



UNIVERSITÀ DEGLI STUDI DI MILANO

Physics Department

PhD School in Physics, Astrophysics and Applied Physics

XXXII Cycle

**Light scattering from micrometric
mineral dust and aggregate particles:
effects of structure and shape
applied to paleoclimate studies**

Scientific Disciplinary Sector FIS/03

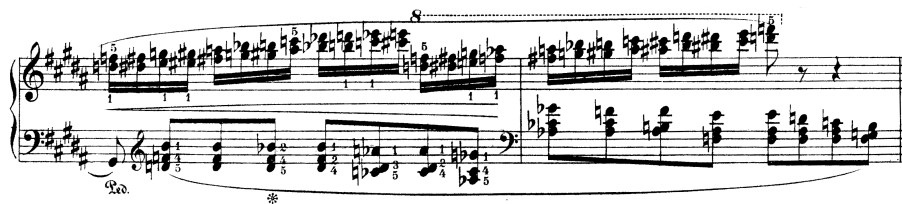
Supervisor: Professor Marco A. C. Potenza

Director of the School: Professor Matteo Paris

Candidate:

Llorenç Cremonesi

A. Y. 2018/2019



*Chopin, Frédéric. Étude Op.25, No.6 (mm 25-26), ca. 1836.
Berlin: Schlesinger, 1883.*

Contents

Introduction	iii
Thesis overview	v
1 Scattering fundamentals	1
1.1 Scattering amplitude	2
1.2 Extinction, scattering and absorption	5
1.3 A collection of independent particles	9
1.4 Polarizability of a particle	11
1.5 Effective Medium Approximations	15
2 Scattering models	19
2.1 Towards composite particles: the structure factor	21
2.2 Rayleigh scattering	24
2.3 Rayleigh–Debye–Gans scattering	27
2.4 Modelling of large compact particles	32
2.5 A molecular optics approach	34
3 Mineral dust	41
3.1 Relevance of mineral dust aerosol	41
3.2 Intricacies of dust optical properties	46
3.3 Effects of shape	49
3.4 Aggregates of mineral dust	62
4 Fractal aggregates	81
4.1 Morphological features of fractal aggregates	82
4.2 Aggregates of polystyrene sulphonate spheres	87
4.3 Experimental results	91
4.4 Near Field Scattering measurements	96

4.5 Simulations	97
Conclusions	107
A Single Particle Extinction and Scattering	115
B Near Field Scattering on flowing samples	121
C Discrete Dipole Approximation	129
Bibliography	133

Introduction

In the present work, we focus on the scattering of visible light from non-spherical particles in the micrometric size range, such as mineral dust and colloidal aggregates. We restrict ourselves to the visible spectrum for practical reasons. From a purely theoretical point of view, such limitation is unnecessary, provided that the particle size and the wavelength are conveniently scaled. However, the relevance of visible and near-infrared light stems from the unique point of view it provides on our natural environment. For example, atmospheric aerosol is unavoidably exposed to both solar and terrestrial radiation. This interaction is known to impact the Earth radiative energy balance (Ferrero et al., 2019, Navarro et al., 2016, Takemura et al., 2002, Albani et al., 2014, Massabò et al., 2013) and the local temperature in the atmosphere, which in turn affects the stability of water droplets and ice crystals, hence the formation of clouds and the occurring of precipitations (Dusek et al., 2006). The extent of this direct and indirect contribution has not to date been determined with adequate accuracy. Similar effects on radiative balance have also been observed in extra-terrestrial environments (Henning and Stognienko, 1996, Levasseur-Regourd et al., 1997, Spiga and Lewis, 2010).

Particles deposited on mid-latitude glaciers, polar snow and sea ice alter the ability of such surfaces to scatter light (albedo) by significantly enhancing absorption (Hansen and Nazarenko, 2004).

The optical properties of a system are not only a useful probe in physics, but also an interesting feature per se, since in many cases they directly determine the extent to which the system is able to interact with its surroundings. For instance, interaction with electromagnetic radiation is the only possible way of studying tropospheric aerosol and cosmic dust in its natural environment, overcoming by remote sensing the distance between the observer and the object (Holben et al., 1998, Li and Draine, 2002, Kokhanovsky, 2016).

Existing research has established that the optical properties of a particle — such

as the scattering and absorption cross sections, albedo and asymmetry parameter — exhibit a strong dependence upon its geometrical structure and composition, as well as its size (Mishchenko et al., 1995, Kahnert et al., 2007, Nousiainen, 2009).

From an experimental point of view, the number of parameters that come into play encourages researchers to deploy a variety of instrumentation to collect data. Optical techniques are a versatile and non-invasive probe, lending themselves to be designed for in situ, routine or in-line applications (Ysard et al., 2018, Kaufmann et al., 2008). They can either be applied to bulk samples, nanocomposites, suspensions of an ensemble of particles or be used in particle-by-particle approaches (Holve and Self, 1979, Potenza et al., 2010a, Potenza and Milani, 2014, Minnai and Milani, 2015, Simonsen et al., 2018). Some examples include Light Detection and Ranging or Laser Imaging Detection and Ranging (LIDAR) (Ferrero et al., 2019), hyperspectral imaging (Garzonio et al., 2018), optical scattering techniques (Mariani et al., 2017), laser sensing particle detectors (Ruth et al., 2008).

At present, the major problem for the interpretation of scattering data lies with the mathematical models linking the optical properties of a particle and its morphology. The very fact that a particle is a system with a limited size is the origin of a completely different level of complexity and interaction capabilities compared to the corresponding bulk case, beyond what is ascribable to the surface to volume ratio. Moreover, a particle (scattering centre) can hardly be considered isolated from its surroundings in most situations.

Lorenz–Mie scattering and effective medium approximations are currently the main theoretical approaches to model the optical properties of aerosol particles, although they can deviate significantly from experimental data (Nousiainen et al., 2011).

Many works have shown a preference for numerical methods over theoretical approximations, also as a tool to interpret experimental data. While retaining some practical advantages, approximate methods fail to reproduce the entire range of observations at all wavelengths as accurately as more computationally intensive exact approaches do (Ysard et al., 2018). Recent advancements in computing capabilities have surely allowed for fast and accurate numerical calculations of complicated particles. It should be noted, however, that such methods tend to be case-specific since they require a detailed modelling of the scatterer.

To understand the radiative properties of complex non-spherical particles it is necessary to go beyond the coarse-grained models on which common approaches are based. Critical aspects of morphology affecting absorption and scattering need to be identified. On the experimental side, a particle-by-particle approach provides a more complete picture. More importantly, experimental data should be burdened by as few free parameters as possible, in order to lay down the guidelines for

more sophisticated mathematical models and feed efficient parameters into climate models (Bond and Bergstrom, 2006).

Thesis aim and overview

The purpose of this thesis is to quantitatively assess the effects of shape and structure of non-absorbing micrometric particles on their radiative properties by optical techniques. Specifically, we extensively rely on the Single Particle Extinction and Scattering (SPES) and Near Field Scattering (NFS) methods to investigate the contribution of scattering to the extinction of visible light, with a particular focus on paleoclimate samples stored in ice cores and on model colloidal aggregates, with a view for applications on airborne particles.

The thesis opens with a part devoted to summarising the foundations of scattering theory, in order to set the ground for the following discussion while defining the notation used throughout the thesis. An overview of the relevant optical properties and theoretical tools is given in chapter 1. We begin by introducing the physical quantities of interest for scattering measurements in a general setting (1.1). The theoretical cornerstone for the experimental techniques used for this work and its main implications are outlined in section 1.2. A very basic description of a collection of scattering centres in an otherwise homogeneous medium is given in section 1.3. We devote section 1.4 to briefly discussing the polarizability of an object finite in size, a key feature in the interaction of particles with electromagnetic radiation. Having covered the case of a homogeneous material, we then move to section 1.5 for discussing the basic effective polarizability of heterogeneous particles.

Chapter 2 follows this introduction and gives an overview of some scattering models of interest and their applicability domain. Section 2.1 is concerned with the link between the structure factor and scattering. Sections 2.2 and 2.3 deal with well-established results and common approaches to simplify the direct and inverse scattering problems depending on the size range of the particles, namely, the Rayleigh and the Rayleigh–Debye–Gans models. This latter case includes a brief analysis for approaching the scattering of non-spherical particles. Building upon this model, the following section (2.4) deals with a recent, simple theoretical approach for large compact particles. To conclude this chapter, a more general model based on molecular optics is summarised in section 2.5.

The second part of this thesis illustrates the experimental procedures followed in this work and the main results. There are two main kinds of samples chosen for analysis. First, the results obtained from compact non-spherical particles as mineral dust from Antarctic and Greenlandic ice cores are reviewed in chapter 3. In a

first section (3.3), we pursue the effect of shape and orientation on the extinction cross section and optical depth of micrometric mineral particles. This constitutes a first step away from the idealised spherical approximation. SPES experimental data provide an estimate of the average aspect ratio of such specimens, while being in open contrast with the predictions of the Mie model. The particle-by-particle approach ensures results which do not suffer from polydispersity.

Attention is then turned in section 3.4 to aggregates of mineral dust formed in deep ice cores, which present further non-idealities owing to their surface roughness. Here the task is to produce a protocol to distinguish such complex particles from compact particles. This is possible thanks to the simultaneous measurement of the extinction cross section and the optical thickness of each particle in the sample. Moreover, populations of isometric aggregates can be identified. This kind of samples also serves as a test of the effective refractive index predicted by the models previously presented in section 1.5. The chapter proceeds to display the results from aggregates of mineral dust and to discuss how to distinguish them from large compact particles without the need for invasive microscopy.

Lastly, the effects of the fractal structure of model non-spherical particles are discussed in chapter 4. Colloidal fractal aggregates are investigated as another example far from being describable in terms of a homogeneous sphere. These systems are very well characterised in literature, and widely accepted models for their structure have been provided, as discussed in the introductory section 4.2. This makes them a perfect benchmark for testing the optical models outlined in the first part of this thesis. Quantitative evidence of the effects given by correlations of the fields radiated by each monomer is provided in sections 4.3 and 4.4. Taking advantage of the polydispersity of the samples, an experimental measurement of both the fractal dimension and the scaling prefactor characterising such fractal structures is produced. Their optical properties are related to the internal structure by a theoretical model designed for the purpose. A connection with the optical theorem is also given. In terms of the models of chapter 2, a comparison between the mean field approximation and the Rayleigh–Debye–Gans approximation favours the latter in predicting the forward scattered field. The results of numerical calculations support this conclusion, as discussed in a dedicated section (4.5).

The appendices are an essential part of this thesis and are conceived as a quick reference to the tools we used for this work. On the experimental side, we vastly relied on the SPES method. Its working principle is outlined in appendix A, providing references for further details on the instrument. The simultaneous and independent measurement of both the real and imaginary part of the scattering amplitude proved to be the fundamental requirement for findings that would be hidden to traditional intensity measurements. In appendix B, we give a brief review of a

method based on Near Field Scattering, modified to be applied to flowing samples. Finally, numerical calculations based on the Amsterdam Discrete Dipole Approximation (ADDA) have been an integral part of the thesis as a support to experimental findings of chapters 3 and 4. The main features of this code are sketched in appendix C.

Scattering fundamentals

Scattering of electromagnetic radiation occurs whenever it encounters a heterogeneity of the medium in which it is propagating, whether due to variations in density or composition (Bohren and Huffman, 2008). Such heterogeneity may be at the atomic, molecular, or greater scale, such as groups of molecules or agglomerate systems. Electromagnetic radiation propagating in a medium without any inhomogeneity is not treated within the scattering theory. Nonetheless, typical optical phenomena such as diffraction, reflection and refraction can be ultimately ascribed to scattering (Fearn et al., 1996, Lalor and Wolf, 1972). Strictly speaking, a perfectly uniform medium does not exist as a consequence of the mere corpuscular nature of matter. It can, however, be considered as such depending on the wavelength of the radiation, which determines the relevant length scale of the phenomenon (Born and Wolf, 2013).

Given the scope of this work, we can describe scattering from a classical perspective; the basic mechanism is as follows. The electromagnetic wave excites electrons in the molecules it encounters, causing them to oscillate along with it with a definite phase. Accelerated electric charges then radiate electromagnetic waves in all directions by acting like small dipole antennas. The most prominent aspect of scattering is that energy is radiated in a variety of directions other than the direction of incidence¹. When electromagnetic waves are scattered at the same frequency as that of the incident wave, scattering is said to be elastic. Other phenomena such as Raman scattering, phosphorescence, fluorescence, or even thermal radiation do not enjoy this property, as to some degree they are related to absorption. As Miles et al. (2001) point out, scattering does allow for in-depth insight. The anisotropy of molecules, collective scattering from many molecules and inelastic scattering associated with rotational and vibrational transitions all contribute to depolarise the scattered field and influence the spectral response of the sample. In the samples we are interested in, however, inelastic Raman scattering is generally much weaker than elastic scattering (Redmond et al., 2010).

¹This can be counted among the striking features of the atmosphere of our planet. See for example Potenza (2015).

We will consider the elastic scattering caused by a micrometric and sub-micrometric particle acting as a non-spherical polarizable obstacle as opposed to apertures, extended interfaces or scattering by turbulence. This includes particles which have a complex internal structure, assemblies of composite materials and small scatterers embedded in a matrix, provided that such systems are finite in size. Some particles found in the samples analysed in this work are shown in figure 1.1 as an example.

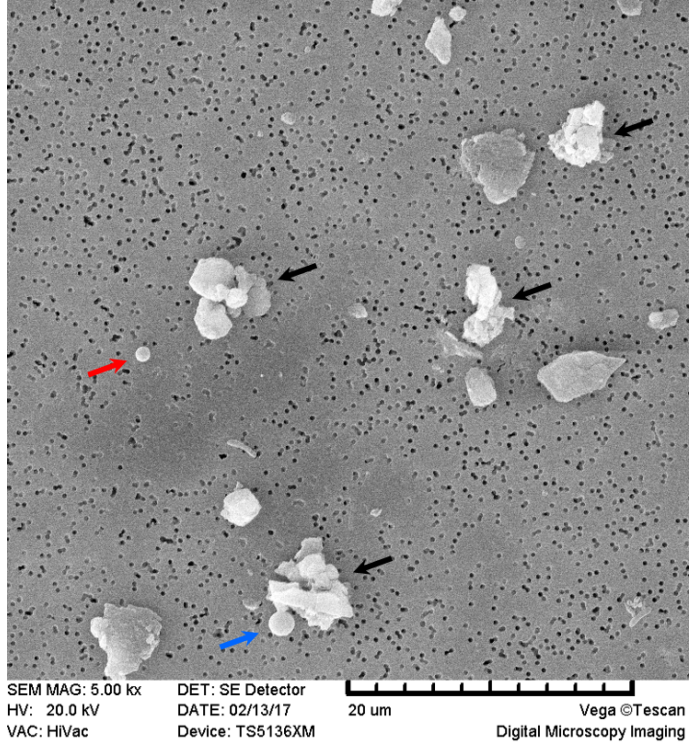


Figure 1.1: Scanning Electron Microscope image of mineral dust particles in a deep ice core from Dome C, Antarctica (sample 5316, ~ 2900 m). Aggregates of small grains are marked with a small black arrow. This shot also includes polystyrene spheres $1\text{ }\mu\text{m}$ and $2\text{ }\mu\text{m}$ in diameter, marked with a red and a blue arrow respectively.

What follows is a brief review of an essential set of theoretical tools, aiming at discussing some important properties and results.

1.1 Scattering amplitude

Let us consider a particle illuminated by a monochromatic light source at a large distance from the particle, propagating along the z axis (figure 1.2). The distance

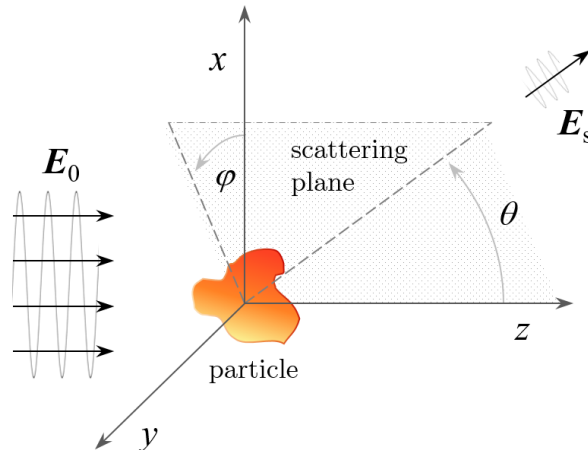


Figure 1.2: Schematic of the scattering geometry of an arbitrary particle in an incident radiation field. The arrows represent the direction of propagation of the fields which is parallel to the wave vector and to which the fields are orthogonal. This defines the positive direction of the z -axis, while the incident and scattering direction together define the scattering plane. $\theta = 0$ corresponds to forward scattering, while $\theta = \pi$ to backward scattering.

might be large enough to disregard the details about the light source, and treat the incoming field locally as a plane, scalar wave propagating in a homogeneous non absorbing medium like air. The particle in the origin of the reference frame is exposed to an incoming field $\mathbf{E}_0 \sim e^{ikz - i\omega t}$, where $k = \frac{2\pi}{\lambda}$ and λ is wavelength relative to the surrounding medium, and scatters light at all angles. Restricting our description to linear optics, we assume the scattered field to be related to the incoming field by a linear function.

At a distance r from the origin, in the far-field, the scattered wave \mathbf{E}_s is spherical wave modulated and dephased as follows²:

$$\mathbf{E}_s(r, \theta, \varphi) = S(\theta, \varphi) \frac{e^{ikz - ikr}}{ikr} \mathbf{E}_0 \quad (1.1)$$

where i is the imaginary unit, θ is the *scattering angle* with respect to the direction of propagation of the incoming light, while ϕ is the *azimuth* angle as defined in figure 1.2. This equation defines the *scattering amplitude*, $S(\theta, \varphi)$, a complex dimensionless quantity which links the incoming field to the scattered field, and

²for simplicity, we drop the time dependence.

completely determines the scattering by an arbitrary particle of finite size³. It is a complex quantity since, in general, the scattered field is not in phase with the incident field. $S(\theta, \varphi)$ is normalised on its integral, as it will be discussed in section 1.2 (see equation (1.6)). Notably, $S(\theta, \phi)$ does not depend upon the distance r at which the particle is observed, but it does depend on its orientation with respect to the incident (plane) wave and the state of polarization of the latter.

In equation (1.1) we considered the simplified case in which $S(\theta, \varphi)$ is a scalar quantity and \mathbf{E}_0 is not polarized. The polarization of the incoming light breaks the symmetry of this equation (Bohren and Huffman, 2008). For example, let us suppose that the incident field is polarized linearly along the x -axis (figure 1.2). Since electromagnetic radiation is a transverse wave, $E_{s\parallel}$ and $E_{s\perp}$ must behave differently: the intensity on the scattering plane parallel to the direction of polarization drops at about $\theta = 90^\circ$, because this direction is parallel to the oscillations of the charges in the particle. This should be considered in any application involving a sensor collecting light at a large scattering angle, θ , or over a large solid angle.

Another factor that can break the symmetry in equation (1.1) is the particle shape, even when illuminated by unpolarized light. This effect is strong in the Rayleigh regime (see section 2.2) for light scattered at $\theta = 90^\circ$ (Jackson, 1999). With increasing particle size the degree of polarization diminishes rapidly, but particle non-sphericity contributes increasingly to the anisotropy of $S(\theta, \varphi)$ with respect to φ (Horvath, 2009).

In this work, we used linearly polarised light and investigated non-spherical particles. We should therefore consider a more general form of $S(\theta, \varphi)$: a matrix with four complex entries, which include depolarization effects. Equation (1.1) is therefore (Van de Hulst, 1981):

$$\begin{pmatrix} E_{s\parallel} \\ E_{s\perp} \end{pmatrix} = \frac{e^{ikz - ikr}}{ikr} \begin{pmatrix} S_2 & S_3 \\ S_4 & S_1 \end{pmatrix} \begin{pmatrix} E_{0\parallel} \\ E_{0\perp} \end{pmatrix} \quad (1.2)$$

S_1 gives the amplitude of the perpendicular component of the incident field in $E_{s\perp}$. Similarly, S_2 gives the amplitude of the parallel component of the incident field in $E_{s\parallel}$. S_3 and S_4 give the corresponding depolarised terms instead, and vanish for homogeneous spheres.

One aspect which is worth highlighting here is that within the extension of the incident beam, \mathbf{E}_0 and \mathbf{E}_s superimpose and interfere. Whether the interference is constructive or destructive depends on the phase of $S(\theta, \varphi)$. This is particularly relevant at $\theta = 0$, where the incident field cannot be avoided, since it is related to

³The minus sign in front of ikr is introduced following Van de Hulst (1981) and has become a convention. An alternative definition in terms of *propagating waves* is given in Bohren and Huffman (2008).

the total scattering cross section, as will be detailed later on (section 1.2).

In many laboratory settings the source consists of a laser Gaussian beam, so that in the far-field there is only the scattered radiation at $\theta > 0$. A detector placed anywhere at a large distance from the particle will sense an intensity given by

$$I_s(r, \theta, \varphi) = \frac{|S(\theta, \varphi)|^2}{k^2 r^2} I_0 \quad (1.3)$$

The quantity $|S(\theta, \varphi)|^2$ is of interest in that it reflects the internal structure of the particle (Debye and Bueche, 1949, Debye et al., 1957), as will be discussed in section 2.1. Usually, one drops the dependence on φ by taking a rotational average, whereas its trend as a function of the scattering angle θ gives the structure factor (section 2.1). This is an essential feature for both laboratory settings and in situ measurements (Mishchenko et al., 1995).

1.2 Extinction, scattering and absorption

The Optical Theorem is a deceptively simple relation which directly follows from the conservation of energy. Its generality and far-reaching implications make it a milestone of scattering theory (Newton, 1976, Bohren and Huffman, 2008, Van de Hulst, 1981). It connects the total extinction cross section of a scatterer to the real part of the scattering amplitude⁴. Before introducing the theorem, we need to define some relevant physical quantities to get started.

1.2.1 Optical cross sections

When a particle intercepts an electromagnetic wave, the power it removes from the incident beam equals the product between the irradiance (energy per unit area per unit time) of the incident beam and *some area*. This area defines the *extinction cross section*, C_{ext} . The *absorption cross section*, C_{abs} , can be similarly defined as the area one must consider in evaluating the flux of the incident beam so that this equals the power absorbed by the particle:

$$P_{\text{ext}} = I_0 \cdot C_{\text{ext}} \quad ; \quad P_{\text{abs}} = I_0 \cdot C_{\text{abs}} \quad (1.4)$$

To our purposes, it is important that these two quantities are not defined from a geometrical point of view, but rather with the energy balance in mind. The total energy per unit time scattered in all directions equals the power per unit area of the

⁴Depending on the chosen notation, this is replaced by the imaginary part of the scattering amplitude by some authors. Here we follow Van de Hulst (1981) as opposed to the textbook from Jackson (1999)

incident wave traversing some area C_{sca} , which is named *scattering cross section* and is defined as

$$C_{\text{sca}} = \frac{1}{k^2} \int_{4\pi} |S(\theta, \varphi)|^2 d\Omega \quad (1.5)$$

where $d\Omega = d\varphi d(\cos\theta)$ is the element of solid angle and $S(\theta, \varphi)$ is the quantity defined in section 1.1. Furthermore, equation (1.4) gives the normalisation of $S(\theta, \varphi)$. As we will see in the experimental part, the complex amplitude assumes values larger than one, especially at low angles, but this does not imply that the particle emits more energy than it receives.

Scattering has some further interesting features. The differential scattering cross section $\frac{dC_{\text{sca}}}{d\Omega}$ is defined as the cross section per unit solid angle, so that

$$C_{\text{sca}} = \int_{4\pi} \frac{dC_{\text{sca}}}{d\Omega} d\Omega \quad (1.6)$$

Comparing (1.6) with the definition in (1.4) it follows that

$$\frac{dC_{\text{sca}}}{d\Omega} = \frac{1}{k^2} |S(\theta, \varphi)|^2 \quad (1.7)$$

This physical quantity is experimentally accessible in angle light scattering measurements (see section 4.4) and establishes a direct link with theory. It bears essential information about the internal structure of the scatterer.

The angular dependence of the scattering cross section is precisely what distinguishes a sphere from an amorphous particle having the same geometrical cross section or the same volume. The angular distribution of light intensity scattered by a particle normalised by its integral

$$\frac{\frac{dC_{\text{sca}}}{d\Omega}}{C_{\text{sca}}} = \frac{|S(\theta, \varphi)|^2}{k^2 C_{\text{sca}}} = \frac{|S(\theta, \varphi)|^2}{\int_{4\pi} |S(\theta, \varphi)|^2 d\Omega} \quad (1.8)$$

is commonly known as the *phase function* (Mishchenko et al., 1995, Bond et al., 2013). This name historically refers to lunar phases, and might give rise to ambiguity when discussing waves (Van de Hulst, 1981), we will therefore avoid this definition. In the experimental section we will use the differential scattering cross section normalised to its maximum, which essentially gives the structure factor of the particle (see section 2.1).

We may also use $\frac{dC_{\text{sca}}}{d\Omega}$ to estimate the balance between the forward and the backward scattering. The quantity

$$\gamma = \frac{1}{C_{\text{sca}}} \int_{4\pi} \frac{dC_{\text{sca}}}{d\Omega} \cos\theta d\Omega \quad (1.9)$$

is called the *asymmetry parameter*. The cosine in the integral produces a weighted average of forward and backward scattering. Isometric scattering would ideally give $\gamma = 0$, a value to which small particles come close. Non absorbing particles of increasing size tend to predominantly scatter light in the forward direction, so that $\gamma \rightarrow 1$. A reflecting (metallic) particle would give negative values of γ instead, up to the limiting case of a perfect mirror where $\gamma = -1$.

Now, since energy must be conserved, C_{ext} gives the total radiant flux both scattered and absorbed by the particle:

$$C_{\text{ext}} = C_{\text{sca}} + C_{\text{abs}} \quad (1.10)$$

which might be phrased as *extinction = scattering + absorption*. Those areas are expressed in μm^2 in the present work to match the order of magnitude typical of our samples. We note that for non-absorbing particles extinction and scattering must be equivalent. In particular, extinction is then equal to the integral of the energy radiated at all angles by the particle. This suggests to put non-absorbing aerosol on the negative side of the Earth energy balance (Stocker, 2014).

We finally introduce optical efficiency. The ratio of the optical cross sections to the geometric cross section of the sphere of equivalent volume, $G = \pi r_{\text{eq}}^2$ define the corresponding efficiency factor

$$Q_{\text{ext}} = \frac{C_{\text{ext}}}{G} \quad (1.11)$$

and alike definitions for scattering and absorption efficiency factors as in Redmond et al. (2010). The ratio between scattering efficiency to extinction efficiency is defined as *single scattering albedo*. Its value approaches 1 for non absorbing particles, and 0 if scattering is negligible compared to absorption. Whether the quantity in equation (1.11) is greater or lower than unity depends on the polarizability of the particle. Interestingly, for very large particles it approaches the value 2 in the far-field (see fig 1.3). The removal from an incident field of twice the amount of light a particle can intercept is known as the extinction paradox (Van de Hulst, 1981). The extinction cross section of a particle should not, in fact, be confused with its geometrical cross section. The very fact that the particle is detectable at angles $\theta > 0$ implies some energy which would have travelled undisturbed is deviated elsewhere, which has a relevant contribution to the energy balance at the length scales and solid angles under consideration⁵.

⁵See for example Chylek (1977), Moosmüller and Sorensen (2018) for further details.

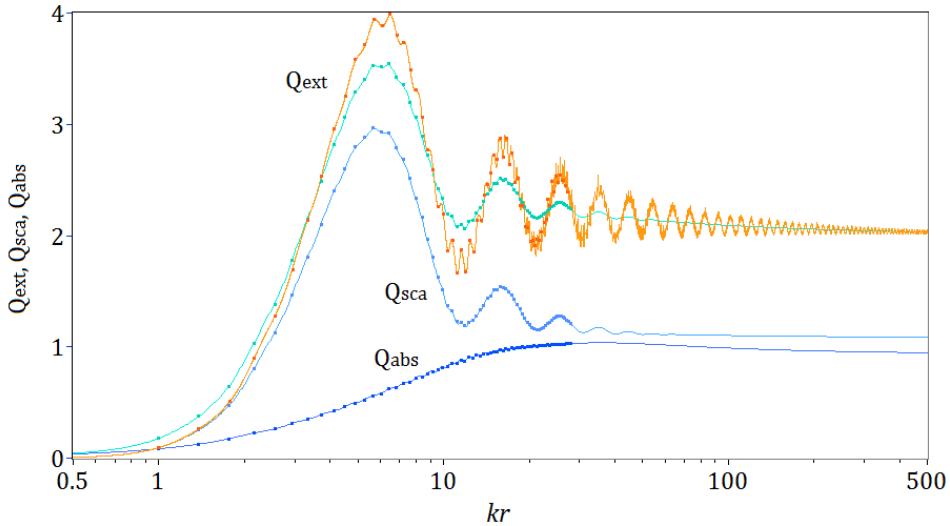


Figure 1.3: Mie calculations of the extinction efficiency of spherical water droplets as a function of the dimensionless size parameter kr . The orange curve refers to $m = 1.33$, whereas the blue curves refer to slightly absorbing spheres with $m = 1.33 + i0.03$. The two lower curves refer to the scattering and absorption cross sections which add to Q_{ext} . Dots show the corresponding discrete dipole approximation calculations (DDA, see appendix C), up to $kr \sim 30$ due to practical constraints. The limit for Rayleigh scattering can be set to $kr \sim 1$. Mie calculations were conducted using MiePlot v4.6 (Philip Laven, www.philiplaven.com/mieplot.htm).

1.2.2 Optical theorem

Given the above definitions, the optical theorem states that

$$C_{\text{ext}} = \frac{4\pi}{k^2} \Re S(0) \quad (1.12)$$

hence the power removed from the incident beam, which includes the integral of the power radiated at all angles is related to the phase of the forward scattered field. We remark that by equation (1.10), $S(0)$ is then related to absorption as well.

However small $\Re S(0)$ might be compared to $\Im S(0)$, it cannot be zero⁶. Otherwise stated, the forward scattered field is not in phase with the incident field and must destructively interfere with it to some degree. Interestingly, this destructive interference at $\theta = 0$ of the scattered wave with the transmitted wave is the process

⁶As we will see in the following, usually $\Im S(0) \gg \Re S(0)$ in sparse, non-absorbing particles.

through which extinction occurs, rather than some sort of shadowing phenomenon. This result can be considered a cornerstone for the present work, and is the fundamental relation underlying the experimental method we adopted (see appendix A).

Equation (1.12) has also a noteworthy practical outcome for our purposes: it is not necessary to estimate absorption and to integrate the scattered intensity measured over a wide solid angle to determine the extinction, provided that the real part of the forward scattering amplitude can be retrieved. This requires to measure the field — not simply the intensity — in the forward direction, and can be attained with a *heterodyne* optical layout (Ferri et al., 2004, Mazzoni et al., 2013, Potenza et al., 2015c): the intense transmitted beam used to illuminate the sample and the faint field scattered forward by single particles in the sample are superimposed and interfere with each other. Such self-reference interferometric scheme opens up the possibility of separating the two fields, and to independently and simultaneously measure the real and imaginary part of the scattered field.

We close this section with some remarks concerning the validity limits of equation (1.12). The basic formulation of the optical theorem reported here follows from considering planar, scalar waves, and is fully valid to our purposes. Some authors have proposed a generalised formulation which applies to situations where the vectorial nature of the electromagnetic field cannot be overlooked. For example, violations of the optical theorem in the form seen in equation (1.12) have been observed experimentally for plasmonic particles illuminated by radially or azimuthally polarized beams. In such settings, the samples exhibit strong extinction but vanishing scattering in the forward direction. Other examples include tightly focused beams, surface waves and complex vortex beams carrying optical angular momentum (Krasavin et al., 2018, Newton, 1976, Halliday and Curtis, 2009). A discussion of such peculiar cases is, however, beyond the scope of this chapter.

1.3 A collection of independent particles

Particularly worthy of mention at this point is the application of the optical theorem to a collection of small particles far apart from each other, as might be the case of a rarefied cloud of tiny scatterers suspended in the atmosphere. Specifically, we assume that the inter-particle distances are much larger than both the wavelength and the sizes of the particles, so that they can be considered as independent scatterers. This ensures that the field incident on each particle is essentially given by the incoming wave, and multiple scattering is negligible. However, the differential scattering cross section still depends on the positions of the scatterers. Denoting

with \mathbf{k} the wave vector of the incident field, and \mathbf{k}_s the wave vector of the scattered field, the quantity

$$\mathbf{q} = \mathbf{k}_s - \mathbf{k} \quad (1.13)$$

is the scattering wave vector. Elastic scattering requires that $|\mathbf{k}_s| = |\mathbf{k}| = k$. As a result

$$|\mathbf{q}| = q = 2k \sin \frac{\theta}{2} \quad (1.14)$$

In the far-field, the phase lag between the fields scattered at a given angle by any two particles is (Born and Wolf, 2013)

$$\Delta\phi = \mathbf{q} \cdot \mathbf{r}_{1,2} \quad (1.15)$$

where $\mathbf{r}_{1,2}$ is the vector joining the two particles, thereby the phase lag $\Delta\phi$ vanishes if \mathbf{k} is parallel to \mathbf{k}_s . If the particles are randomly distributed, at any angle $\theta > 0$

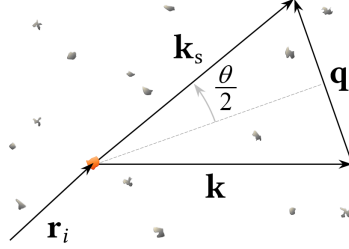


Figure 1.4: Definition of the scattering vector \mathbf{q} for elastic scattering.

the overall intensity is approximately given by the sum of the intensities scattered by each particle in the cloud. This follows from the averaging out of constructive and destructive interference. If we observe the field scattered at $\theta = 0$, particles act like coherent emitters and interfere constructively regardless of their position in the scattering volume (Parola et al., 2014). Under this assumptions, the total scattering amplitude of an ensemble of N particles is

$$S^{tot}(0) = \sum_{j=1}^N S_j(0) \quad (1.16)$$

where the index j is the particle label. Note that the position of the particles is irrelevant in this picture. The total scattering cross section is thus given by

$$C_{\text{ext}}^{tot} = \sum_{j=1}^N C_{\text{ext},j} \quad (1.17)$$

It can be shown that, when considering an extended collection of independent particles, a similar relation also applies to the total scattering cross section (Van de

Hulst, 1981)

$$C_{\text{sca}}^{\text{tot}} = \sum_{j=1}^N C_{\text{sca},j} \quad , \quad C_{\text{abs}}^{\text{tot}} = \sum_{j=1}^N C_{\text{abs},j} \quad (1.18)$$

where the equation involving the absorption cross section is a consequence of equation (1.10). These two equations only apply to low density clouds of particles, where there is no multiple scattering and particles are sufficiently far apart from each other so that the internal fields in each particle are uncorrelated. The reader might refer to the first part of the work by Parola et al. (2014) for further details about the effective refractive index and the scattering amplitude of such a system. The model described above is relevant for estimating the overall aerosol optical depth (AOD) of the atmosphere, which may be considered to good approximation as a very rarefied cloud of solid particles immersed in a non-absorbing medium. This linear approximation is used in satellite and ground based remote sensing of aerosols, water vapour and clouds.

It requires, however, to know the optical properties of the particles in the cloud ($S_j(0)$, $C_{\text{sca},j}$, and so forth), or at least a properly defined average, usually based on their size distribution (Müller et al., 2010). We will now proceed to focus on this aspect of the problem.

Looking more closely to the properties of the individual particles, one may wonder whether the independent scattering condition also applies to the primary particles in aggregates. This would lead to only consider the total mass of particles suspended in the atmosphere, overlooking their size distribution. In chapter 4, we will see that even sparse particles do not meet the requirements for this approximation, such as fractal aggregates or soot⁷. For example, at close distances, neighbouring particles experience the coupling of internal electric fields (Kinnan and Chumanov, 2010) to an appreciable extent, so that equation (1.17) does not give the best interpretation of experimental data.

1.4 Polarizability of a particle

Here we discuss the constituent material of the particle, which ultimately governs the extent of its interaction with electromagnetic waves. In the scope of the present work, it is sufficient to investigate the molecular polarizability α of a particle following the classic conceptual framework in Jackson (1999), Ashcroft and Mermin (2010), rather than its detailed chemical properties and its interaction with single

⁷In the literature, the term 'soot' is used to refer to the by-product of incomplete combustion of carbonaceous materials, commonly consisting in aggregates of nanometre-size spheres of carbon. It is mainly composed of particulate carbon and may encompass traces of fuel and other impurities, depending on the source.

photons.

The polarizability α , an extensive physical quantity related to volume and shape, is defined as follows. A homogeneous, external field \mathbf{E}_0 applied to a neutral, non-polar object induces a rearrangement of its atomic charges, which in turn gives rise to a local field \mathbf{E}_{loc} and a dipole moment

$$\mathbf{p} = \alpha \mathbf{E}_{\text{loc}} \quad (1.19)$$

In general, α is a tensor, here we restrict ourselves to the much simpler case of a scalar polarizability (i.e. we assume a diagonal tensor). This quantity is related to the dielectric function $\varepsilon(\omega)$ which is frequency dependent⁸ and it is complex if the frequency of the incident radiation is close to any resonant frequency of the molecules in the sample. This results in absorption of the incident light and an increase in the temperature of the particle (this energy is then returned to the environment as thermal radiation).

It is common to write α in terms of the refractive index of the particle $n = \sqrt{\varepsilon}$ relative to the refractive index n_0 of the surrounding medium, $m = n/n_0$. We should emphasise that it is α , rather than solely the refractive index, the parameter that provides the link between the field scattered at all angles by an arbitrary particle and the incident field.

To retrieve α , the microscopic Maxwell—Lorentz equations must be solved. If there are many molecules in a volume of order λ^3 , the material can be considered a homogeneous medium consisting of densely packed dipoles. Let \mathcal{N} be the number of molecules per unit volume, then the dielectric dipole polarizability is given in terms of the refractive index by the Lorentz-Lorenz formula:

$$\alpha = \frac{3}{4\pi\mathcal{N}} \frac{m^2 - 1}{m^2 + 2} \quad (1.20)$$

which in Gaussian units has the dimensions of a volume. Equation (1.20) is usually referred to as the Clausius–Mossotti equation when the squared refractive index is replaced by the corresponding dielectric function $\varepsilon = m^2$ relative to the medium. We refer to Le Ru et al. (2013) for a refinement of this model.

The constants in the prefactor come from considering a spherical volume surrounding the site at which the local electric field is computed, known as the Lorentz sphere. Given that there is no restriction on the spatial extension of the material, this formula may be applied to bulk materials and gases as well (Ashcroft and Mermin, 2010). It is understood, however, that single molecules (dipoles) are much smaller than the wavelength. The key point is that the contribution from all

⁸For instance, see Kou et al. (1993) for a comprehensive study on the refractive index of water.

the surrounding molecules to the local field applied to each molecule is taken into consideration, which makes for a significant complexity. A common assumption in deriving the polarizability is that the material has a certain degree of symmetry in the arrangement of its constituent molecules, so that when calculating the local field at a given point some terms cancel out (Ashcroft and Mermin, 2010). Usually, the molecules are considered to be located on a cubic lattice, which is a seemingly strict constraint. However, due to the high number of scattering centres and to their proximity, it is generally safe to assume an isotropic distribution, which has an equivalent effect. Such statistical average encompasses contributions from a large number of molecules at all sides to the local field at a given point. Interestingly, this means that in measuring the refractive index of a material we are to some extent macroscopically sensitive to the microscopic arrangement of matter.

Let us now move to the link between α and the morphology of the particle. In the Rayleigh regime, the polarizability might be written as (Van de Hulst, 1981)

$$\alpha = \frac{3v}{4\pi} \frac{m^2 - 1}{m^2 + 2} \quad (1.21)$$

where v is the volume of the particle. As a straightforward reference, we can consider a homogeneous sphere of radius a :

$$\alpha = a^3 \frac{m^2 - 1}{m^2 + 2} \quad (1.22)$$

For example, this will be useful in the following when considering the small spherical constituent blocks of colloidal aggregates.

Equation (1.21) cannot be generalised to a particle of arbitrary size, as we will see in greater detail in the following chapters. To be specific, let us consider a non-spherical micrometric grain of a given mineral as the ones investigated in section 3.3. We assume to know precisely its composition, hence its refractive index, and that we can measure its volume with a Coulter Counter (Delmonte et al., 2010). We would then have all the parameters appearing in equation (1.21). Polarizability is nonetheless a microscopic quantity related to the local field \mathbf{E}_{loc} , which is determined by the Laplace equation for the corresponding electric potential. Particle shape and orientation with respect to the incident field affect the boundary conditions of the Maxwell equations, thus they affect α . For example, in figure 1.5 are shown the diametrical sections of the internal fields in a prolate ellipsoid with its major axis parallel (left) and perpendicular (right) to the incoming linearly polarized field, with very evident differences. The angular dependence of the scattering amplitude in panels (e) and (f) is dramatically affected by a change in orientation

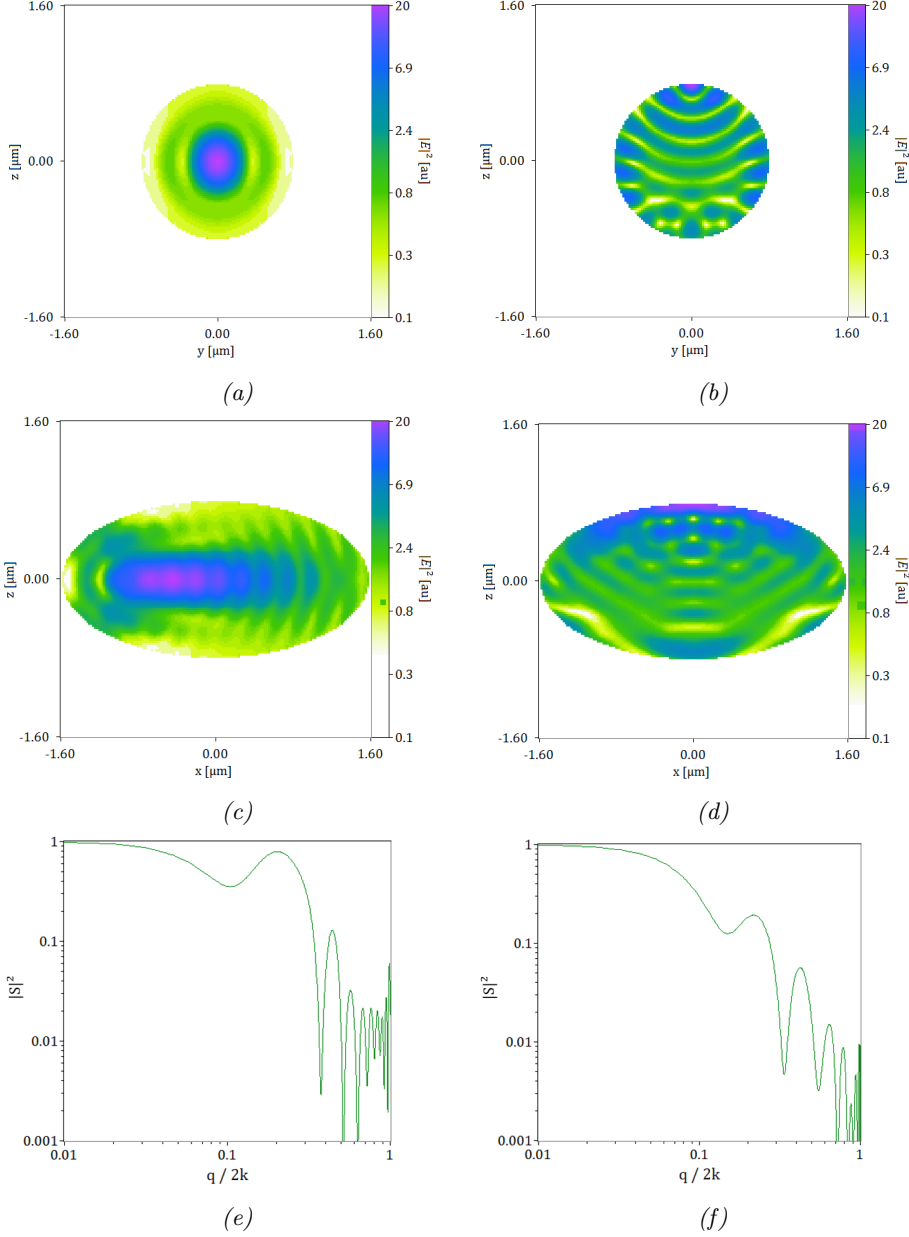


Figure 1.5: DDA calculation of the internal fields in a prolate ellipsoid (volume-equivalent radius $r_{\text{eq}} = 1 \mu\text{m}$, aspect ratio 0.5, $m = 1.5$). The major axis is oriented parallel (left) and orthogonal (right) to the linearly polarized incoming field ($\lambda = 0.632 \mu\text{m}$). (a,b) section at $x = 0$, (c,d) section at $y = 0$, (e,f) square modulus of the scattering amplitude normalised on its maximum.

(notably, the electric field inside the particle is not uniform).

In summary, equation (1.21) is only applicable to isometric particles or in the ideal case of Rayleigh scattering. In other cases one can expect the shape to be somewhat encoded in the scattered field.

Spheres and spheroids have been playing a prominent role in scattering theory since its early steps (Mie, 1908). They are a benchmark and a widespread tool for approximating non-spherical particles like the ones considered in Torres et al. (2017), Simonsen et al. (2018), Ch  lek and Klett (1991), Potenza et al. (2016a). However, it should be pointed out that such particles usually are considerably different in their optical properties from spherical particles of comparable size and chemical composition (Mishchenko et al., 2016, Sorensen et al., 2018, Leinonen et al., 2012). This will be the subject of chapter 2. For example, a homogeneous sphere cannot predict the correct depolarization effects (Mishchenko et al., 2000, Potenza et al., 2010b).

1.5 Effective Medium Approximations

In closing this chapter, we take a small step away from the homogeneous sphere model by outlining a widely adopted approach to generalise the equations of section 1.4 to particles which are not uniform in composition. Let us consider a non absorbing homogeneous medium in which many small particles of a different material are spread. The medium is commonly referred to as the *matrix* while the particles dispersed in it are called *inclusions*⁹. The overall response of such heterogeneous material to external fields might be modelled by replacing it with a homogenised medium by Effective Medium Approximations (EMA).

Originally developed for bulk, they have been extended to finite size systems such as noble metal nanoparticles. Similarly, EMA have been successfully applied to clusters and structured crystals, interstellar dust, metal–dielectric composites, soot, porous rocks and percolative systems (Stroud, 1975, Jones, 1988, Luck, 1991, Mann et al., 2009, Kinnan and Chumanov, 2010, Minnai et al., 2017). Such approximations only account for simple structural properties of the medium like the *volume fraction*, defined as the ratio of the total volume occupied by the inclusions to the total volume of the composite medium. They rely on the following assumptions:

- i) The material must respond linearly to the external field (Stroud, 1998).
- ii) The polarizable inclusions are treated as individual dipoles whose shape does not affect appreciably their interaction with electromagnetic radiation and

⁹Historically, these terms come from gold nanoparticles suspended in water (see Minnai (2018)).

fall in within the Rayleigh scattering regime.

- iii) More importantly, inclusions are considered to be independent, non-interacting entities and multiple scattering is neglected.

Some generalisations have been proposed in order to extend EMA to the specific case of large inclusions (Ch ylek and Srivastava, 1983) and to take into account the shape of the small particles inside the matrix (Ch ylek and Videen, 1998). The optical and electrical properties of the composite medium are estimated on the basis of an average of the polarizabilities of its individual components, weighted by their concentrations. It is customary to express this approximation in terms of the dielectric permeabilities of the system. Specifically, in the Maxwell-Garnett model (Maxwell-Garnett, 1904), the effective dielectric permeability ε_m is given by

$$\frac{\varepsilon_{\text{eff}} - \varepsilon_m}{\varepsilon_{\text{eff}} + 2\varepsilon_m} = \phi \frac{\varepsilon_i - \varepsilon_m}{\varepsilon_i + 2\varepsilon_m} \quad (1.23)$$

where ϕ is the volume fraction, while ε_m and ε_i are the dielectric constants of the matrix and the inclusions, respectively. Although arising from different perspectives, equation (1.23) and the Lorentz-Lorenz formula in (1.20) are closely related (Markel, 2016). The dependence on the refractive index is the same, while the volume fraction has a role akin to that of the number density of molecules.

An explicit solution of equation (1.23) for the effective dielectric constant is

$$\varepsilon_{\text{av}}/\varepsilon_m = 1 + \frac{3\phi \frac{\varepsilon_i - \varepsilon_m}{\varepsilon_i + 2\varepsilon_m}}{1 - \phi \frac{\varepsilon_i - \varepsilon_m}{\varepsilon_i + 2\varepsilon_m}} \quad (1.24)$$

from which an effective refractive index can be defined, by taking $m_{\text{eff}} = \sqrt{\varepsilon_{\text{av}}/\varepsilon_m}$. The agreement to experiment is reasonably good if the materials in the mixture are optically similar (Ch ylek and Videen, 1998), i.e. the refractive index jump is small. We highlight that this model does not explicitly depend on the size of the inclusions, and the volume fraction ϕ is arbitrary, in principle (Stroud, 1998). The applicability of this approximation is, however, restricted to grain sizes much smaller than the wavelength of the incident radiation. We will test this model in chapter 4.

The Maxwell-Garnett formula has been generalised to multi-component mixtures (Markel, 2016). Equation (1.23) can be written in the form

$$\frac{\varepsilon_{\text{eff}} - \varepsilon_m}{\varepsilon_{\text{eff}} + 2\varepsilon_m} = \sum_j \phi_j \frac{\varepsilon_j - \varepsilon_m}{\varepsilon_j + 2\varepsilon_m} \quad (1.25)$$

where ε_j and ϕ_j are the permittivity and the volume fraction of the j -th material, respectively.

A significant example to our purposes is the following. If we consider a spherical homogeneous particle of radius R with N smaller spherical inclusions of radius a , then the volume fraction is simply $\phi = Na^3/R^3$. Applying the mean field approximation, the polarizability of such composite particle is given by

$$\alpha^{\text{eff}} = R^3 \frac{\varepsilon_{\text{eff}} - \varepsilon_{\text{m}}}{\varepsilon_{\text{eff}} + 2\varepsilon_{\text{m}}} = Na^3 \frac{\varepsilon_{\text{i}} - \varepsilon_{\text{m}}}{\varepsilon_{\text{i}} + 2\varepsilon_{\text{m}}} = N\alpha \quad (1.26)$$

Thus the polarizability of the whole composite particle is proportional to the polarizability of a single inclusion, α , and scales linearly with its mass. The same applies to an aggregate of N particles, which is modelled as a single entity of polarizability $N\alpha$. In the context of this approximation, polarizability is in fact treated as an ideal extensive property of the system. Similarly, equation (1.25) yields a weighted sum of the polarizabilities, namely

$$\alpha^{\text{eff}} = \sum_j N_j \alpha_j \quad (1.27)$$

However, one must be aware that the matrix and the inclusions are not interchangeable, since the Maxwell-Garnett formula is not symmetric. Particles must be, at least in principle, distinguishable from the matrix in which they are embedded. This in turn acts as an implicit constraint on ϕ .

Multi-component random mixtures are usually described by a model symmetric with respect to all components, known as the Bruggeman formula

$$\sum_n \phi_n \frac{\varepsilon_n - \varepsilon_{\text{eff}}}{\varepsilon_n + 2\varepsilon_{\text{eff}}} = 0 \quad (1.28)$$

The volume fractions ϕ_j are arbitrary, provided their sum equals 1 (Stroud, 1998). The effective medium approaches outlined above implicitly assume in their derivation that particles in the medium are randomly distributed, i.e. they are not correlated (Sihvola, 2001). The internal structure of the scatterer is completely disregarded. Thus, two composite media characterised by a different distributions of scatterers, but with the same density, are indistinguishable. For instance, if we were to split in half every inclusion and rearrange the mixture while keeping ϕ constant, the effective permeability predicted by this model would be the same. This is a feature worth keeping in mind in view of what will be discussed in sections 2.3 and 2.5.

Despite the widespread use of effective medium approximations, there have been concerns about their effectiveness and accuracy in some contexts. As stated by Mishchenko et al. (2016), the analysis of the range and conditions of their practical applicability to scattering can hardly be characterised as optimistic. Discrepancies

with experiment are observed to grow with increasing particle size and volume fractions, and these models become increasingly questionable.

Effective medium approximations can provide qualitative trends of the effective optical properties of particles (Potenza and Milani, 2014), yet a refinement of such models is often needed to provide quantitative results, as it will be examined in depth in chapter 4.

Scattering models

Delineating the link between the morphology of a particle and its optical properties is known as the *scattering problem*. Given a known electromagnetic field (wave) incident on a particle of known physical properties, the *direct scattering problem* consists in determining the internal field in the particle and in the medium in which it is embedded, hence the scattered field. It is generally a hard task which may be tackled by numerical computations. Conversely, solving the *inverse scattering problem* requires to recover the physical properties of the particle based on the measured scattered field. This is a common and more demanding situation, since the information available to the observer is often limited to a few optical quantities (see for example Torres et al. (2017)).

The large number of parameters involved in the process makes the inverse problem particularly hard to parse. For example, extinction depends to a large extent on particle size, yet its polarizability plays a non-negligible role which becomes decisive if the particle is strongly absorbing (Van de Hulst, 1981). In addition, particle shape hence orientation with respect to the light source, surface roughness, internal structure and composition all contribute to scattering affecting the efficiency with which a particle subtracts energy from the light source.

The Lorenz—Mie solution to Maxwell equations was the first attempt to solve the scattering problem. It is a rigorous formulation in terms infinite series, which covers the case of one isolated sphere of any dielectric constant and any size¹ (Mie, 1908). Other special cases such as the infinite cylinder, the ellipsoid and alike particles have been solved as well (Bohren and Huffman, 2008).

Originally derived for metal nanoparticles, it also gives an exact solution for dielectric spheres and converges to the limit of geometric optics (Horvath, 2009). For instance, this model is successfully used in the realm of metal-polymer nanocomposites, nanoparticles and clusters (see Minnai and Milani (2015), Potenza et al.

¹It has become widespread in scattering theory to denote as *Mie regime* the scattering from particles whose size is comparable to the wavelength, even though the Lorenz—Mie result holds for any sphere radius: its limitation is the particle shape.

(2016b), Minnai (2018) and references therein).

Recent experimental results showed that this model is effective in predicting the resonant absorption and other remarkable features of super-cooled water droplets, which can be considered very close to perfect spheres (Goy et al., 2018).

Despite dealing with simple geometrical shapes, the solution may require a high number of terms to converge, depending on the polarizability and size of the particle. Other models accounting, to some extent, for particle non-sphericity, are not as well-defined methodologically and are computationally demanding (Dubovik et al., 2006). The ideal setting of Mie scattering is rarely met in practical circumstances, so that this model loses its effectiveness on large scales, where irregular particles can hardly be approximated with spheres or point-like emitters (Fu et al., 2009, Mishchenko et al., 2000). For example, a theory for homogeneous spheres is unable to predict polarization effects or the extent of the scattering lobe correctly. Furthermore, spheres very close to each other exhibit interactions and electromagnetic coupling which fall beyond the approximations of Mie theory for the local field. We will not go into the details of the Lorenz–Mie model, but refer the reader to a complete description in Van de Hulst (1981) or Bohren and Huffman (2008).

As regards the Maxwell equations, exact solutions for real systems rapidly grow in complexity beyond practical use. To overcome this difficulty, many approximate theories have been developed, which can effectively describe different situations according to the assumptions they rely on (Bohren and Huffman, 2008, Van de Hulst, 1981).

There are a number of regimes for which appropriate models have been developed for a simplified approach to the problem (Jackson, 1999). The distinction between them is ultimately related to the relative length scales involved, i.e. the wavelength, λ , and the size a of the target (for instance, the diameter of a sphere). Otherwise stated, the wavelength sets the level of detail about which the scattered field contains information. The common guideline is to simplify as much as possible the scatterer in exchange for generality. The most relevant cases for our problem are the following:

- i) If the target is much smaller than the radiation wavelength, $a/\lambda \ll 1$, the lowest order induced multipoles are sufficient for an accurate description, the limiting case being an oscillating electric dipole representing a single molecule.
- ii) If such scales are comparable, the system requires a more general and more complex approach such as a multipole expansion or, more commonly, a numerical calculation (Kahnert, 2016).
- iii) Particles much larger than the wavelength fall in a regime ranging from

diffraction to the realm of geometrical optics. This is a very interesting feature of water droplets and small ice crystals in clouds, hail and precipitations (Ebert and Curry, 1992, Borghese et al., 2007, Leinonen et al., 2012, Van de Hulst, 1981, Fletcher et al., 2011, Wallace and Hobbs, 2006).

Approximation (ii) will be useful for describing micrometric particles with an appreciable degree of morphological complexity, while (i) will be employed to model their small elementary constituents (Born and Wolf, 2013, Goodman, 2005).

On a wider scale, light impinging on an extended collection of several interacting scatterers is a system in which the properties of its single constituents are somewhat blurred by the superposition of many signals². This is worsened by possible multiple scattering, correlations and polydispersity (Borghese et al., 2007). The difficulty of retrieving useful information from scattering measurements grows considerably and necessarily requires a statistical approach. The privileged point of view is the scattering from single particles, to which the response of an ensemble of many particles is inextricably linked (Bohren and Huffman, 2008). To sum up, the need for a theoretical model stems from two main issues: i) solving the direct problem can be analytically impossible in most cases, and collecting enough data to go beyond case specificity is time-consuming if handled with numerical methods. ii) the inverse problem is an ill-posed problem which usually cannot avoid rough approximations, and precious insight on the particle morphology becomes unreachable. The established approaches which regard the experimental conditions met in the present work will be the subject of the next sections. We will be highlighting the main hypotheses on which each model is based, with a particular focus on their interconnections and applicability. Once the background is set, an alternative, more general theoretical model will be proposed in section 2.5.

2.1 Towards composite particles: the structure factor

The morphology of a particle has a key role in scattering phenomena, and is one of the ingredients that must be included in any numerical calculation or theoretical model. While compact particles do not pose major technical difficulties when approximating their geometry and outer boundary, aggregates and particulate objects need a richer description which must include the density, size of their sub-constituents and possibly their arrangement inside the aggregate (Penttilä et al., 2007). This is where the structure factor comes into play.

Since this quantity is related to the density distribution of the system, it carries information about its structure and characteristic length scales (Sorensen and Wang,

²Unless the sensor is capable of achieving the so-called *cocktail party effect* described by Arons (1992).

1999). Formally, it is defined as follows:

$$S_s(\mathbf{q}) = \left| \int \rho(\mathbf{r}) e^{i\mathbf{q}\cdot\mathbf{r}} d\mathbf{r} \right|^2 \quad (2.1)$$

where \mathbf{r} runs over all the positions inside the volume of the particle, and $\rho(\mathbf{r})$ stands for the number density of its molecules, or more generally dipoles. This function is related to the pair correlation function³ $g(\mathbf{r})$: by the convolution theorem for the Fourier transform, equation (2.1) can be equivalently written as

$$S_s(\mathbf{q}) = \int g(\mathbf{r}) e^{i\mathbf{q}\cdot\mathbf{r}} d\mathbf{r} \quad (2.2)$$

where $g(\mathbf{r})$ is defined as the self-convolution of the density, namely:

$$g(\mathbf{r}) = \int \rho(\mathbf{x} - \mathbf{r}) \rho(\mathbf{x}) d\mathbf{x} \quad (2.3)$$

The variable \mathbf{r} in $g(\mathbf{r})$ stands for the vector joining the positions of a pair of particles. As these formulas suggest, the spatial arrangement of the scattering centres is encoded in this quantity. From an experimental point of view, it can be defined as the scattered intensity as a function of scattering angle or the scattering wave vector \mathbf{q} introduced in section 1.3. Equation (2.1) implies that the intensity scattered by the system is proportional to the square modulus of the Fourier transform of the density function.

In the case of an aggregate of N discrete dipoles, the integral is replaced by a sum over the positions of the particles. The density function can be written as a sum of Dirac delta distributions centred on the positions of the particles

$$\rho(\mathbf{r}) = \frac{1}{N} \sum_{i=1}^N \delta(\mathbf{r} - \mathbf{r}_i) \quad (2.4)$$

which yields

$$S_s(\mathbf{q}) = \frac{1}{N^2} \left| \sum_{j=1}^N e^{i\mathbf{q}\cdot\mathbf{r}_j} \right|^2 = \frac{1}{N^2} \sum_{i=1}^N \sum_{j=1}^N e^{i\mathbf{q}\cdot(\mathbf{r}_i - \mathbf{r}_j)} \quad (2.5)$$

the latter expression gives at glance some qualitative insight on the trend of $S_s(\mathbf{q})$ by comparing the distance between each pair of particles, $|\mathbf{r}_i - \mathbf{r}_j|$, with the modulus of the scattering vector, $q = |\mathbf{q}|$. If particles are considered point-like, the only relevant length scale is set by mutual distances and their corresponding range, which gives an estimate of the resolution of the scattering. If $q^{-1} > |\mathbf{r}_i - \mathbf{r}_j|$ the

³Sometimes referred to as density-density correlation function or radial distribution function.

scattered waves are going to add in phase and the intensity scales approximately as N^2 . Conversely, increasing the scattering angle gives large values of q^{-1} , hence $\mathbf{q} \cdot (\mathbf{r}_i - \mathbf{r}_j) > 1$. Here the phase of each scattered wave will vary considerably upon the specific particle being considered, giving rise to equally likely constructive and destructive interference, hence an overall (total) scattered intensity scaling as N (Sorensen, 2001). This justifies why for large articles we expect the scattering lobe to be more pronounced in the forward direction, while Rayleigh scatterers have an almost isotropic distribution of the irradiance (see later section 2.2, figure 2.2).

A universal expression for $S_s(q)$ can hardly be given even in the case of model aggregates (Teixeira, 1988, Sorensen et al., 1992, Sorensen and Wang, 1999, Lattuada et al., 2003). In many cases, the correlation function and consequently the structure factor are assumed to be isotropic, dropping the dependence on the direction of the vectors \mathbf{r} and \mathbf{q} respectively, and by only considering their moduli instead. This seemingly drastic simplification arises from averaging several statistical conformations and orientations, and is a reasonable scenario if the particles are able to move freely (Witten and Sander, 1983, Mishchenko and Yurkin, 2017). Thus

$$S_s(q) = \frac{1}{N^2} \langle \sum_{i,j} e^{i\mathbf{q} \cdot (\mathbf{r}_i - \mathbf{r}_j)} \rangle \quad (2.6)$$

where the sum runs over the coordinates \mathbf{r}_i of the N particles in the aggregate. If we consider a spherical particle with arbitrary radius a , the integral in (2.1) can be computed analytically

$$\int_{|\mathbf{r}| < a} \frac{1}{v} e^{i\mathbf{q} \cdot \mathbf{r}} d\mathbf{r} = \frac{3}{a^3} \int_0^a \frac{\sin(qr)}{qr} r^2 dr = 3 \frac{j_1(qa)}{qa} \quad (2.7)$$

where $j_1(qa)$ is the Spherical Bessel function. This expression only depends on the modulus of the wave vector and gives $S_s^{sph}(q)$ if squared. Thus, we can define the form factor of the particle as⁴

$$P(x) = \left| 3 \frac{j_1(x)}{x} \right|^2 = 9 \frac{|\sin(x) - x \cos(x)|^2}{x^6} \quad (2.8)$$

where $x = qa$. The dependence on the dimensionless product qa makes the size of such particles a critical parameter: as in basic diffraction theory, it determines the angular aperture of the forward scattering lobe.

⁴For sake of clarity, we should point out that the original definitions in solid state physics differ slightly from the ones usually adopted in optics. Specifically, they do not include the square modulus. In equation (2.5), the quantity in brackets is known as the geometric structure factor. Moreover, the atomic form factor or scattering factor is defined as the Fourier transform of the electron density of an atom. To this respect, the texts from Bushell et al. (2002) and Ashcroft and Mermin (2010) might be compared.

The relevance of equation (2.8) is twofold. In this work, we have vastly dealt with polystyrene beads, which can be considered homogeneous, spherical particles. Moreover, whenever the primary particles are much smaller than the wavelength, equation (2.8) is an adequate approximation of point-like scatterers whose shape is unperceivable (see section 2.2).

In summary, the structure factor of an aggregate of N identical particles can be factorised as the product of two contributions. The scattered intensity as a function of the scattering wavenumber is then

$$I(q) \sim S_s(q) \cdot P(qa) \quad (2.9)$$

The product $S_s(q) \cdot P(qa)$ might be thought of as the total structure factor of the aggregate, whenever the distinction between the aggregate and its primary constituents is possible.

In most practical cases, both $S_s(q)$ and $P(qa)$ have a maximum at $q = 0$ and are characterised by an overall decreasing trend with increasing q . The extent of such decrease is essentially given by $S_s(q)$, hence it is strongly dependent on the morphology of the particle.

2.2 Rayleigh scattering

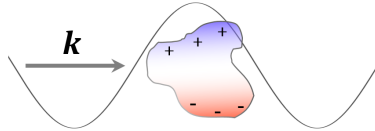


Figure 2.1: Heuristic schematic of a plane wave with wave vector \mathbf{k} inducing an (oscillating) electrical dipole in a small particle. The particle size and wavelength are not to scale.

Any particle much smaller than the wavelength behaves much like the electric dipole introduced in section 1.4, i.e. the fundamental unit identifiable in scattering theory. The assumption on size ensures that the external field varies slowly over the length scales which characterise the particle with which it interacts, so that all of the charges perceive a homogeneous field and collectively oscillate in phase (see figure 2.1). In this picture, known as Rayleigh scattering, the scattering amplitude is approximately given by

$$S(\theta) = \begin{pmatrix} S_2 & S_3 \\ S_4 & S_1 \end{pmatrix} = ik^3 \alpha \begin{pmatrix} \cos \theta & 0 \\ 0 & 1 \end{pmatrix} \quad (2.10)$$

where α may have an imaginary part accounting for absorption. If the incident light is not polarized, the scattered intensity $I(\theta)$ is proportional to⁵

$$|S(\theta)|^2 = k^6 |\alpha|^2 \frac{1 + \cos^2 \theta}{2} \quad (2.11)$$

The terms 1 and $\cos^2 \theta$ are related to the component of the incident field whose polarization is parallel or perpendicular to the scattering plane, respectively (see figure 2.2). As regards the polarizability, α , we can take the expression (1.21) from section 1.4.

Even a point-like approximation might take into account the size of the particle

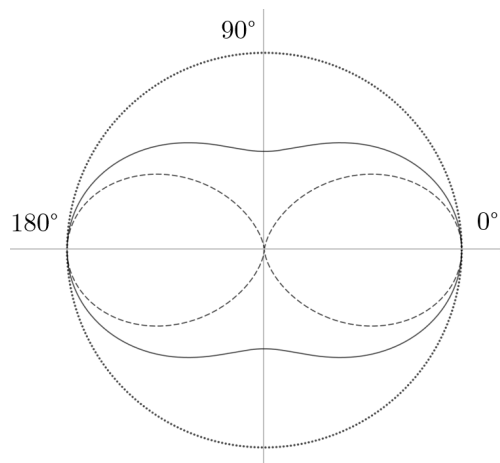


Figure 2.2: Angular normalised distribution of the irradiance of a particle in the Rayleigh scattering regime. The scattering plane is viewed from the top. Light polarized parallel to the scattering plane (dashed line) and perpendicular to the scattering plane (dotted line). The solid line represents unpolarized incident light, given by the normalised sum of the two previous cases.

to some extent, by including its form factor, $P(q(\theta)a)$ (equation (2.8)):

$$|S(\theta)|^2 = k^6 |\alpha|^2 P(q(\theta)a) \frac{1 + \cos^2 \theta}{2} \quad (2.12)$$

where $q(\theta) = 2k \sin \frac{\theta}{2}$. This is essentially a correction at large q values, and reduces to equation (2.11) for $a \rightarrow 0$ since $P \rightarrow 1$.

It is important to notice that, according to equation (1.1), the scattering amplitude

⁵The angular distribution resembles the Klein–Nishina scattering cross-section distribution in the Thomson limit (Klein and Nishina, 1929), which might be also compared to the scattering lobes derived from Mie theory.

defined above gives a scattered field in phase with the incident field. Since our goal is to explore the connections with the optical theorem, we need to refine this approximation by including a second order term at $\theta = 0$:

$$S(0) = ik^3\alpha + \frac{2}{3}k^6|\alpha|^2 \quad (2.13)$$

Higher order terms in $k^3\alpha$ might be considered to account for deviations from the Rayleigh regime. Let us now verify that the two terms in Eq. (2.13) are enough to give a complete picture. On one hand, if we substitute (2.10) in equation (1.4) for computing the integral of the intensity radiated at all angles by the particle we obtain

$$C_{\text{sca}} = \frac{1}{k^2} \int_{4\pi} |ik^3\alpha|^2 \frac{1 + \cos^2\theta}{2} d\Omega = \frac{8\pi}{3} k^4 \alpha^2 \quad (2.14)$$

by approximating the form factor $P(q) \simeq 1$. On the other hand, the second order term in (2.13) gives

$$C_{\text{ext}} = \frac{4\pi}{k^2} \Re S(0) = \frac{4\pi}{k^2} \frac{2}{3} k^6 \alpha^2 = \frac{8\pi}{3} k^4 \alpha^2 \quad (2.15)$$

i.e. the classical Rayleigh scattering cross section (Jackson, 1999). We note that if the particle is non absorbing, $C_{\text{sca}} = C_{\text{ext}}$, as it should.

Since α is proportional to the volume V of the particle, the term $k^3\alpha$ is small and $\Im S(0) \gg \Re S(0)$ (assuming α is real, see below). The modulus of the scattered field is then essentially due to the imaginary part of the scattering amplitude. Nonetheless, $S(0)$ cannot be a purely imaginary number: extinction can be traced back to the smaller term $\Re S(0)$, as a result of the optical theorem discussed in section 1.2. In some cases, overlooking this term is an acceptable approximation in so far as a small, non-absorbing particle removes almost no power from the light source ($a \rightarrow 0$). The phase of $S(0)$ is even more relevant for larger particles.

Absorbing particles have a complex polarizability, then

$$C_{\text{abs}} = -4\pi k \Im(\alpha) \quad (2.16)$$

Since α is an extensive physical quantity, absorption is proportional to the volume of the particle V , whereas scattering is proportional to V^2 : even a small absorption becomes the prevalent effect for very small particles. Beyond absorption, scattering has a very strong dependence on the wavelength which, for example, accounts for the colour of the sky.

For our purposes, the relevance of this regime lies in being the limiting case in which the constituent elements of more complex particles can be resolved. The incident wavelength offers a limited window of length scales beyond which it is not possible to extract information from a scattering experiment: we can model

as a Rayleigh dipole any particle whose substructures are too small to be probed, overlooking its shape.

For particles whose size is comparable to the wavelength and larger, this simplified

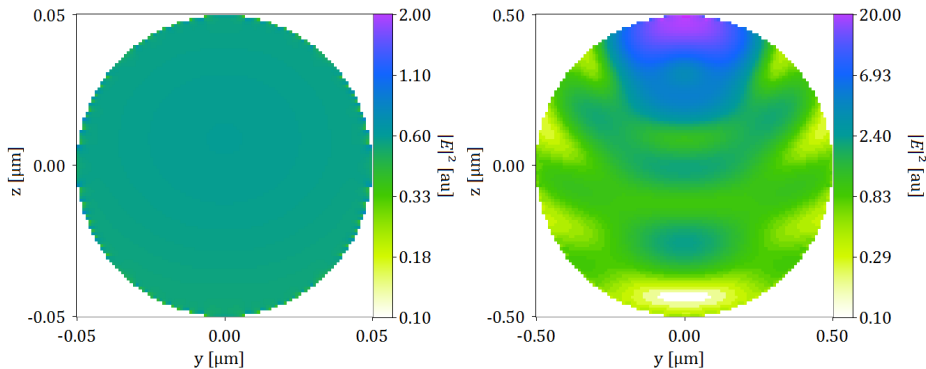


Figure 2.3: Diametrical section displaying the internal fields in a sphere falling under the Rayleigh regime $a/\lambda = 0.076$ (left) and a sphere with a radius ten times bigger $a/\lambda = 0.76$ (right). In the latter case, the particle size is comparable to the wavelength and the field exhibits a considerable variability.

picture must be replaced by other models which will be discussed in the following sections. As an example, in figure 2.3 we compare the internal electric fields in spherical water droplets of different sizes. In a droplet much smaller than the wavelength, the internal field is almost homogeneous, as discussed above. Considering a particle of the exact same material but ten times bigger, the internal field does not only grow in intensity, but exhibits clearly defined patterns and spatial variability. This is also reflected in the angular dependence of light scattering.

2.3 Rayleigh–Debye–Gans scattering

The Rayleigh–Debye–Gans (RDG) approximation builds upon the Rayleigh model seen in the previous section approaching the scattering problem for particles whose size is comparable to the wavelength, or larger. It provides the scattering and absorption cross sections for particles in the following validity domain (Bond and Bergstrom, 2006):

$$|m - 1| \ll 1 \quad (2.17a)$$

$$2k\ell|m - 1| \ll 1 \quad (2.17b)$$

where k is the incident radiation wavenumber, ℓ is a characteristic linear dimension of the particle⁶, and m is the relative refractive index relative to the surrounding medium, which may be complex. Both conditions must be met by the scatterer in order to conveniently describe its optical properties with this model. For example, the polystyrene sphere shown in figure 2.4 fails to meet the second condition. We made extensive use of such calibrated polymeric particles as a benchmark for our experimental measurements (see appendices A and B). In this case, the regular shape allows to determine the optical properties by Mie theory⁷.

In the RDG model, a particle is considered as an ensemble of small, non-interacting and independent units which can be treated in the Rayleigh limit, while contributions from multiple scattering and self-interaction are neglected (Farias et al., 1996). This theoretical framework is commonly used for modelling low-density aggregates (Sorensen, 2001).

Each small volume element δV in the particle is considered as an isolated dipole; its polarizability is given by equation (1.21)

$$\alpha = \frac{3}{4\pi} \frac{m_i^2 - 1}{m_i^2 + 2} \delta V \quad (2.18)$$

The field scattered by each sub-volume is written according to the Rayleigh limit and added in amplitude and phase (Bond and Bergstrom, 2006). Within the framework of this approximation, the scattering matrix of the aggregate, $S(\theta, \varphi)$, only depends on the scattering angle θ . Its elements S_3 and S_4 vanish, whereas S_1 and S_2 are found integrating over the volume of the particle (Van de Hulst, 1981)

$$S_1(\theta) = ik^3 \int \frac{3}{4\pi} \frac{m_i^2 - 1}{m_i^2 + 2} e^{i\mathbf{q}\cdot\mathbf{r}} \delta V \quad (2.19a)$$

$$S_2(\theta) = ik^3 \cos \theta \int \frac{3}{4\pi} \frac{m_i^2 - 1}{m_i^2 + 2} e^{i\mathbf{q}\cdot\mathbf{r}} \delta V \quad (2.19b)$$

where \mathbf{q} is the scattering vector while the position \mathbf{r} of each scattering centre gives the phase factor $e^{i\mathbf{q}\cdot\mathbf{r}}$.

Equations (2.19) show that scattering depends on the arrangement of its components: rearranging particle positions will affect the phases of the fields scattered by each particle and the resulting superposition. The same applies to a change in orientation if the particles are non-spherical. If the particles are spatially uncorrelated, so are the phases of the scattered fields.

⁶It corresponds to the radius in case of spheres.

⁷As regards the phase of $S(0)$, we observed that some polymeric beads exhibit a mild discrepancy with respect to the predictions of Mie theory, possibly because of deviations from the perfect spherical shape. Some results are presented in appendix B. An in-depth analysis of such phenomenon could be the subject for future work.

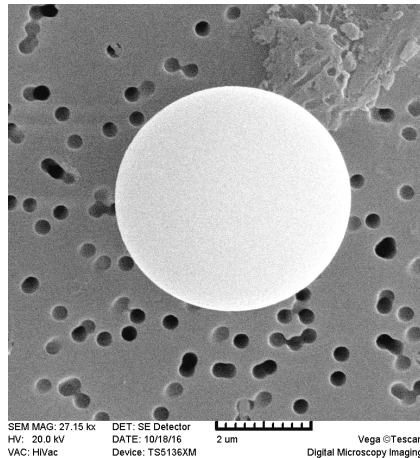


Figure 2.4: Scanning Electron Microscope image of a polystyrene spheres bead $5\text{ }\mu\text{m}$ in diameter. In water, the relative refractive index of this particle is $m \simeq 1.19$ at $\lambda = 0.635\text{ }\mu\text{m}$. While meeting the first requirement in equation (2.17), this particle fails to meet the second condition. In this case, however, the scattering amplitude can be calculated effectively with Mie theory.

Let us focus on an aggregate of N small, *identical* particles. In the far-field, the scattered electric field is given by

$$\mathbf{E}_s(\mathbf{q}) \sim \frac{1}{kr} \sum_{j=1}^N e^{i\mathbf{q} \cdot \mathbf{r}_j} \quad (2.20)$$

where \mathbf{q} is the scattering vector and \mathbf{r}_j is the position of each elementary unit, which keeps track of the internal structure of the aggregate. This equation reproduces well the intensity at any scattering angle $\theta > 0$. Nonetheless, according to the optical theorem, the phase-lag of the scattered field cannot be zero. Therefore, the left term in equation (2.20) must be multiplied by a phasor which can be derived from the optical cross sections. If the primary particles are far apart from each other (section 1.3), the phase of their scattering amplitude at $\theta = 0$ is a good approximation of the phase-lag of the whole aggregate.

The optical cross sections of the aggregate are approximated by simple functions of the scattering and absorption cross sections of the primary particles by assuming they act independently. Specifically, the RDG model predicts that absorption in sparse aggregates scales linearly with the number of its primary constituents

$$C_{\text{abs}}^{\text{tot}} = N C_{\text{abs}}^{\text{part}} \quad (2.21)$$

Conversely, the aggregate differential scattering cross section scales as N^2 :

$$\boxed{\frac{dC_{\text{sca}}^{\text{tot}}}{d\Omega} = N^2 S_s(\mathbf{q}) \frac{dC_{\text{sca}}^{\text{part}}}{d\Omega}} \quad (2.22)$$

where $S_s(\mathbf{q})$ is the structure factor of the aggregate⁸, $\frac{dC_{\text{sca}}^{\text{part}}}{d\Omega}$ is the differential scattering cross section of a single particle, which by equation (2.12) is

$$\frac{dC_{\text{sca}}^{\text{part}}}{d\Omega} = k^4 |\alpha|^2 \frac{1 + \cos^2 \theta}{2} P(q(\theta)a) \quad (2.23)$$

The above formulae usually provide a good agreement with light scattering data, for example with the static form factor (Sorensen et al., 1998, Ferri et al., 2015, Sorensen et al., 2018). Interestingly, this model coincides with the Mie model when considering many point-like particles arranged to form a sphere of radius R , i.e. taking $a \rightarrow 0$, $P(qa) \rightarrow 1$ and $S_s(\mathbf{q}) = P(qR)$ in equation (2.22).

Equation (2.22) implies that the optical properties of an aggregate are differ from those of the particles it comprises. Unlike the case of independent scatterers seen in section 1.3, here the extinction cross sections of the small particles do not simply add. Interestingly, while the structure factor appears in equation (2.22), it is missing in equation (2.21). In this picture, absorption is then proportional to the total volume or mass (Moosmüller et al., 2009), as was the case with the Rayleigh regime (section 2.2). From a microscopical perspective, this follows from assuming that the particle interacts weakly with the radiation, thus any molecule in the particle is exposed to approximately the same field. Atomic or molecular single-photon (linear) absorption processes are assumed to take place regardless the morphology of the particle. However, shape affects its radiation efficiency when the energy absorbed by the particle is eventually returned to the environment.

In our measurements, we have access to the zero-angle scattering amplitude, $S(0)$: let us build upon the equations seen so far to bridge the gap between RGD theory and this complex parameter.

In the forward direction we have $q = 0$, hence, combining (2.22) with equation (1.7) yields

$$\begin{aligned} \frac{dC_{\text{sca}}^{\text{tot}}}{d\Omega}(0) &= N^2 S_s(0) \frac{dC_{\text{sca}}^{\text{part}}}{d\Omega}(0) = N^2 k^4 |\alpha|^2 \overset{1}{S_s(0)} \overset{1}{P(0)} \\ &\Rightarrow |S(0)| = N k^3 |\alpha| \end{aligned} \quad (2.24)$$

This gives that the modulus of the forward scattering amplitude scales as the number of point-like particles in the aggregate, N . Assuming these are independent, the Maxwell-Garnett model outlined in section 1.5 may give an estimate of the

⁸Some of its features are briefly discussed in section 2.1

effective polarizability of the aggregate (Sorensen, 2001). By comparing equation (1.26) to equation (2.13) we may set $\alpha^{\text{eff}} = N\alpha$ and write

$$S(0) \simeq ik^3 \alpha^{\text{eff}} \quad (2.25)$$

Consequently, the forward scattered amplitude is essentially given by its imaginary part. On the other hand, we can combine equations (2.22) and (2.23) to write some explicit relations in the simplified case of a structure factor that only depends on the modulus of the scattering wave vector. By integrating equation (2.23), we obtain

$$\begin{aligned} C_{\text{sca}}^{\text{tot}} &= \int_{4\pi} \frac{dC_{\text{sca}}^{\text{tot}}}{d\Omega} d\Omega \\ &= N^2 k^4 |\alpha|^2 \int_{4\pi} S_s(q) P(qa) \frac{1 + \cos^2 \theta}{2} d\Omega \\ &= N^2 k^4 |\alpha|^2 2\pi \int_0^\pi S_s(q(\theta)) P(q(\theta)a) \frac{2 - \sin^2 \theta}{2} \sin \theta d\theta \\ &= 8\pi N^2 k^4 |\alpha|^2 \int_0^1 S_s(2kx) P(2kxa) [1 - 2x^2 + 2x^4] x dx \end{aligned} \quad (2.26)$$

where we have set $x = \sin \theta / 2$ for a more compact expression. This is essentially equivalent to the formula for the turbidity in Ferri et al. (2015). It is worth noting that, in the integral, the product $S_s \cdot P$ comes from the morphology of the particle and hence reflects a geometrical feature, whereas the electromagnetic nature of the physical phenomena involved here is taken into account in the term in square brackets.

If the particle is non absorbing, then $C_{\text{sca}}^{\text{tot}} = C_{\text{ext}}^{\text{tot}}$ and we obtain the real part of the scattering amplitude explicitly by the optical theorem (equation (1.12)):

$$\text{Re} S(0) = \frac{k^2}{4\pi} C_{\text{sca}}^{\text{tot}} = 2(Nk^3 |\alpha|)^2 \int_0^1 S_s(2kx) P(2kxa) [1 - 2x^2 + 2x^4] x dx \quad (2.27)$$

On the other hand, if the particle is absorbing, $\Re S(0)$ has an extra contribution due to C_{abs}

$$\text{Re} S(0) = \frac{k^2}{4\pi} (C_{\text{sca}}^{\text{tot}} + C_{\text{abs}}^{\text{tot}}) \quad (2.28)$$

We can finally write the complex scattering amplitude by piecing together equations (2.27) and (2.25):

$$S(0) \simeq ik^3 \alpha^{\text{eff}} + \frac{k^2}{4\pi} (C_{\text{sca}}^{\text{tot}} + C_{\text{abs}}^{\text{tot}}) \quad (2.29)$$

The assumption that the elementary units scatter independently is central to the RDG approximation. This condition is not strictly met in practice and there is,

moreover, a non-zero contribution from waves being scattered more than once. The conditions (2.17) ensure that these effects are negligible. However, the requirements in equations (2.17) should be checked with care, as in the following example, to which we will return in detail in chapter 4. According to effective medium approximations, sparse aggregates exhibit an *effective* refractive index close to unity (even in the presence of absorption) due to their small volume fraction (see section 1.5). While the RDG theory describes their features satisfactorily Sorensen et al. (2018), their morphology makes the use of effective medium approximations questionable: we would get the right answer for the wrong reason. Mishchenko et al. (2016), Wang and Sorensen (2002) and Farias et al. (1996) and discussed thoroughly the validity of these models.

2.4 Modelling of large compact particles

As we have seen in the previous section, it is straightforward to combine the RDG approximation with the effective medium approximation (section 1.5) and apply them to homogeneous spheres. More generally, a scattering regime named *Anomalous Diffraction* by Van de Hulst (1981) applies to particles larger than the wavelength that meet the conditions in (2.17). The physical interpretation is as follows:

- i) reflection and refraction at the boundaries of the scatterer are negligible;
- ii) going through the particle, the incoming wave suffers a small phase-shift.

Briefly, the real and imaginary part of the scattering amplitude at $\theta = 0$ of the particle is related to its size, a , and its relative refractive index, m , as follows:

$$S(0) = k^2 a^2 \left(\frac{1}{2} + \frac{e^{-i\rho}}{i\rho} + \frac{e^{-i\rho} - 1}{(i\rho)^2} \right) \quad (2.30)$$

where $\rho = 2ka|m - 1|$ is the *optical thickness*. Since $\rho \ll 1$, the two exponentials in $S(0)$ can be expanded up to the third and fourth order, respectively, which leads to a cancellation of many terms. Thus,

$$S(0) = k^2 a^2 \left(\frac{\rho^2}{8} + \frac{i\rho}{3} \right) + o(\rho^2) \quad (2.31)$$

If ρ is real,

$$\Re S(0) \simeq k^2 a^2 \frac{\rho^2}{8} \quad (2.32a)$$

$$\Im S(0) \simeq k^2 a^2 \frac{\rho}{3} \quad (2.32b)$$

These approximations provide a basis for interpreting the experimental results in chapters 3 and 4).

In the remainder of this section, we can finally outline a generalisation to non-spherical particles introduced by Villa et al. (2016). Taking their cue from the Anomalous Diffraction model outlined above, Villa et al. (2016) define $\tilde{\rho}(x, y) = k t(x, y) |m - 1|$, where $t(x, y)$ is the thickness of the particle evaluated at (x, y) along a line parallel to the z -axis, which coincides with the direction of propagation of the incident field (optical axis) intercepting the particle (figure 2.5). Then

$$S(0) = \frac{k^2}{2\pi} \int_{\Sigma} (1 - e^{-i\tilde{\rho}(x,y)}) dx dy \quad (2.33)$$

where the integral is computed over Σ , i.e. the cross-sectional area of the particle. If the optical thickness is small, the exponential can be expanded

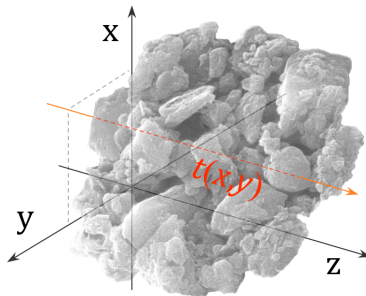


Figure 2.5: Schematic of the thickness of the particle as defined in the text.

$$S(0) \simeq i \frac{k^2}{2\pi} \int_{\Sigma} \tilde{\rho}(x, y) dx dy + \frac{k^2}{4\pi} \int_{\Sigma} \tilde{\rho}^2(x, y) dx dy \quad (2.34)$$

Let us assume a real optical thickness, so that $\Re S(0)$ and $\Im S(0)$ can easily be separated. The first term might be directly compared to the term $ik^3\alpha_{\text{eff}}$ of the Rayleigh–Debye–Gans regime (section 2.3). Using the integral average defined as

$$\langle \tilde{\rho} \rangle = \frac{1}{\Sigma} \int_{\Sigma} \tilde{\rho}(x, y) dx dy \quad (2.35)$$

we can write

$$\alpha_{\text{eff}} = \frac{1}{2\pi k} \int_{\Sigma} \tilde{\rho}(x, y) dx dy = \frac{\langle \tilde{\rho} \rangle \Sigma}{2\pi k} \quad (2.36)$$

We can separate $\tilde{\rho}$ into its average and deviations from its average, namely $\tilde{\rho}(x, y) = \langle \tilde{\rho} \rangle + \delta\tilde{\rho}(x, y)$. In particular, $\langle \tilde{\rho}^2 \rangle = \langle \tilde{\rho} \rangle^2 + \langle \delta\tilde{\rho}^2 \rangle$ because $\langle \delta\tilde{\rho} \rangle = 0$. By the optical theorem,

$$C_{\text{ext}} = \int_{\Sigma} \tilde{\rho}^2(x, y) dx dy = \Sigma \left(\langle \tilde{\rho} \rangle^2 + \langle \delta\tilde{\rho}^2 \rangle \right) \quad (2.37)$$

Thus

$$\Re S(0) = \frac{k^2 \Sigma}{4\pi} \left(\langle \tilde{\rho} \rangle^2 + \langle \delta \tilde{\rho}^2 \rangle \right) \quad (2.38a)$$

$$\Im S(0) = k^3 \frac{\langle \tilde{\rho} \rangle \Sigma}{2\pi k} \quad (2.38b)$$

These expressions suggest that $\tilde{\rho}$ is affected by both the average refractive index and the non-uniformities due to the internal structure and shape of the particle. As regards its interaction with electromagnetic radiation, these features are predominant compared to the refractive index, and to them can be ascribed the significant variability that is observed experimentally.

By definition, $\tilde{\rho}$ depends on the orientation of the particle with respect to the incident field, although the averages appearing in equations (2.38) do not explicitly depend on x, y .

Following the notation by Villa et al. (2016), we associate to a particle of arbitrary morphology an optical thickness given by

$$\rho = \frac{2\Re S(0)}{\Im S(0)} = \langle \tilde{\rho} \rangle + \frac{\langle \delta \tilde{\rho}^2 \rangle}{\langle \tilde{\rho} \rangle} \quad (2.39)$$

In summary, the optical thickness can be related to two fundamental parameters of the scatterer, namely the refractive index, m , and the effective geometrical thickness, t :

$$\rho \sim t \cdot |m - 1| \quad (2.40)$$

while the first parameter accounts for the composition of the particle and is responsible for the strength of the interaction with light, the latter is affected by shape and orientation.

2.5 A molecular optics approach

Having discussed some well-established, approximate models in sections 2.2 and 2.3, we close this chapter by proposing an alternative model based on a recent publication by Parola et al. (2014). It gives a perturbative expression for the scattered field by including the interactions between the dipoles in the system and the effect of correlations⁹. Its derivation is based on molecular optics. This brings us closer to a more suitable point of view for describing the features of complex particles, since it deals with optical phenomena from a microscopic perspective.

Let us consider a linearly polarized harmonic plane wave with frequency ω incident

⁹This section is a concise summary of the notes from Professor Alberto Parola from Insubria University in Como, with whom we collaborated, and whom we would like to thank for his precious advice and fundamental contribution to this thesis.

on a particle with an arbitrary structure. As introduced in sections 1.4 and 2.2, every polarizable molecule in the system behaves as an oscillating dipole $\mathbf{p} = \mathbf{p}_0 e^{-i\omega t}$, oriented parallel to the incident field \mathbf{E}_0 . The complete expression for the electric field radiated by a dipole \mathbf{E}_d , as a function of time t and space coordinate \mathbf{r} is given by the real part of the following expression (Jackson, 1999)

$$\mathbf{E}_d(\mathbf{r}, t) = k^3 \left[\frac{1}{kr} (\mathbf{n} \times \mathbf{p}) \times \mathbf{n} + (3\mathbf{n}(\mathbf{n} \cdot \mathbf{p}) - \mathbf{p}) \left(\frac{1}{k^3 r^3} - \frac{i}{k^2 r^2} \right) \right] e^{ikr - i\omega t} \quad (2.41)$$

where k is the wavenumber of the incident field, \mathbf{n} is a unit vector in the direction of \mathbf{r} , whose modulus is indicated by r . The first term in the brackets is the only one being considered in the far-field approximation, and gives the Rayleigh model of section 2.2. The two other terms, scaling as r^{-3} and r^{-2} , respectively, are the contributions to the near-field, which affect the local field acting on the neighbouring particles. It is common to neglect these terms for low-density scatterers, since they vanish rapidly with growing distances. Nevertheless, their contribution is essential in systems which exhibit correlations (Parola et al., 2014). If the dipoles are not isolated, the local field at a given point is affected to some extent by all neighbouring dipoles, hence, so is the scattered field. In this case the derivation is less straightforward, and will be the subject of the following pages.

2.5.1 General form of the forward scattering amplitude

For later convenience, let us rewrite equation (2.41) using a tensor notation:

$$E_d^\mu(\mathbf{r}, t) = k^3 \Gamma^{\mu\nu} p_0^\nu e^{ikr - i\omega t} \quad (2.42)$$

where repeated (lower-case Greek) indices are implicitly summed over. The dimensionless tensor $\Gamma^{\mu\nu}(\mathbf{r})$ governing the field radiated by each dipole in the system is given by the following expression

$$\Gamma^{\mu\nu}(\mathbf{r}) = \frac{1}{kr} (\delta^{\mu\nu} - n^\mu n^\nu) + (3n^\mu n^\nu - \delta^{\mu\nu}) \left(\frac{1}{k^3 r^3} - \frac{i}{k^2 r^2} \right) \quad (2.43)$$

where n^μ is the radial unit vector appearing in equation (2.41). We consider a confined distribution of particles illuminated by a harmonic plane wave $E_0^\mu(\mathbf{r}, t) = \mathcal{E}^\mu e^{i\mathbf{k} \cdot \mathbf{r} - i\omega t}$, which by definition is such that $k^\mu \mathcal{E}^\mu = 0$. Now, following Parola et al. (2014), we can write the total electric field as

$$E^\mu(\mathbf{r}, t) = E_0^\mu(\mathbf{r}, t) + \alpha k^3 \sum_j \Gamma^{\mu\nu}(\mathbf{r} - \mathbf{r}_j) E_j^\nu(\mathbf{r}_j, t) e^{ik|\mathbf{r} - \mathbf{r}_j|} \quad (2.44)$$

The sum runs over all the dipoles in the particle. $E_j^\nu(\mathbf{r}_j, t)$ is the local field around the j -th dipole¹⁰. It is worth noting that this includes the contribution of all the

¹⁰With the notation adopted here, equation (1.19) becomes $p_j^\nu(t) = \alpha E_j^\nu(\mathbf{r}_j, t)$.

other dipoles in the system. Both the radiative and near-field of each dipole is being considered in this expression, alongside with their arrangement in the particle. To go any further, the path essentially splits now into two different approaches. Equations (2.44) may be solved by iterative methods, for example following Yurkin and Hoekstra (2007). Alternatively, one can take advantage of some simplifications to pursue an analytical solution. An expansion to second order in the dimensionless polarizability, defined here as $\tilde{\alpha} = \alpha k^3$, leads to the perturbative expression by Parola et al. (2014)

$$E^\mu(\mathbf{r}, t) = E_0^\mu(\mathbf{r}, t) + \tilde{\alpha} \sum_j \Gamma^{\mu\nu}(\mathbf{r} - \mathbf{r}_j) E_0^\nu(\mathbf{r}_j, t) e^{ik|\mathbf{r} - \mathbf{r}_j|} \\ + \tilde{\alpha}^2 \sum_{j \neq l} \Gamma^{\mu\nu}(\mathbf{r} - \mathbf{r}_j) \Gamma^{\nu\xi}(\mathbf{r}_j - \mathbf{r}_l) E_0^\xi(\mathbf{r}_l, t) e^{ik|\mathbf{r} - \mathbf{r}_j|} e^{ik|\mathbf{r}_j - \mathbf{r}_l|} \quad (2.45)$$

This approximation dramatically simplifies equation (2.44).

Going a step further, if the total electric field is evaluated outside the distribution, at a large distance from the particle ($r \gg r_j \forall j$), we may take the far-field limit and write

$$E^\mu(\mathbf{r}, t) = \mathcal{E}^\mu e^{i\mathbf{k} \cdot \mathbf{r} - i\omega t} + \tilde{\alpha} \frac{e^{ikr - i\omega t}}{kr} \sum_j (\delta^{\mu\nu} - n^\mu n^\nu) \mathcal{E}^\nu e^{i\mathbf{k} \cdot \mathbf{r}_j} e^{-ik\mathbf{n} \cdot \mathbf{r}_j} + \\ \tilde{\alpha}^2 \frac{e^{ikr - i\omega t}}{kr} \sum_{j \neq l} (\delta^{\mu\nu} - n^\mu n^\nu) \Gamma^{\nu\xi}(\mathbf{r}_j - \mathbf{r}_l) \mathcal{E}^\xi e^{-ik(\mathbf{n} \cdot \mathbf{r}_j + |\mathbf{r}_j - \mathbf{r}_l|)} e^{i\mathbf{k} \cdot \mathbf{r}_l} \quad (2.46)$$

where $\mathbf{n} = \frac{\mathbf{r}}{r}$. In the forward direction $\mathbf{r} \parallel \mathbf{k}$, hence $k\mathbf{n} = \mathbf{k}$ and we can simplify to a certain degree the exponentials in the sums. Thus

$$E^\mu(\mathbf{r}, t) = \mathcal{E}^\mu e^{i\mathbf{k} \cdot \mathbf{r} - i\omega t} + \frac{i}{kr} S^{\mu\nu}(0) \mathcal{E}^\nu e^{ikr - i\omega t} \quad (2.47)$$

As we did in equation (1.1), the scattered field is written in terms of the scattering amplitude in the forward direction $S^{\mu\nu}(0)$, which is defined as

$$i S^{\mu\nu}(0) = N \tilde{\alpha} \delta^{\mu\nu} + \tilde{\alpha}^2 (\delta^{\mu\xi} - n^\mu n^\xi) \sum_{j \neq l} \Gamma^{\xi\nu}(\mathbf{r}_j - \mathbf{r}_l) e^{-i\mathbf{k} \cdot (\mathbf{r}_j - \mathbf{r}_l)} e^{ik|\mathbf{r}_j - \mathbf{r}_l|} \quad (2.48)$$

expanded to second order in $\tilde{\alpha} = \alpha k^3$. N is the number of dipoles in the sum, to which is proportional the first order term of $S^{\mu\nu}(0)$, whereas its second order term will be shown to scale as N^2 in the following steps. We may now write the scattering amplitude replacing the sum over all the molecules with an integral by introducing the particle radial distribution function¹¹ $\mathcal{N}(\mathbf{r}, \mathbf{r}') = \langle \sum_{i \neq j} \delta(\mathbf{r} - \mathbf{r}_i) \delta(\mathbf{r}' - \mathbf{r}_j) \rangle$

$$i S^{\mu\nu}(0) = N \tilde{\alpha} \delta^{\mu\nu} + \tilde{\alpha}^2 (\delta^{\mu\xi} - n^\mu n^\xi) \int d\mathbf{r} d\mathbf{r}' \mathcal{N}(\mathbf{r}, \mathbf{r}') \Gamma^{\xi\nu}(\mathbf{r} - \mathbf{r}') e^{-i\mathbf{k} \cdot (\mathbf{r} - \mathbf{r}')} e^{ik|\mathbf{r} - \mathbf{r}'|} \quad (2.49)$$

¹¹The average is taken on the appropriate molecular distribution.

In the case of an aggregate of many small particles falling in the Rayleigh regime, these can be represented by spherical particles of radius a and volume $v = \frac{4}{3}\pi a^3$, each of which encompasses a large number of molecules. Without loss of generality, we may assign to the primary particles a volume-equivalent radius. We shall shift our focus on such monomers with polarizability α given by equation (1.22) (section 1.4). By the same steps described in (Parola et al., 2014), the scattering amplitude can be written as

$$i S^{\mu\nu}(0) = N\tilde{\alpha}\delta^{\mu\nu} + \tilde{\alpha}^2 (\delta^{\mu\xi} - n^\mu n^\xi) \int d\mathbf{r} d\mathbf{r}' [\rho(\mathbf{r})\delta(\mathbf{r} - \mathbf{r}') + g(\mathbf{r}, \mathbf{r}')] K^{\xi\nu}(\mathbf{r}, \mathbf{r}') \quad (2.50)$$

where $\rho(\mathbf{r})$ is the density of particles and $g(\mathbf{r}, \mathbf{r}')$ is the correlation function. The integral kernel $K^{\xi\nu}(\mathbf{r}, \mathbf{r}')$ is given by

$$K^{\xi\nu}(\mathbf{r}, \mathbf{r}') = \int \frac{d\mathbf{x} d\mathbf{x}'}{v^2} \theta(a - |\mathbf{x} - \mathbf{r}|) \theta(a - |\mathbf{x}' - \mathbf{r}'|) \Gamma^{\xi\nu}(\mathbf{x} - \mathbf{x}') e^{-i\mathbf{k}\cdot(\mathbf{x}-\mathbf{x}')} e^{ik|\mathbf{x}-\mathbf{x}'|} \quad (2.51)$$

where θ is the Heaviside step function. We now need to take the Fourier transform of the kernel

$$\begin{aligned} K^{\xi\nu}(\mathbf{q}) &= P(qa) \int d\mathbf{r} e^{-i(\mathbf{k}-\mathbf{q})\cdot\mathbf{r}} e^{ikr} \Gamma^{\xi\nu}(\mathbf{r}) \\ &= \frac{4\pi}{k^3} P(qa) \left[\frac{k^2 \delta^{\xi\nu} - (\mathbf{k} - \mathbf{q})^\xi (\mathbf{k} - \mathbf{q})^\nu}{|\mathbf{k} - \mathbf{q}|^2 - k^2 - i\eta} + \frac{\delta^{\xi\nu}}{3} \right] \end{aligned} \quad (2.52)$$

where $P(qa)$ is the form factor introduced in equation (2.8). The last term arises from excluding a neighbourhood of $\mathbf{r} = 0$, while η is a real parameter to be brought to zero after integration. Thus

$$\begin{aligned} i S^{\mu\nu}(0) &= N\tilde{\alpha}\delta^{\mu\nu} + \\ &\tilde{\alpha}^2 (\delta^{\mu\xi} - n^\mu n^\xi) \int \frac{d\mathbf{q}}{2\pi^2 k^3} P(qa) G(\mathbf{q}) \left[\frac{k^2 \delta^{\xi\nu} - (\mathbf{k} - \mathbf{q})^\xi (\mathbf{k} - \mathbf{q})^\nu}{|\mathbf{k} - \mathbf{q}|^2 - k^2 - i\eta} + \frac{\delta^{\xi\nu}}{3} \right] \end{aligned} \quad (2.53)$$

where

$$G(\mathbf{q}) = \int d\mathbf{r} d\mathbf{r}' [\rho(\mathbf{r})\delta(\mathbf{r} - \mathbf{r}') + g(\mathbf{r}, \mathbf{r}')] e^{-i\mathbf{q}\cdot(\mathbf{r}-\mathbf{r}')} \quad (2.54)$$

Taking an average over all possible orientations (Mishchenko and Yurkin, 2017) we imply spherical symmetry

$$G(q) = \left\langle \sum_{ij} e^{i\mathbf{q}\cdot(\mathbf{r}_i - \mathbf{r}_j)} \right\rangle \equiv N^2 S_s(q) \quad (2.55)$$

where \mathbf{r}_i are the coordinates of the constituent particles and $S_s(q)$ is the structure factor defined in equation (2.6).

The scattering amplitude is shown to be diagonal by recalling that in the forward direction the electric field is orthogonal to \mathbf{k} . The final expression for the forward scattering amplitude is then

$$\begin{aligned}
 S(0) &= \frac{N\tilde{\alpha}}{i} + \frac{N^2\tilde{\alpha}^2}{i} \int \frac{d\mathbf{q}}{4\pi^2k^3} P(qa) S_s(q) \left(\frac{2k^2 - q^2 + (\mathbf{q} \cdot \mathbf{k}/k)^2}{|\mathbf{k} - \mathbf{q}|^2 - k^2 - i\eta} + \frac{2}{3} \right) \\
 &= -iN\tilde{\alpha} + \frac{N^2\tilde{\alpha}^2}{4} \int_0^{2k} \frac{dq}{k^2} q P(qa) S_s(q) \left(2 - \frac{q^2}{k^2} + \frac{q^4}{4k^4} \right) \\
 &\quad + \frac{iN^2\tilde{\alpha}^2}{4\pi} \int_0^\infty \frac{dq}{k^2} q P(qa) S_s(q) \left[\frac{q^3}{k^3} - \frac{8q}{3k} + \left(2 - \frac{q^2}{k^2} + \frac{q^4}{4k^4} \right) \ln \frac{|q - 2k|}{q + 2k} \right]
 \end{aligned} \tag{2.56}$$

Note that the term $N\tilde{\alpha}$ here acts as an expansion parameter, whereas according to the mean field approximation $N\tilde{\alpha}$ coincides with the total polarizability of an aggregate of N particles (equation (1.26)). For the sake of convenience, we may set $x = \frac{q}{2k}$ in the integrals and define:

$$C_1 := 2 \int_0^1 dx P(2xka) S_s(2xk) (x - 2x^3 + 2x^5) \tag{2.57a}$$

$$C_2 := \frac{2}{\pi} \int_0^\infty dx P(2xka) S_s(2xk) \left[4x^4 - \frac{8}{3}x^2 + (x - 2x^3 + 2x^5) \ln \frac{|x - 1|}{x + 1} \right] \tag{2.57b}$$

The forward scattering amplitude, $S(0)$, assumes then a more compact form

$$S(0) = -iN\tilde{\alpha} + C_1 N^2\tilde{\alpha}^2 + iC_2 N^2\tilde{\alpha}^2 \tag{2.58}$$

Let us take a closer look to the polarizability before we proceed to separate the real and imaginary part of the scattering amplitude. In general, we may assign to each particle a (complex) relative refractive index $m + i\kappa$, where κ is the imaginary part accounting for absorption. Multiplying equation (1.21) by k^3 , this yields the dimensionless polarizability

$$\tilde{\alpha} = \frac{3k^3v}{4\pi} \frac{(m^2 + \kappa^2)^2 + m^2 - \kappa^2 - 2 + i6m\kappa}{(m^2 + \kappa^2)^2 + 4(m^2 - \kappa^2)^2 + 4} \tag{2.59}$$

We note that the real part of $\tilde{\alpha}$ is positive, as it should, since $m > 1$.

If $m \gg \kappa$, it can be approximated to first order in κ as

$$\tilde{\alpha} \simeq \frac{3k^3v}{4\pi} \left(\frac{m^2 - 1}{m^2 + 2} + i \frac{6m\kappa}{(m^2 + 2)^2} \right) \tag{2.60}$$

Hence, setting $\tilde{\alpha}_r := \Re \tilde{\alpha}$ and $\tilde{\alpha}_i := \Im \tilde{\alpha}$, we can separate the real and imaginary part of $S(0)$ in equation (2.57) as

$$\Re S(0) = N\tilde{\alpha}_i + C_1 N^2(\tilde{\alpha}_r^2 - \tilde{\alpha}_i^2) - 2C_2 N^2\tilde{\alpha}_r\tilde{\alpha}_i \tag{2.61a}$$

$$\Im S(0) = -N\tilde{\alpha}_r + C_2 N^2(\tilde{\alpha}_r^2 - \tilde{\alpha}_i^2) + 2C_1 N^2\tilde{\alpha}_r\tilde{\alpha}_i \tag{2.61b}$$

We may now specify these formulas in the case of a real polarizability¹²

$$\Re S(0) = C_1 N^2 \tilde{\alpha}^2 \quad (2.62a)$$

$$\Im S(0) = -N\tilde{\alpha} + C_2 N^2 \tilde{\alpha}^2 \quad (2.62b)$$

The first term in $\Im S(0)$ corresponds to the RDG approximation discussed earlier, where the scattering amplitudes of all the non-interacting dipoles sum up coherently and the aggregate behaves as a single dipole of polarizability $N\tilde{\alpha}$. The effects of spatial correlations between monomers appear only in the second order terms, which depend on both the monomer form factor and the cluster structure factor, hence the morphology of the particle. We find that correlations do not affect $\Im S(0)$ significantly, since the second order term constitutes a small correction. Conversely, they are decisive in $\Re S(0)$ given the absence of the first order term ($\sim N\tilde{\alpha}$). This complies with the Optical Theorem. In section 4.5, it will be shown that, for low-density aggregates, the second term appearing in the expression (2.62b) is negligible compared to $N\tilde{\alpha}$, and that the modulus of the forward scattering amplitude is essentially given by $|\Im S(0)|$.

As mentioned above, this model guarantees good accuracy to second order in the (dimensionless) polarizability. Moreover, it exhibits a degree of versatility. It can be shown that, with the proper assumptions, it reduces to the simpler models seen in the previous sections of this chapter. For example, by taking $ka \rightarrow 0$ and $kR_g \rightarrow 0$ so that $P(2kx)S(2kx) = 1$, equation (2.62a) can be easily integrated giving $\Re S(0) = \frac{2}{3}N^2(\alpha k^3)^2$ so that $C_{\text{ext}} = \frac{8\pi}{3}N^2\alpha^2 k^4$, which coincides with Rayleigh scattering from non-absorbing particles (Bohren and Huffman, 2008).

Furthermore, if we multiply equation (2.62a) by $\frac{k^2}{4\pi}$ we obtain

$$\frac{k^2}{4\pi}\Re S(0) = 8\pi N^2 k^4 |\alpha|^2 \int_0^1 S_s(2kx)P(2kx)[1 - 2x^2 + 2x^4]x \, dx \quad (2.63)$$

which is equivalent to the scattering cross section in equation (2.27). This means that we can infer the correct real part of the scattering amplitude, $\Re S(0)$, from the RDG approximation¹³, provided that $\tilde{\alpha}$ is real and much smaller than 1. This also constitutes an independent proof the optical theorem is complied with. The model given here is a unified derivation of the scattering properties of arbitrarily shaped particles in terms of their structure factor, whereas in the RDG model scattering and absorption are treated separately (see equations (2.22) and (2.21)).

¹²In the experimental part of this thesis we will consider polystyrene and dielectric mineral dust suspended in water.

¹³This result of the RDG theory assumes non-absorbing particles, for which $C_{\text{ext}} = C_{\text{sca}}$. Conversely, the model presented in this section does not need such assumption.

From a structural perspective, any particle consisting of many small entities will necessarily exhibit correlations between its constituents — however low its overall density may be — since those must adhere to one another. On the other hand, there is a certain degree of anti-correlation in that particles cannot intercept each other (excluded volume contribution). Such correlations are shown to have a tangible effect on the radiative properties of the particle. The structure factor appearing in equations (2.62a) and (2.62b) ensures these features are included in the scattering model.

Far apart, small particles are well described as emitting dipoles falling under the Rayleigh scattering regime, as seen in section 1.3. The closer they come to each other the stronger the coupling of the internal electromagnetic fields will be, until they can no longer be considered independent (Mishchenko, 2018). With an argument similar to that set out in Sorensen (2001), it can be stated that the incident wave vector determines the relevant length scale of the region below which there is no way of distinguishing the spatial distribution of the mass in an aggregate. For any length scale above this limit, the internal structure of the system cannot safely be disregarded. In particular, this applies even if the primary constituents are conceivable as point-like scatterers, i.e. they are much smaller than the incident wavelength.

We will proceed to examine a survey of applications to some special cases in chapter 4 (see figure 4.11); some further comments on this model will be given in section 4.5.

Mineral dust

Even the clearest sky¹ conceals countless solid and liquid particles in the nanometre and micrometre size range, suspended up to the stratosphere (Seinfeld and Pandis, 2016). Two natural sources of aerosol prevail due to their large extension over the Earth’s surface: oceans and deserts. Sparsely vegetated regions with rainfall lower than $\sim 250 \text{ mm yr}^{-1}$ entrain into the atmosphere tiny soil particles, known as mineral dust, via aeolian processes² (Field et al., 2010, Kok et al., 2012). Similarly, wind is responsible for the release into the atmosphere of ions and other corpuscles found in seawater such as microalgae (Marks, 1987, Vogt et al., 1996, Tesson et al., 2016). In addition, anthropogenic pollutants and particles emitted by volcanoes contribute to the load of atmospheric particulates, primarily with metal-rich particles and carbonaceous aggregates (Charlson et al., 1992, Hinkley et al., 1999, Mather et al., 2003, Rauch and Pacyna, 2009, Vallelonga et al., 2010, Burgay et al., 2019). Piazzalunga et al. (2013) gives a comprehensive chemical characterisation of aerosol composition.

3.1 Relevance of mineral dust aerosol

Among all aerosol types, mineral dust from both natural and anthropogenic sources boasts a prominent mass contribution to the particle load in the troposphere (Bond et al., 2013). These together constitute the second most abundant aerosol after sea salt and has the highest average optical thickness (Prospero et al., 2002). Estimates based on global climate models set this contribution between 800 Tg yr^{-1} and 2000 Tg yr^{-1} (Zender et al., 2004) which exceeds 50% of aerosol total dry mass (Miller et al., 2006), a large portion of which ($\sim 60\%$) originates from northern Africa (low-latitude deserts). As an example, a comparison of current to Last Glacial Maximum dust load profiles [$\mu\text{g}/\text{m}^2$] is shown in figure 3.1.

¹See for example Rondanelli et al. (2015) or Kenyon and Storey (2006).

²Aeolian processes include erosion, emission, transport, and deposition of particles by wind.

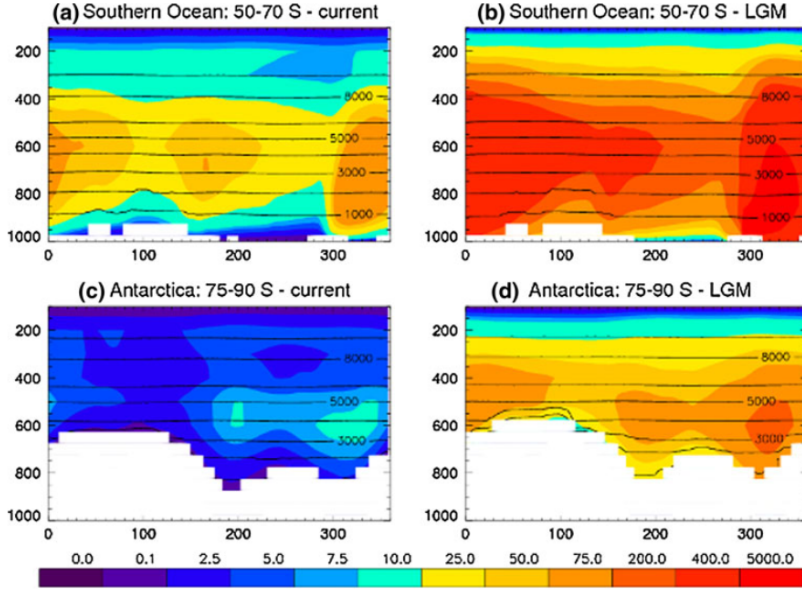


Figure 3.1: Comparison of current to Last Glacial Maximum dust load. The vertical profiles [$\mu\text{g}/\text{m}^2$] are averaged over two distinct latitudinal bands: 50° – 70° S (Southern Ocean) and 70° – 90° S (Antarctica). Longitude is reported on the x-axis, while pressure is shown on the y-axis with black lines indicating height above sea level (in metres). Taken from Albani et al. (2012).

A variety of other factors contribute to the importance of mineral dust, many of which are ultimately related to its atmospheric lifetime and mineral flux range, therefore to its size distribution (see for example Kok et al. (2012)). For example, bioavailable iron and phosphorus carried and released by mineral aerosol in aquatic ecosystems are known to fertilise and impact the bio-geochemical cycles of oceans and seas (Mahowald et al., 2005, Spolaor et al., 2012, Kjær et al., 2015). In turn, bacteria and phytoplankton of such environments affect the nitrogen and carbon dioxide content of the oceans (Mahowald et al., 2009, Winton et al., 2014, Babin and Stramski, 2002, Marín et al., 2017). The supply of essential nutrients is particularly relevant in surface waters of remote mineral-poor ecosystems (Neff and Bertler, 2015). Dust can also serve as a reaction surface for gases in the atmosphere and can moderate photochemical processes (Prospero et al., 2002).

The basic mechanisms which underlie the deflation of dust from continental land-masses and spread into the atmosphere are the collisions of saltating particles with the surface and sandblasting (Lawrence and Neff, 2009). The efficiency of such pro-

cesses and the size distribution of the resulting products depend on the mineralogy of the soil as well as on its tendency to liberate smaller particles (Ruth, 2002).

In general, dust can undergo long-range transport, which makes seemingly regional sources grow in importance and have tangible effects on a global scale (Balkan-ski et al., 2007). Travel distance is related to atmospheric lifetime, which in turn depends on the size of the particle and ranges between one day and one week approximately. Dust size may range from a few nanometres to several tens of microns, the largest among atmospheric aerosol particles (Mahowald et al., 2014). One of the main features differentiating the optical properties of dust from other aerosol particles such as biomass burning and anthropogenic aerosols is, in fact, the abundance of large grains greater than $\sim 1.2\text{ }\mu\text{m}$ (Dubovik et al., 2002). However, only particles smaller than about $10\text{ }\mu\text{m}$ in diameter are subject to long-range transport (Moosmüller et al., 2012).

The aerosol load is one of the essential parts of the Earth climate system, as established by a significant amount of studies (Haywood and Boucher, 2000, Ridgwell, 2002, Maher et al., 2010, Nousiainen et al., 2011). Atmospheric aerosol impacts the radiative budget directly by scattering and absorbing solar radiation and downwelling terrestrial thermal (infrared) radiation. This can result either in a positive or negative feedback depending on the surface reflectance of the land or water underneath (Haywood and Boucher, 2000). Moreover, aerosol particles affect the hydro-geological cycle by serving as nucleation sites for droplets and ice crystals in clouds. Not only do they cause an increase in droplet concentration, but also a decrease in average droplet size³. This influences the microphysical properties of a cloud, such as their lifetime and precipitation efficiency (Kaufman et al., 2005). In turn, clouds interact with light to the extent of their optical thickness, albedo and lifetime, yielding either a cooling or warming effect in the short-wave and long-wave range respectively (Ebert and Curry, 1992, Haywood and Boucher, 2000).

It has been observed that a critical feature linking cloud characteristics to dust is the size distribution of the latter (Dusek et al., 2006). The feedback related to dust aerosol has been found to contribute to the temperature increase in the Arctic regions, which are experiencing a trend twice as fast as the rest of the globe. Some authors agree that the evolving aerosol properties caused an overall increase in temperature of $\sim 1\text{ }^{\circ}\text{C}$ on a global scale, and up to $\sim 1.5\text{ }^{\circ}\text{C}$ in the Arctic (see Ferrero et al. (2019), Kylling et al. (2018) and references therein). These estimates include anthropogenic aerosol and pollutants characterised by high absorption such as carbon aggregates. In this respect, a variety of studies have established that carbon aggregates such as soot have a decisive impact on climate. For instance, as

³The thermodynamic conditions needed for homogeneous nucleation of water in the atmosphere are extremely rare, whereas heterogeneous nucleation requires a much lower relative humidity. The comparison here refers to other aerosol particles such as ion impurities (Fletcher et al., 2011).

reported by Jacobson (2001) direct radiative forcing from black carbon alone exceeds in magnitude the forcing due to methane, suggesting that black carbon may be the second most important component of global warming after carbon dioxide. This feature is deeply related to its extraordinary absorption properties (Kahnert et al., 2012, Vecchi et al., 2014, Massabò et al., 2015).

The radiative properties of such particles would require a thorough treatment which is out of the scope of the present thesis, albeit it may be one of its natural progressions. Here we will focus on samples for which scattering is stronger than absorption.

Much uncertainty still exists about the effect of mineral dust on the climate system, e.g. with respect to its effects on synoptic scale climate and tropospheric heating Stocker (2014). The constant renewal of dust population as a consequence of the relatively short lifetime of mineral particles in the atmosphere also emerges as a considerable obstacle. Moreover, tropospheric aerosol emissions and distribution, as well as land surface reflectivity, suffer from a large spatial and temporal variability, which makes estimates very uncertain (Prospero et al., 2002, Kaufman and Koren, 2006). Overall, these features give an indication of the complexity of radiative forcing (Sokolik et al., 2001).

A growing volume of studies is concerned with the development of models for the global and regional pathway undertaken by aerosol in the atmosphere, its load, and emission rate and depositional flux of dust (Lawrence and Neff, 2009). These are of interest in global climate models, specifically for evaluating the radiative forcing of aerosol (Slingo et al., 2006, Lefèvre et al., 2013, Albani et al., 2014, Matsui, 2017). Modelling the radiative balance is a far from trivial task. It must take into account the complex interplay between external forcing and internal feedback, and requires the morphological and optical properties of aerosol particles as an input: the amplitude of the forcing is related to aerosol size, mass extinction efficiency, shape and mineralogy of dust grains, in addition to the altitude of the dust layer (Dubovik et al., 2002). Having detailed and reliable information available about the optical properties of particles suspended in the atmosphere is therefore essential. To this purpose, it is necessary to deepen our current knowledge of the response of dust to electromagnetic fields — beyond the usual models and approximations — as well as to collect enough data from samples in the field to compensate for the great variability of scattering parameters.

Transport and subsequent dry and wet deposition in polar regions make long term storage of pristine aerosol particles possible far from sources of pollution and contamination (Alloway et al., 2007, Wolff et al., 2010). These sites are an invaluable source of data. Among other advantages, ice core drilling of polar ice caps allows

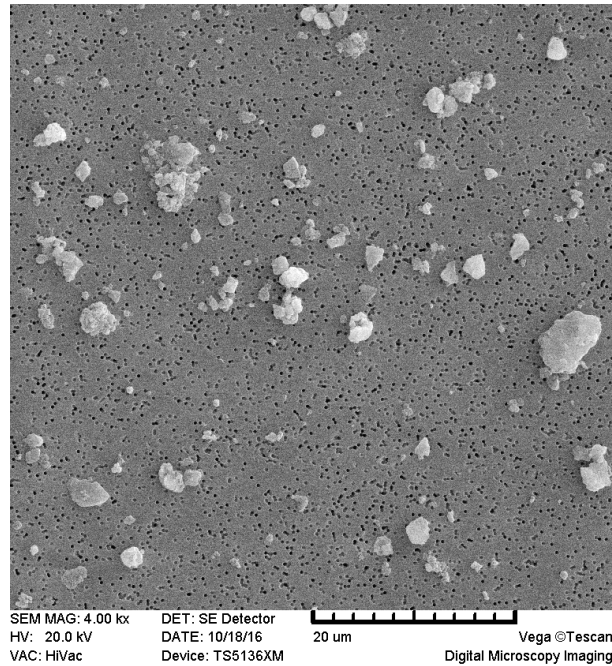


Figure 3.2: Scanning Electron Microscope image of mineral dust particles from Dome C, Antarctica (sample 5534). Shape and size variability is well visible, moreover, some particles result from in-situ aggregation of smaller grains (top-left area).

for accurate dating of samples and retrieval of high-resolution⁴ paleoclimate records over up to geologic time spans (Ruth et al., 2008, Rasmussen et al., 2014, Bertler et al., 2018, Maffezzoli et al., 2017, Potenza et al., 2017a). A Scanning Electron Microscope⁵ image of a set of mineral dust particles found in an Antarctic ice core are shown in figure 3.2.

Aerosol flux, concentration and composition can be related to abrupt climatic fluctuations and glacial–interglacial transitions (Delmonte et al., 2002, Albani et al., 2018, Lunga et al., 2017). For example, in central Greenlandic ice cores dust concentrations were found to vary up to two orders of magnitude between the Last Glacial Maximum and the Holocene (Ruth et al., 2003). The glacial–interglacial climate changes are correlated with sequences of high and low dust concentrations ranging from 800 to 15 $\mu\text{g kg}^{-1}$ over the past climate cycles. Furthermore, differ-

⁴Time resolution might be annual or even sub-annual, depending on the availability of accurate stratigraphic markers (Kjær et al., 2017). Generally, it gradually decreases with depth.

⁵The images were taken with the Scanning Electron Microscope in the EuroCold laboratory in the University of Milano-Bicocca during the first years of this PhD thesis. Liquid samples (melted ice cores) were filtered and covered with a Gold conductive layer.

ences in particle size distributions have been observed in different sites over the same climatic period (Delmonte et al., 2004).

In addition to insoluble dust particles, water-soluble ions such as Na^+ and NH_4^+ , metals and other elements can be detected and analysed with a temporal reference (Marino et al., 2004, Vallelonga et al., 2004, Witherow et al., 2006). Unique evidence of the atmospheric composition of the past can be collected by separating air bubbles occluded in the ice (Kaufmann et al., 2008). For instance, the Greenland Ice Core Project (GRIP) and the European Project for Ice Coring in Antarctica (EPICA) have recovered a considerable amount of valuable information for the characterisation the atmosphere climatic changes in the past, and have contributed significantly to our understanding of the role of mineral dust in the climate system (see for example the works by Fischer et al. (2007), Ruth et al. (2008), Lambert et al. (2008), Masson-Delmotte et al. (2010), Wolff et al. (2010), Zennaro et al. (2014), Emanuelsson et al. (2015)). A mineralogy study on the samples from the GRIP project is given by Maggi (1997).

More recent projects such as the North Greenland Eemian Ice Drilling (NEEM) or the Roosevelt Island Climate Evolution (RICE) achieved insights in the Last Interglacial–Glacial cycle bolstered by optimised Continuous Flow Analysis (CFA) systems and recently developed high resolution analytical techniques (Bigler et al., 2011, Petit et al., 2013, Pyne et al., 2018).

3.2 Intricacies of dust optical properties

The relevance of the radiative properties of mineral dust is twofold. On one hand, they have emerged as an important agent in the Earth’s global energy balance. On the other hand, and from a more technical point of view, particle sizing is commonly attained by optical techniques which rely heavily on assumptions about the optical cross section and polarizability of the samples. These approaches have been associated with systematic errors and calibration issues, as evidenced in the works conducted by (Lambert et al., 2008, Potenza et al., 2015b, Simonsen et al., 2018), which go beyond the specific case of ice core characterisation.

Size distribution of airborne dust has been subject of extensive research, primarily based on Coulter Counter (CC) or Optical Particle Counter (OPC) measurements (Ruth et al., 2003, Ghan and Zaveri, 2007, Cuccia et al., 2010, Bigler et al., 2011, Petit et al., 2013). The former measures the volume of the particle immersed in an electrolyte from a variation of impedance. The latter kind of instruments determine an *optical* equivalent size based on a measurement of the light scattered over a given solid angle (Heim et al., 2008). Other optical instruments as the Klotz Abakus follow a similar approach by measuring extinction (see later section 3.3)

related to an equivalent diameter via a spherical approximation. This is at the core of the discrepancies between the size distributions retrieved by such different strategies, as it has recently been established by Simonsen et al. (2018).

Characterising the optical properties of mineral dust — and aerosol particles in general — can be challenging, since they are affected by morphology, impurities and coatings (Ellis et al., 2016). Moreover, shape has been shown to have a considerable impact on aerosol optical depth (Potenza et al., 2016a, Mariani et al., 2017).

In addition, the composition of aerosol may evolve rapidly over time, altered by chemical reactions during transport: dust can collect many smaller constituents and acquire correspondingly diverse scattering and absorption cross sections (Pöschl, 2005). Specifically, fluorescence has occasionally been observed in aerosol particles on which adhered airborne particulates such as polycyclic aromatics and fluorescent cells (Redmond et al., 2010). For instance, at high altitudes relative humidity can exceed 100% (Fletcher et al., 2011) and in capturing water molecules hygroscopic aerosol particles change both in their size and effective polarizability. Usually, particles are then described in terms of a wet radius, while the effective medium approximations are the main tool for estimating the wet refractive index (Ghan and Zaveri, 2007, Balkanski et al., 2007).

Dust absorption is mainly governed by the amount of iron oxide (Dubovik et al., 2002), and the imaginary part of its refractive index can, on average, be set around 0.003 – 0.004 as compared to previous estimates twice as large (Redmond et al., 2010). On the other hand, comprehensive studies of mineralogy as the one from Gaudichet et al. (1986), and a broader perspective adopted by Claquin et al. (1999), estimate a value of the real part roughly $\sim 1.5 - 1.55$.

A major concern has been the differential scattering cross section of mineral dust, which is found to vary substantially from those of equivalent spheres based on Lorenz–Mie theory suited for homogeneous or spherical core-shell particles, as extensively reported in Nousiainen (2009). By definition, such approach fails to account for the particle shape, which has been acknowledged as a determining factor for the response to electromagnetic waves in the visible and near-infrared spectrum especially for micron sized particles (Kahnert et al., 2007).

As an example, in figure 3.3 we compare the scattering from a spherical particle to a population of cubes and oblate ellipsoids (flat, aspect ratio = 0.25) of equivalent volume ($2.15 \mu\text{m}^3$) and same refractive index ($n = 1.52$). Data from cubes and ellipsoids are averaged over a population of 100 randomly oriented particles, respectively. Such particles clearly exhibit a variability of the modulus of the scattering amplitude upon orientation, indicated in the plots with the coloured areas (standard deviation). While the scattering lobe has approximately the same aperture

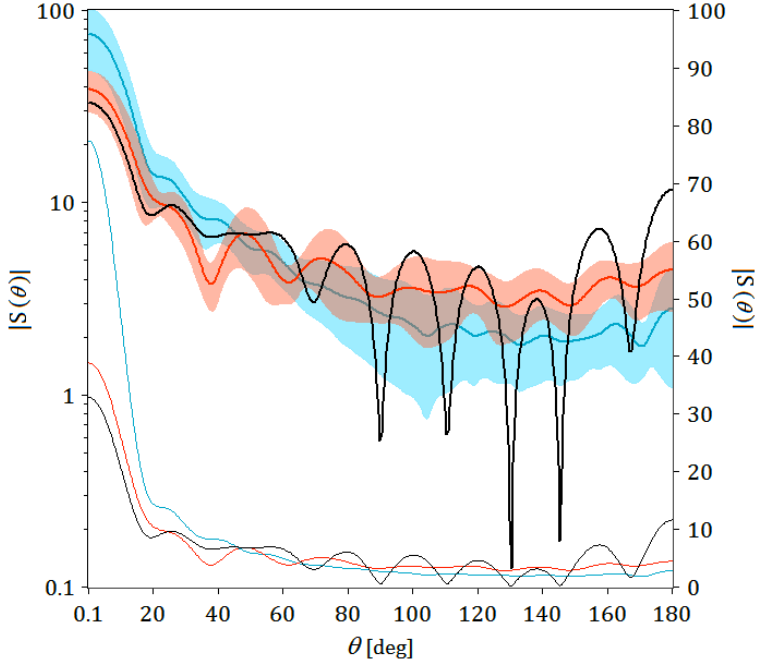


Figure 3.3: Log-lin plot of the modulus of the scattering amplitude for particles with different shapes and same volume and refractive index ($r_{eq} = 0.8 \mu\text{m}$, $\lambda = 0.63$, $n = 1.52$): sphere (black), oblate ellipsoids (blue, aspect ratio = 0.25) and cubes (red). For non-spherical particles, $S(0)$ is averaged over a population of 100 randomly oriented particles. Coloured areas correspond to the standard deviation. The curves of the sphere and the cubes, given their compact shape, have a more similar behaviour at small angles and differentiate at higher angles, as expected by basic diffraction theory. For reference, the three lower graphs are reported in lin-lin scale with corresponding colours. Notice the considerable difference in the forward scattering, and the variability upon the scattering angle.

for all three geometries, the value of $S|(\theta)|$ in the forward direction is appreciably different.

Notwithstanding its widespread use, the applicability of the Lorenz–Mie model for homogeneous spheres has been recently called into question, due to its poor agreement with experimental data in some specific cases (Pollack and Cuzzi, 1980, Mishchenko et al., 1995, Nousiainen et al., 2011). In the study by Munoz et al. (2001), the angular dependence of the scattering matrix of randomly oriented mineral particles is presented for fly ash aggregates and compact clay particles, with

particular focus on the influence of the shape of the particles. A clear distinction between the average aerosol scattering matrix of aggregates and clay was assessed, especially at high scattering angles. One of the challenges faced by researchers is the modelling of shape of non-spherical particles (Dubovik et al., 2006, Moosmüller et al., 2009). Global model calculations of radiative transfer usually do not account for complex particle shapes, but rely on Mie theory instead (Bond et al., 2013). Early attempts to model irregular large particles relied on geometrical optics models, but accuracy was limited by the critical dependence of reflectance upon surface roughness. From an angular distribution point of view, the impact of surface roughness is to smooth the scattering matrix trend as a function of the scattering angle and decrease the linear polarization maximum at $\theta = 90$ and strengthen depolarization (Nousiainen et al., 2003). A major advance is considered to be the use of ellipsoids to come closer to the shape of non-spherical particles and their differential scattering cross section. As mentioned in Section 3.6, the spheroid model allows a much more accurate modelling of phase function and polarization of scattered light from dust than that achievable through a model based on Mie spheres (Redmond et al., 2010).

According to the definitions in section 2.1, at low angles (low q) the scattered intensity bears information about the large scale morphology of the particle. At $\theta = 0$ one should have therefore the lowest sensitivity to orientation and the shape of the particle. Nevertheless, detecting the real and imaginary part of the field allows inspecting the particle morphology to some extent.

Overall, the studies mentioned so far suggest that a direct measure on single particles is often more informative than attempting to infer their properties with a model. We proceed to present some experimental results in the following sections.

3.3 Effects of shape

We now turn to the first part of the experimental results of this work⁶.

The experimental question we attempted to investigate is how does the shape of particles intercepting a laser beam affect their extinction cross section and optical thickness, as defined in section 2.4.

From a model perspective, giving up the isometric approximation for any particle introduces at least one new free parameter characterising its shape and, in addition, orientation. We should, in fact, consider that the incoming radiation sets at least one preferential direction parallel to its wave vector.

⁶A substantial portion of the contents of this section follows from the work undertaken with Dr. Marius F. Simonsen, to whom I would like to extend my acknowledgements both on a professional and a personal level. A thorough study on Greenlandic ice core samples can be found in Simonsen (2018) and Simonsen et al. (2018).

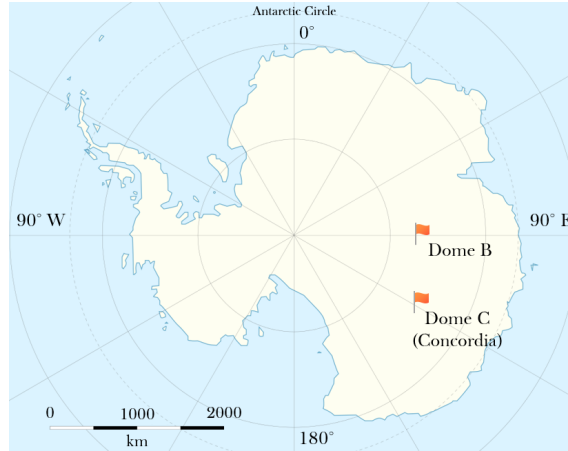


Figure 3.4: Map of Antarctica marked with the locations of Dome B and Dome C sites, from which the samples discussed in sections 3.3 and 3.4 were drilled.

As regards the shape, the parameter we are interested in is the aspect ratio ($a.r.$), loosely defined as the ratio between the major dimension of a particle and the width perpendicular to it or, more broadly, between its width and its height, whenever these are clearly distinguishable. The aspect ratio has values ranging from 1 for isometric particles, including spheres and cubes, to ideally 0 for an infinitely thin needle or sheet. In practice, it is common to encounter particles with $a.r. \sim 0.3 - 0.4$. This parameter cannot give a complete picture of the particle morphology, but it still has a measurable effect on the spread of the optical thickness distribution. Typical mineral particles found in ice cores are shown in figure 3.5: oblate (flat) particles on the left panel, and a prolate particle on the right panel. Following the procedure from Villa et al. (2016), we estimate the average aspect ratio of the particles by means of a look up table generated with the discrete dipole approximation code ADDA (appendix C).

We based our analysis on the Single Particle Extinction and Scattering (SPES) optical method, which is non-invasive and gives access to two independent scattering parameters. Furthermore, it allows for single particle measurements. This feature is critical, owing to the extremely low concentration of mineral dust in ice cores: most of the time, only one particle is present in the scattering volume of the instrument, i.e. the sensitive portion of the cell through which the sample flows. The SPES method has been extensively detailed and validated in a number of publications, as in Potenza et al. (2015a,b,c), Villa et al. (2016), Potenza et al. (2016a) and Mariani et al. (2017). A summary of the main features of the method can be found in appendix A.

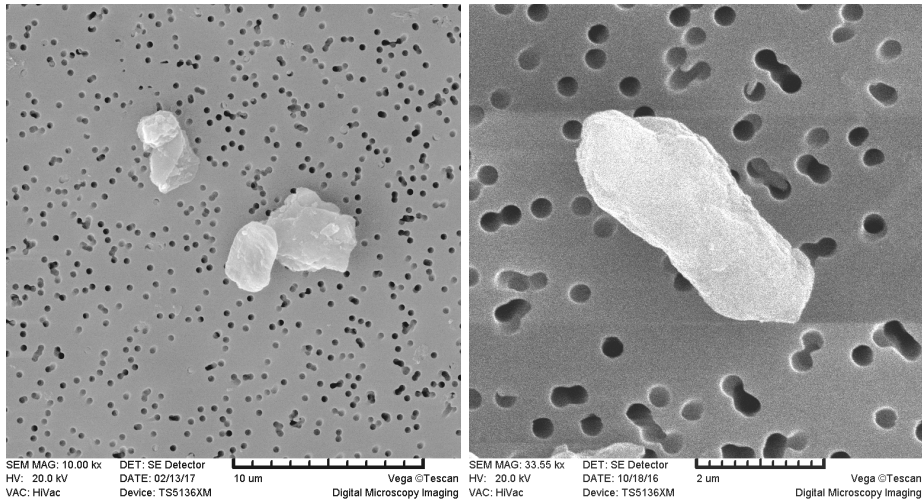


Figure 3.5: Scanning Electron Microscope image of oblate (left) and prolate (right) mineral dust particles in sample 5316, from Antarctica (EPICA) Dome C ice core, ca. 2900 m depth.

We operated a SPES unit in a cleanroom to avoid contamination of the samples. These were circulated through the instrument many times, up to some hundreds. The goal was to gather enough statistics to minimise the count-error, which depends on both the chosen binning and on the sample yielding a broader or narrower distribution. Usually this does not, however, take more than $\sim 10 - 20$ minutes. The measurement efficiency can be enhanced by a factor of 10 by adopting a different cell and tuning the laser focusing.

The typical output of SPES is shown in figure 3.6. Data are shown on the complex plane representing the forward scattering amplitude, $S(0)$, as a two-dimensional histogram in a log-log scale. The colour gradient indicates the number of counts within each two-dimensional bin, normalised to the maximum value (green). The figure shows the distribution of a size polydisperse population of micrometric kerosene droplets, yielding an extended distribution of scattering amplitude moduli, with a narrow distribution in the vertical direction ($\Im m S(0)$), the particles being spherical. The results from measurements using calibrated spheres are shown in figure A.2 in the appendix, where the discrete values of the diameters yield narrow peaks well separated on the $S(0)$ plane. However, the size polydispersity exhibited by the sample 3.6, as well as all the other samples we analysed, does not preclude assessing the refractive index, but is rather a feature that can be exploited for statistical analysis. We compare experimental data with Mie calculations, indicated with a black solid line in the figure, whereby we obtain $n = 1.46$ in very good agreement

to the expected value for kerosene (this pattern is further exemplified in figure A.3 in the appendix).

In principle, we may assign to (almost) any point in the $S(0)$ plane a homogeneous

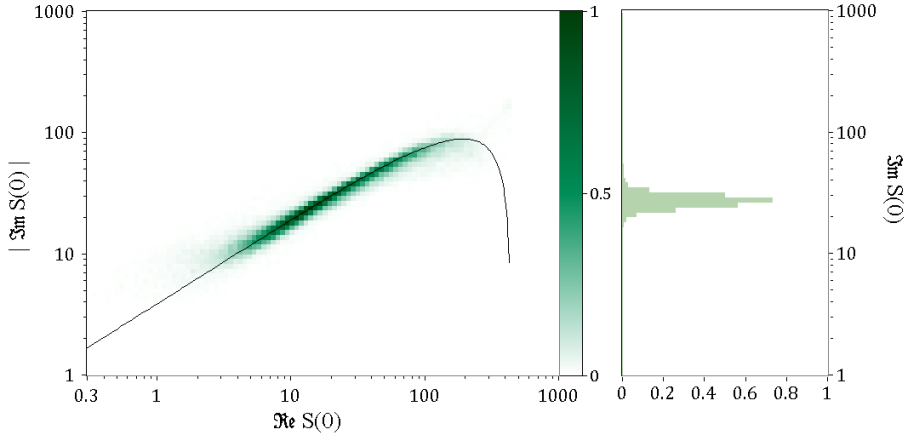


Figure 3.6: The complex $(\Re S(0), |\Im S(0)|)$ plane adopted for representing the SPES data (left). The two-dimensional histogram reports the experimental results relating to an emulsion of micrometric spherical droplets of kerosene in water, normalised on its maximum (dark green). Mie calculations for $n = 1.46$ are reported with a black solid line. Polydispersity results in a wide range of scattering amplitude moduli. By contrast, the distribution is narrow in the vertical direction, as evidenced by the histogram on the right panel reporting a section at $\Re S(0) = 20$.

sphere characterised by two parameters, namely, its radius and refractive index. We would then achieve a *Mie inversion* of our scattering data. However, this one-to-one correspondence is strictly limited to spheres or, at most, to compact, isometric particles. In some circumstances, for instance, a distribution like the one shown in figure 3.6 may be ascribable to particles other than spheres: under appropriate shear conditions, prolate particles can be forced to rotate on a plane orthogonal to the optical axis. As a result, the incoming laser beam crosses particles with the same geometrical thickness t regardless their orientation, thus the optical thickness, ρ , is consistently the same (equation (2.39)). Under these conditions, prolate particles yield a distribution on the complex plane which is identical to one arising from a distribution of spheres (see figure 3.7). In order for the two distributions to overlap on the $S(0)$ (or (C_{ext}, ρ)) plane, however, the refractive index of the spheres must be lower than that of the prolate particles. The exact value depends primarily on the aspect ratio of the prolate particles.

A recent work by Potenza et al. (2016a) provides an example of such phenomenon

by quartz micrometric particles. Experimentally, prolate particles and spheres can be distinguished by designing the setup in such a way that shear is removed or reduced as necessary (see section 3.4). Hence, the asymmetric particles are free to orient randomly, and their distribution broadens significantly.

In figure 3.7 we show simulated data of prolate particles (ellipsoids, aspect ratio

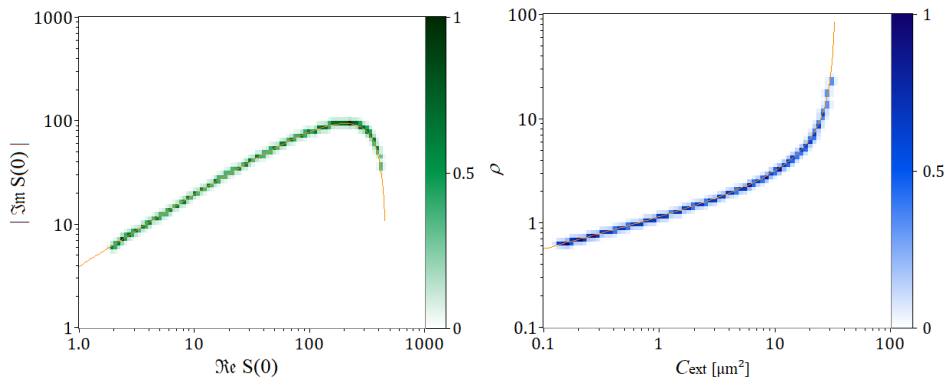


Figure 3.7: (left) Simulations for prolate ellipsoids with aspect ratio 0.33 (green histogram) compared with Mie calculations of a distribution of spheres 0.1–2.5 μm in diameter (orange solid line). While the refractive index of the ellipsoids is $n = 1.55$, the best match is found with spheres with $n = 1.46$. (left) Alternative plot on the (C_{ext}, ρ) plane.

0.33) oriented randomly with their major axis orthogonal to the optical axis. The volume of the particles ranges uniformly from $\sim 0.065 \mu\text{m}^3$ to $\sim 14 \mu\text{m}^3$. In the notation adopted by ADDA, $\text{Im}S(0)$ is negative and its sign is reversed in the plots. Comparing the distribution with the Mie model for spheres yields a refractive index which is much lower than the refractive index of the population: $n = 1.46$ (instead of $n = 1.55$). This is a good illustration of the effect of shape on the optical thickness (consequently, on the effective refractive index): this is generally reduced by any deviation from the sphere (Van de Hulst, 1981). Alternatively, this behaviour can be seen as an enhancement of the scattering efficiency of the population, which in turn can be traced back to basic diffraction theory. Particles exhibiting protuberances, surface roughness, edges, etc. have a tendency to scatter light at higher angles, therefore, the forward scattering is correspondingly decreased relative to compact, smooth particles with the same volume (mass). It should be noted, however, that this also depends on particle orientation. Experimental data of analogous cases can be found in Villa et al. (2016), where the authors investigated calibrated monophasic mineral samples and monodisperse calibrated dumbbells for the purpose.

At variance with samples that are mainly populated by prolate particles, shear does not effectively impose enough constraints on oblate particles to reduce thickness variability. Oblate particles under shear tend to rotate around the axis parallel to the flow, whereas their effective thickness crossed by the laser beam can still vary widely (Simonsen et al., 2018). We report in figure 3.8 data from a recent alpine sample (Rutor Glacier, 2500 m - Aosta Valley, Italy, 2016) which is in stark contrast to the ideal case of spherical particles shown in figure 3.6. It is representative of the majority of samples from this site.

SPES data is spread on a wide portion of the $S(0)$ plane, which is attributable to the shape of the particles. The refractive index of mineral dust, in fact, lies in a narrow range, so the variability due to this parameter is negligible⁷. This particular case shown here exhibits some other interesting features, such as a distinct ridge at about the centre of the distribution. This is reflected by the panel on the right. Interestingly, the equivalent refractive index (corresponding to a distribution of spheres) of such distribution is just below $n = 1.41$, too low to be compatible with the mineralogy of particles in ice cores (Delmonte et al., 2017). Thus, this counts are most probably due to a population of prolate particles. We can, for instance, easily confirm this hypothesis with electron microscopy or holography in conjunction with SPES measurements.

Moreover, some variability in the two-dimensional histogram can be ascribed to mineralogy or to a fraction of absorbing particles, which might be responsible for the lower portion of the plot (low \Im and high $\Re S(0)$, i.e. low forward scattering and high extinction). Work is currently in progress to characterise such features. The panel on the right reports a section of the distribution at $\Re S(0) = 20$ and provides a closer look to its width. Moreover, comparing the width of the distribution to simulations we can estimate the average aspect ratio of the particles in the samples, which ranges between 0.15 and 0.25.

As an example, in figure 3.9 we report a polydisperse distribution of cuboid platelets (oblate square prisms) with aspect ratio 0.3. As it is clear from the left panel of figure 3.9, the pattern on the plane is widely extended along both the ρ and C_{ext} axes.

The volume of the particles ranges between $0.005 \mu\text{m}^3$ and $24 \mu\text{m}^3$, which gives a distribution of equivalent diameters between $\sim 0.1 \mu\text{m}$ and $\sim 1.8 \mu\text{m}$. For later convenience, in the vertical axis we report the optical thickness, $\rho = 2\Re S(0)/\Im S(0)$, as defined in equation (2.39). On the horizontal axis is reported the extinction cross section, C_{ext} , which by the optical theorem (1.2) is proportional to $\Re S(0)$. This physical quantity is a monotonic, non-decreasing function of volume, but its trend

⁷The refractive index of mineral samples can be obtained by a match to calibrated liquids with an optical microscope.

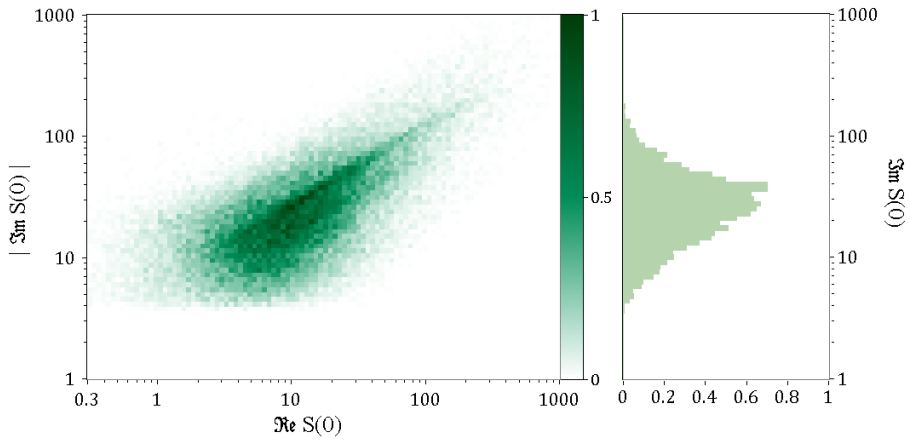


Figure 3.8: SPES data reported in a two-dimensional histogram as in figure 3.6, relating to a recent alpine sample Rutor Glacier, 2500 m - Aosta Valley, Italy, 2016. Notice the ridge at approximately the centre of the distribution, which also appears in the histogram on the right. The equivalent refractive index of this population is 1.41.

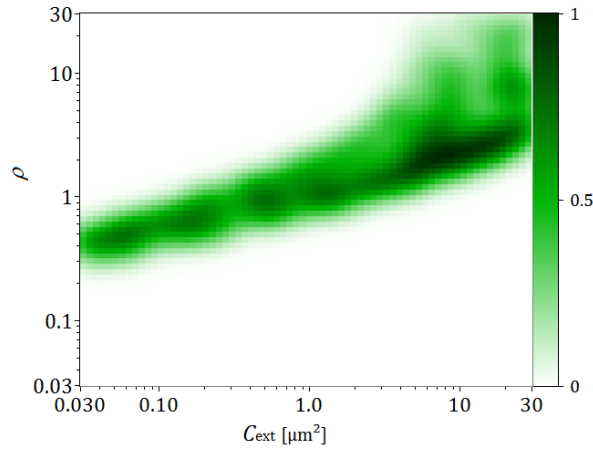


Figure 3.9: Distribution of a simulated population of square platelets, 0.3 in aspect ratio, with their side ranging between $0.26\text{ }\mu\text{m}$ and $4.3\text{ }\mu\text{m}$, and volume ranging between $0.005\text{ }\mu\text{m}^3$ and $24\text{ }\mu\text{m}^3$.

is not linear and depends on many other parameters, among which the refractive index. As a result, it only gives a rough estimate of particle size. Particles with a larger refractive index fall higher on the (C_{ext}, ρ) plane (see section 2.4).

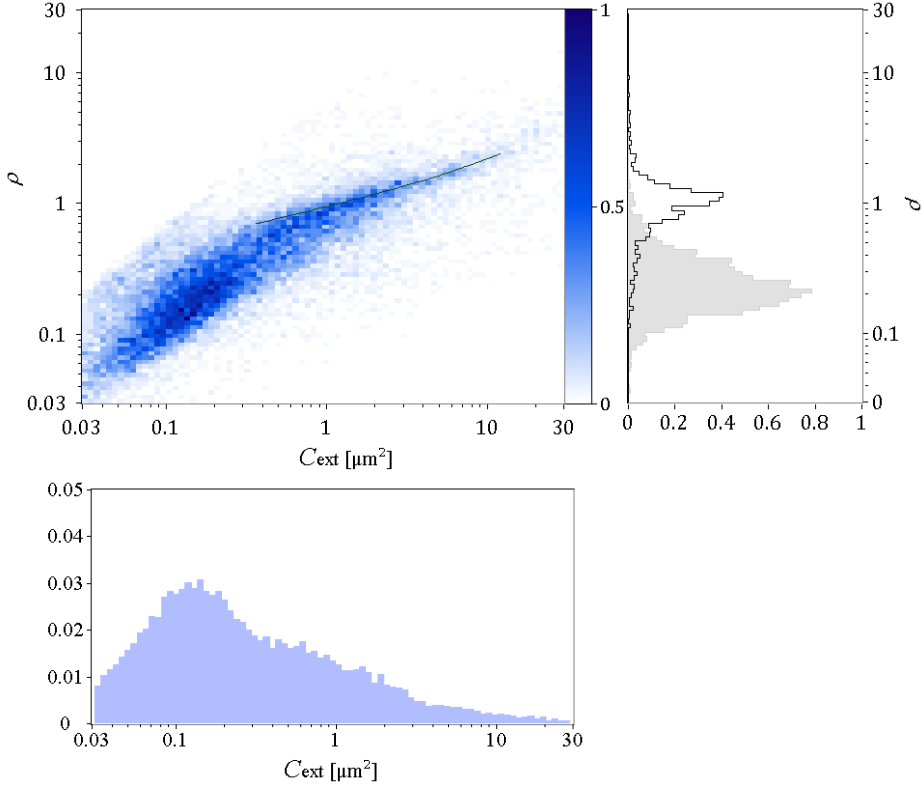


Figure 3.10: (top left) SPES data from sample DB560.40 (19 ky BP), Dome B, Antarctica. Notice that the distribution can be ideally divided into two subsets. The black solid line refers to ellipsoids with an aspect ratio of 0.5 and a refractive index $n = 1.46$. (top right) Vertical sections at $C_{\text{ext}} = 0.2$ (grey) and $C_{\text{ext}} = 2$ (black) offering a clearer view of the widths of the two populations on the left. (lower panel) Histogram of the extinction cross section.

In figure 3.10, we report the results relative to a sample from Dome B, Antarctica (77°05'S, 94°55'E, figure 3.4) dated to 19,000 years ago. A thorough analysis of samples from this site can be found in the work by Delmonte et al. (2017). Two separate populations are well visible on the (C_{ext}, ρ) plane: a broad distribution of smaller particles at roughly $C_{\text{ext}} \lesssim 0.5$ and a predominance of prolate particles for $C_{\text{ext}} \gtrsim 0.5$ that give rise to a thin distribution. The black curve in the graph is

obtained from ellipsoids with a ranging volume, aspect ratio = 0.5 and refractive index $n = 1.46$. Interestingly, this curve coincides with Mie theory calculations for spheres with a refractive index $n = 1.42$.

For comparison, integrating the two-dimensional histogram along the vertical axis yields the histogram in the lower panel of figure 3.10, as if only extinction was measured. The peculiar patterns arising on the complex plane are somewhat hidden. SPES data from a neighbouring section of sample DB560.40 are shown in figure 3.11. Dust content in the Dome B ice core we analysed exhibited a outstanding variability. Comparing the histograms in figures 3.10 and 3.11 illustrates this feature clearly. The ridge like distribution related to prolate particles (~ 0.5 aspect ratio) is still visible, albeit is not possible to distinguish prolate from oblate particles in this sample. We can evaluate the average aspect ratio of the particles from the variance of the optical thickness, ρ , by comparing experimental data to a distribution of simulated polydisperse oblate particles. Specifically, we are able to set an *optical* aspect ratio from the spread in the 2D histograms. The overall width of the distribution is compatible to oblate particles with *a.r.* ~ 0.5 setting the refractive index around $n = 1.5$.

In figures 3.12 and 3.13 we give some further examples of the distributions from Antarctic samples in Dome B. In particular, figures 3.12 (b) and 3.13 (b) show remarkably different distributions in spite of relating to neighbouring samples⁸

We will now move on to discuss more closely the instrumental issues arising from the effects of shape seen so far. As mentioned while introducing this chapter, the Coulter Counter (Coulter, 1953) is an effective tool for characterising the size distribution of the kind of particles we are interested in (Delmonte et al., 2005). This instrument provides a reliable estimate of the volume of the particle based on an electrical impedance signal. If the particle is not charged or polarized, this result is weakly affected by shape: a volume-equivalent diameter, d_{vol} , can be then associated to the particle, assuming it is spherical.

The main drawbacks of this method are the need to alter the sample (the melted ice core) in order to stabilise electrical conductivity of the fluid by the addition of salt (Simonsen et al., 2018), and the sensitivity of the instrument to electrical noise. Furthermore, it cannot be included as a module of continuous flow analysis lines, which imposes a limit on the duration and the resolution of the measurements (Delmonte et al., 2004).

Conversely, optical sizing techniques in the size range $\sim 0.5 - 20 \mu\text{m}$ are non-invasive and suitable for in-line analyses.. A notable example is the optical instrument men-

⁸The image in figure 3.13 (a) is a courtesy of Dr. Barbara Delmonte, Università degli Studi di Milano-Bicocca, private communication.

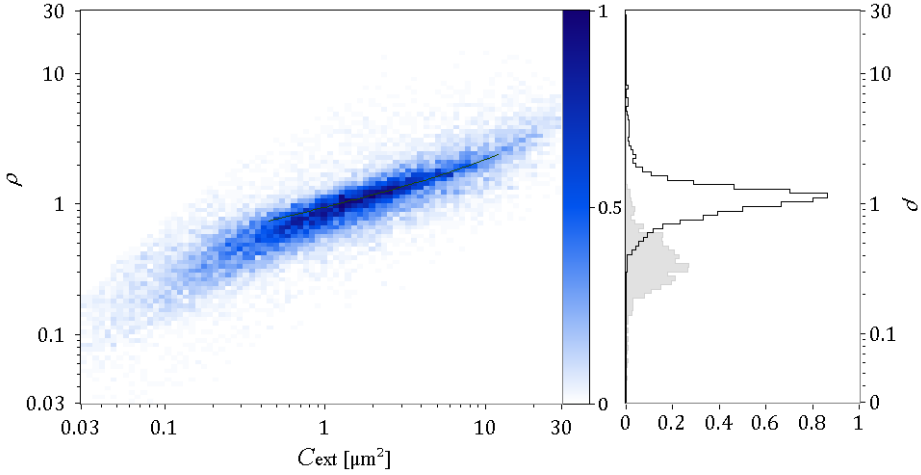


Figure 3.11: (left) SPES data from sample DB560.20 (Dome B, Antarctica), a neighbouring ice core section of the sample described in figure 3.10. The black solid line refers to quartz ellipsoids with an aspect ratio of 0.5. (right) Optical thickness distribution at $C_{\text{ext}} = 0.2 \mu\text{m}^2$ and $C_{\text{ext}} = 2 \mu\text{m}^2$ are reported in grey and black, respectively.

tioned by Simonsen et al. (2018), namely the Klotz Abakus, installed in the CFA system of the *Center for Ice and Climate* in Copenhagen and reaches a depth resolution of ~ 3 mm on melted ice-cores. The signal is affected by electrical noise to a lesser extent with respect to the Coulter Counter, provided the laser is stable. In this kind of instruments, a sensor is placed either at an angle around $\theta = 90^\circ$ with respect to a laser beam, and the recorded intensity is related to an extinction-equivalent diameter, d_{ext} , inverted by the Mie model. This is defined as the diameter of a sphere of a given material - commonly polystyrene - that would produce the same signal as the measured one. In some cases, it may include an optical system for measuring attenuation or for integrating the scattered intensity over a given solid angle closer to $\theta = 0$.

As an instrument performing straightforward light intensity measurements, it is not designed to set stringent constraints on the numerous scattering parameters. Thus, the procedure to invert data overlooks composition, shape, and orientation of the actual particle crossing the laser beam. These affect both the total optical extinction and the scattering angular distribution.

Since the Coulter Counter and the Abakus are designed to measure different characteristics of the particles, they need different models whereby to infer an equivalent

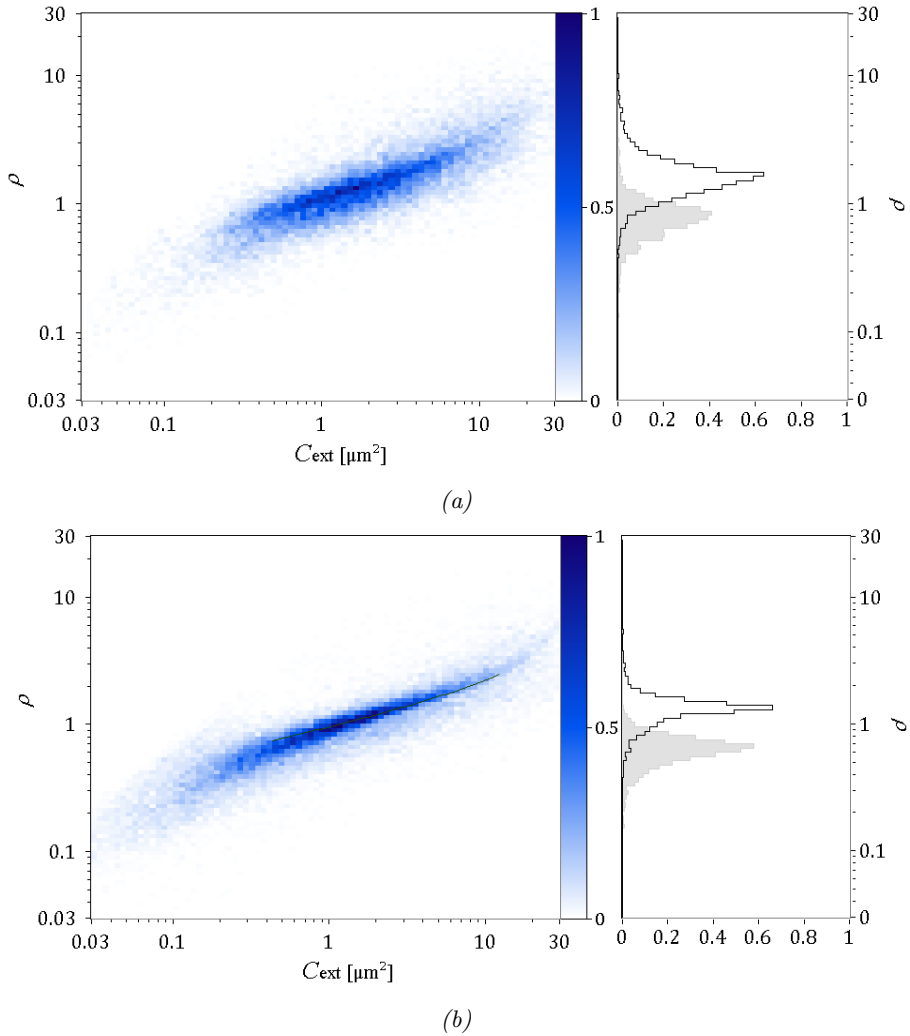


Figure 3.12: Samples DB600-20 (a) and DB640-35 (b) from Dome B, Antarctica. The black line corresponds to quartz oblate ellipsoids with an aspect ratio of 0.5. While being both dominated by prolate particles, the samples exhibit a different width in the optical thickness distribution. Optical thickness histograms on the right are sections of the SPES data set at $C_{\text{ext}} = 0.5 \mu\text{m}^2$ (grey) and $C_{\text{ext}} = 3 \mu\text{m}^2$ (black).

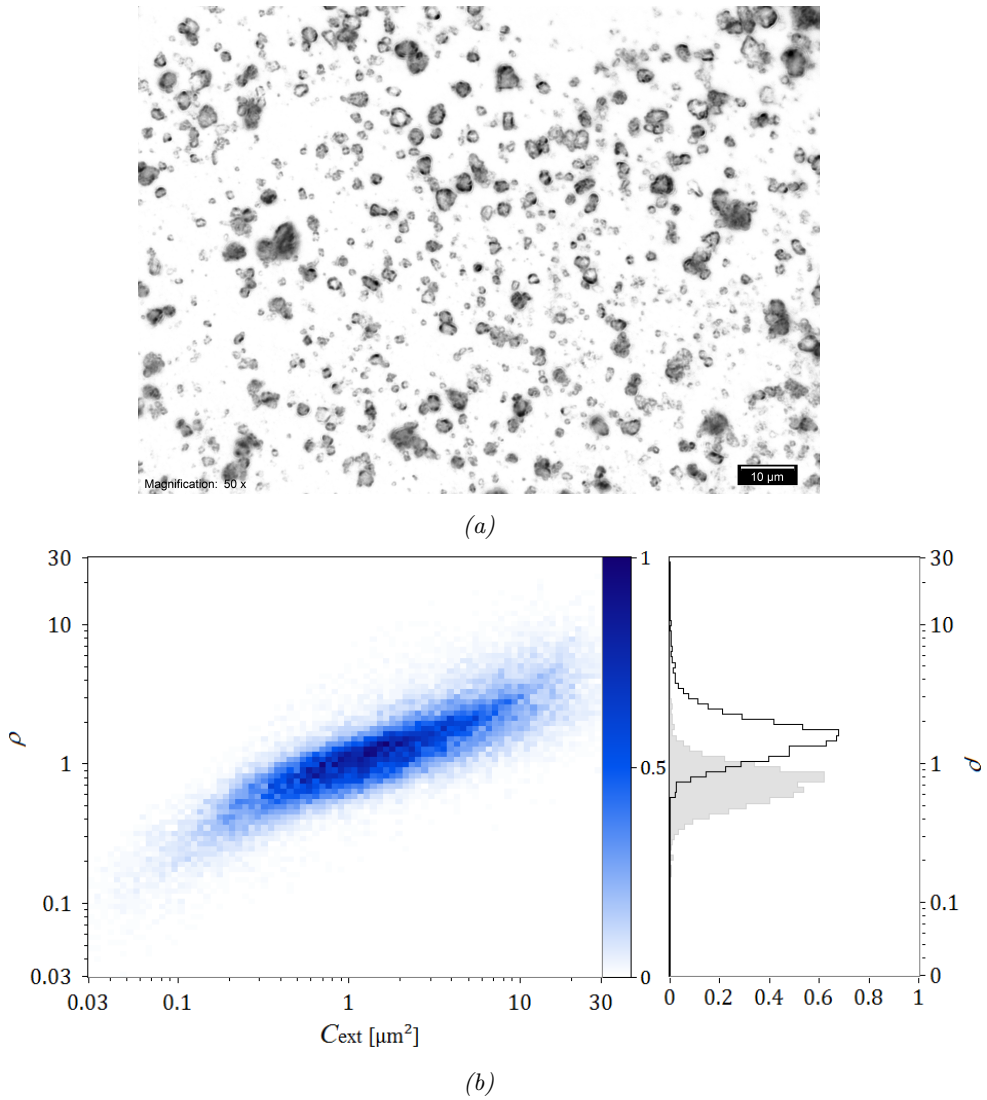


Figure 3.13: (a) Negative image of the particles in Sample DB640-75 from Dome B, Antarctica, taken at the optical microscope (Olympus BX51-M). The colours have been inverted for graphical purposes. (b) SPES data from the same sample represented as a two-dimensional histogram. Notice the remarkable difference of the distribution with respect to a neighbouring sample in figure 3.12. The histograms on the left correspond to sections at $C_{\text{ext}} = 0.2$ and $C_{\text{ext}} = 2$, respectively.

diameter. We observed that the volume equivalent diameter is usually smaller than the extinction diameter. This issue has been addressed in Simonsen et al. (2018), which also gives a protocol for calibrating the two instruments. Here we briefly report some of the measurements carried out in the clean room of the EuroCold laboratory in Milan.

We analysed Greenlandic samples drilled from the Renland Ice Cap Project (RECAP) and date back to both the last glacial maximum and the Holocene, up to 356 years before year 2000 (b2k) for the sample closest to the surface. SPES data from one of the most recent samples are reported in figure 3.14.

An overview of the samples and their depths can be found in the supplement of

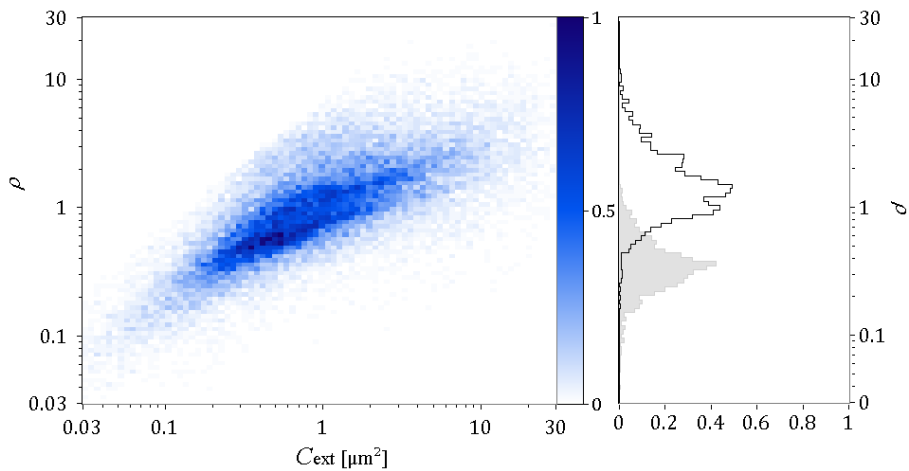


Figure 3.14: Greenlandic sample from Renland (RL304, depth ~ 167 m, 364 yrb2k, Holocene). SPES data is reported on a two-dimensional histogram (left panel), ρ distributions at $C_{\text{ext}} = 0.2$ (grey) and $C_{\text{ext}} = 2$ (black) are reported on the right panel. Notice two narrow ridge-like patterns from prolate particles (sphere-equivalent refractive index: $n = 1.39$ and $n = 1.47$ respectively) overlaid to a broad distribution due to oblate particles.

Simonsen et al. (2018). Each sample consists of a 55 cm long section of the ice core, a portion of which was measured with SPES. This method does not allow for an absolute measurement of particle concentration in the samples, since the area illuminated by the focused beam is smaller than the width of the cell, and each sample needs to be driven many times through the beam. Nonetheless, the particle counts give a relative estimate of concentration. Glacial samples systematically yielded considerably higher concentrations, up to one order of magnitude approximately, as well as a much more extended distribution on the (C_{ext}, ρ) plane (as shown in

figures 3.15, 3.16 and 3.17).

Overall, a significant prevalence of oblate particles was found in almost all samples from both periods; an exception is shown in figure 3.15, panel (b). According to the (C_{ext}, ρ) distributions, we can the limit of prolate particles at around 15%.

As in many other samples from ice cores, the refractive index of the particles ranges in a narrow interval, between 1.52 and 1.55 approximately. With these values, the average aspect ratio could be estimated, yielding 0.39 ± 0.032 for Holocene and 0.33 ± 0.04 for glacial samples. This difference can be identified by comparing figures 3.15, 3.16 with figure 3.17 in terms of the average width of the optical thickness distribution.

3.4 Aggregates of mineral dust

In addition particle shape and composition, the optical properties of dust also depend on surface roughness (Nousiainen et al., 2011, Potenza et al., 2016a). The close-up in figure 3.18 offers a prime example of the features of mineral dust aggregates comprising a variety of voids and fragments with various scale lengths. In particular, such morphological characteristics are not limited to the surface but can also occur inside the particle; they are responsible for an increase in scattering efficiency, while the overall optical thickness is reduced compared to that of a compact particle with the same volume (Potenza et al., 2017a). Particles in deep ice cores have been observed to undergo in situ aggregation below a depth of about 3 km (De Angelis et al., 2013). This phenomenon in itself has yet to be fully understood, and it would be certainly worth exploring. For example, it is known to alter the pristine size distribution of dust in deep ice cores, hence the more ancient data on climate and atmospheric dust load (Lambert et al., 2008).

Scanning electron microscopy observations can reveal detailed information about the morphology of the particles populating the samples, including mineral aggregates. Preparing samples for such analysis requires to isolate the solid components from water by using specific filters, which are then covered with a thin conductive layer (gold) before being scanned. Time-wise, this approach is far from being suitable for a systematic study.

Coulter Counter and optical extinction measurements detect the presence of such aggregates from anomalies in the size distributions, specifically, an excess of counts corresponding to large equivalent diameters. Nonetheless, these methods are not able to separate the contribution of unaltered compact particles from aggregates of small sizes.

In the following pages, we outline an experimental protocol whereby we were able to detect aggregates in ice core mineral dust samples irrespective of their size. This

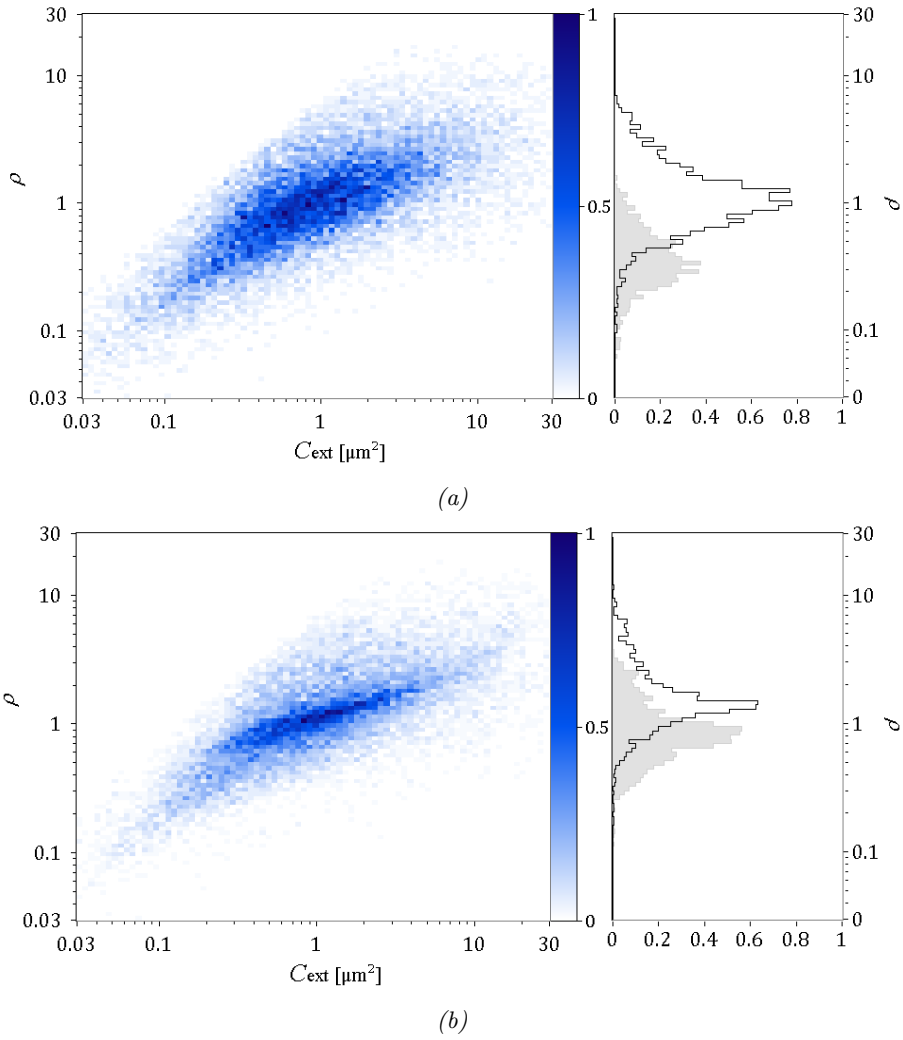


Figure 3.15: Holocene samples from Renland, eastern Greenland. (a) Sample RL788, depth 433.1 m, 2792 yr b2k. (b) Sample RL794, depth 436.4 m, 2878 yr b2k.

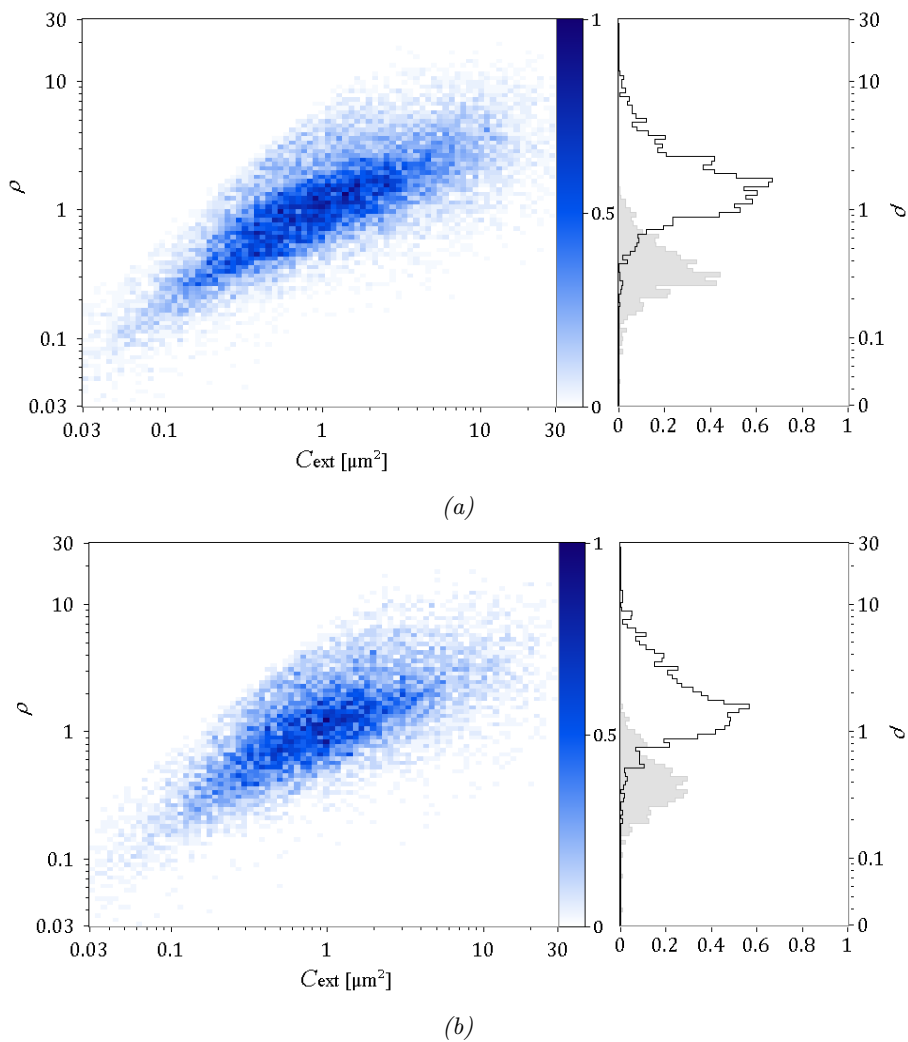


Figure 3.16: Holocene samples from Renland, eastern Greenland. (a) Sample RL837, depth 460.1 m, 3619 yr b2k. (b) RSample RL851, depth 467.8 m, 3926 yr b2k.

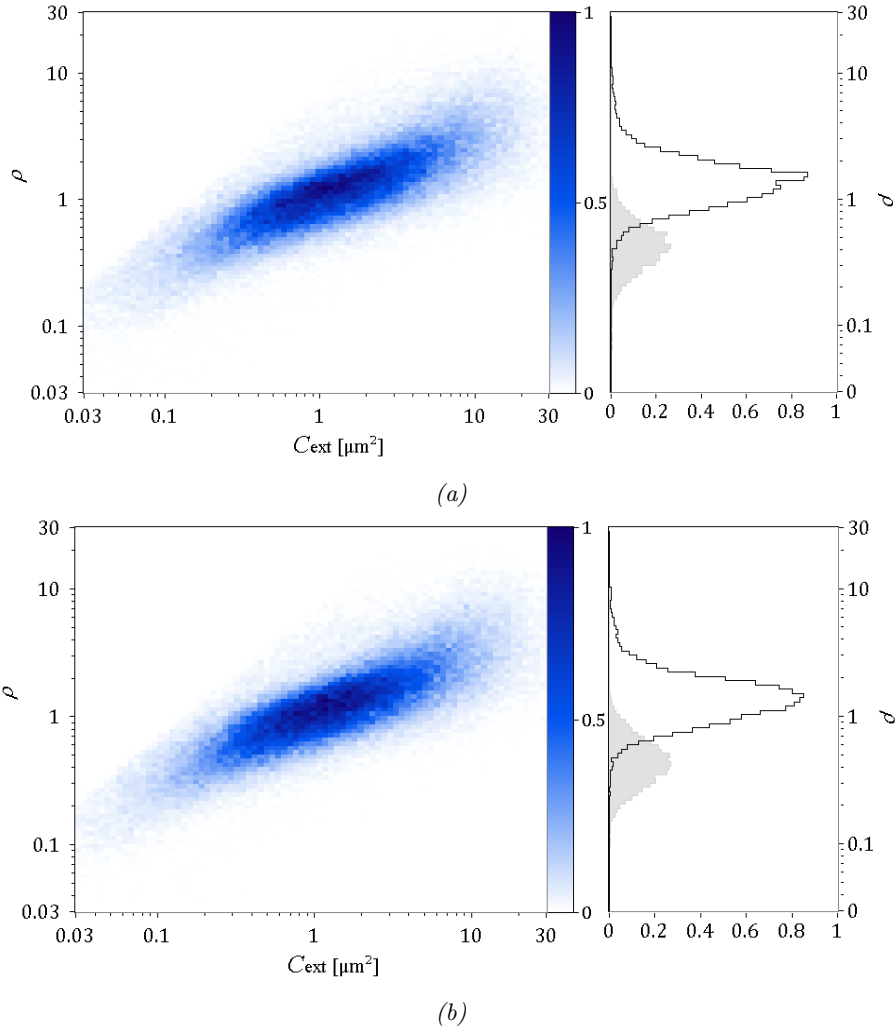


Figure 3.17: Glacial samples from Renland, eastern Greenland. (a) Sample RL973, 534.9 m, 22 958 yr b2k. (b) Sample RL974 535.4 m, 26 764 yr b2k.

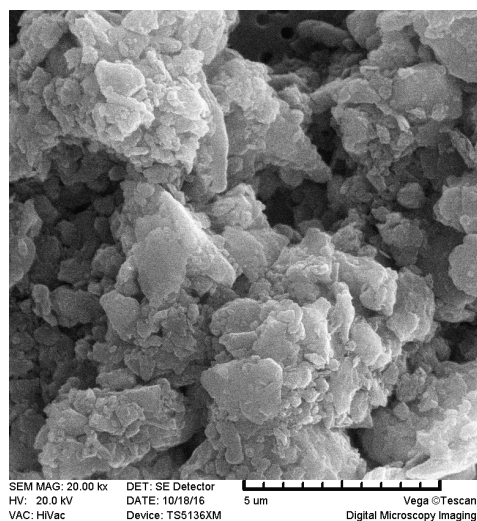


Figure 3.18: Close-up of the surface of a large mineral dust aggregate in sample EDC 5534 (see below).

represents another application of the SPES method, in connection with different shear conditions to give a preferred orientation to the particles driven through the system.

The outcome of this procedure on EPICA Dome C ($75^{\circ}06'S$ $123^{\circ}20'E$ in figure 3.4) led to a publication which we include at the end of the present chapter (Potenza et al., 2017a). We hereafter summarise the main points of this article. The reader might also refer to the supplementary material attached to the original manuscript for further details⁹.

We relied on a previous study on calibrated, non-spherical particles (standard monophasic quartz, kaolinite, and illite), which showed that shear can effectively impose constraints on the orientation particles of certain geometries (Villa et al., 2016). The key of the procedure is separating isometric particles from oblate/prolate particles.

By using two different flow-through cuvettes (Hellma 170.700-QS, 3.5×0.2 mm and Hellma 176.752-Qs 1.5×1.5 mm) at $10 \frac{\text{mL}}{\text{min}}$ and $1 \frac{\text{mL}}{\text{min}}$ flow rates, respectively, we can vary dramatically the shear stress to which particles are exposed. For the sake of comparison, we show the flow velocity profile in the two cells in figure 3.22.

In figure 3.21 we provide a close comparison of these two shear conditions on the same sample. Panels on the right correspond to the (C_{ext}, ρ) two-dimensional dis-

⁹<https://pubs.acs.org/doi/abs/10.1021/acsearthspacechem.7b00018>

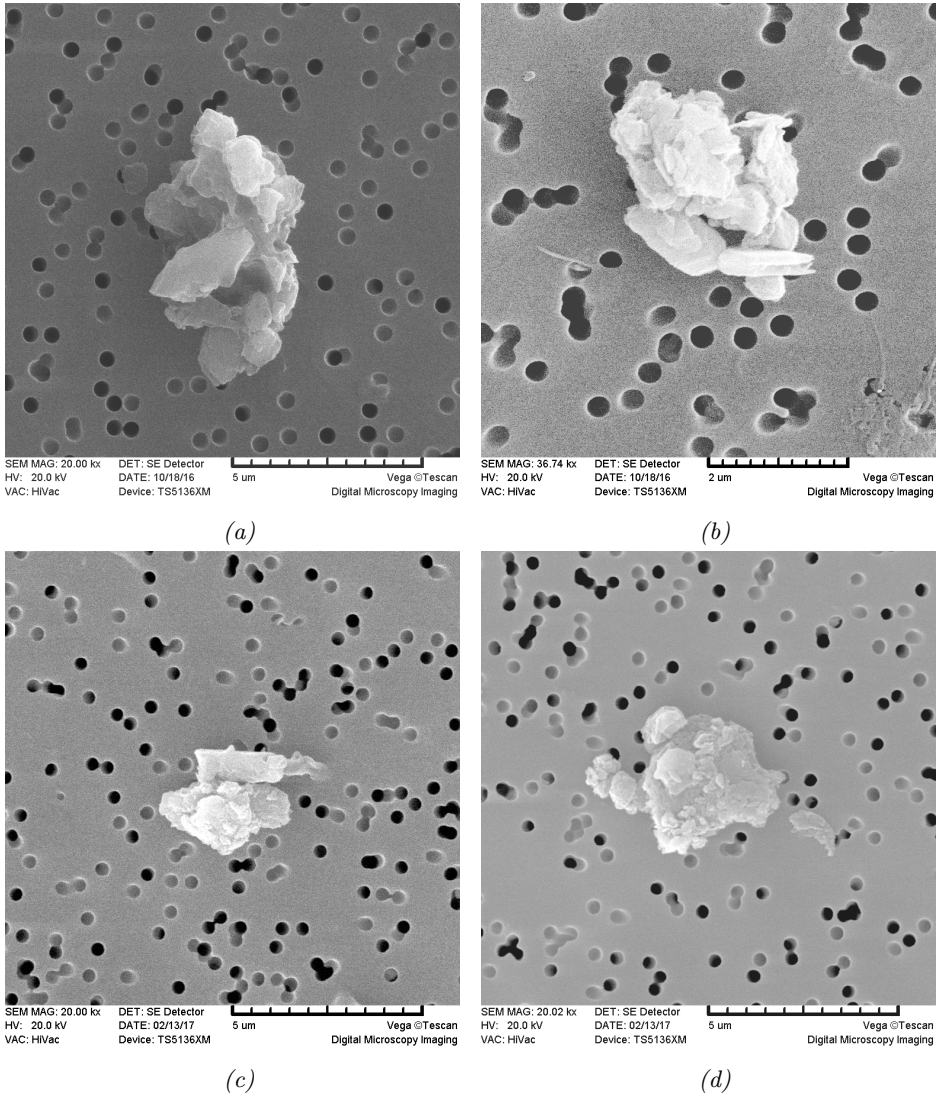


Figure 3.19: SEM images of mineral dust aggregates in deep ice cores from (EPICA) Dome C, Antarctica, ca. 2900 m depth. (a,b) sample EDC 5316, (c,d) sample EDC 5768.

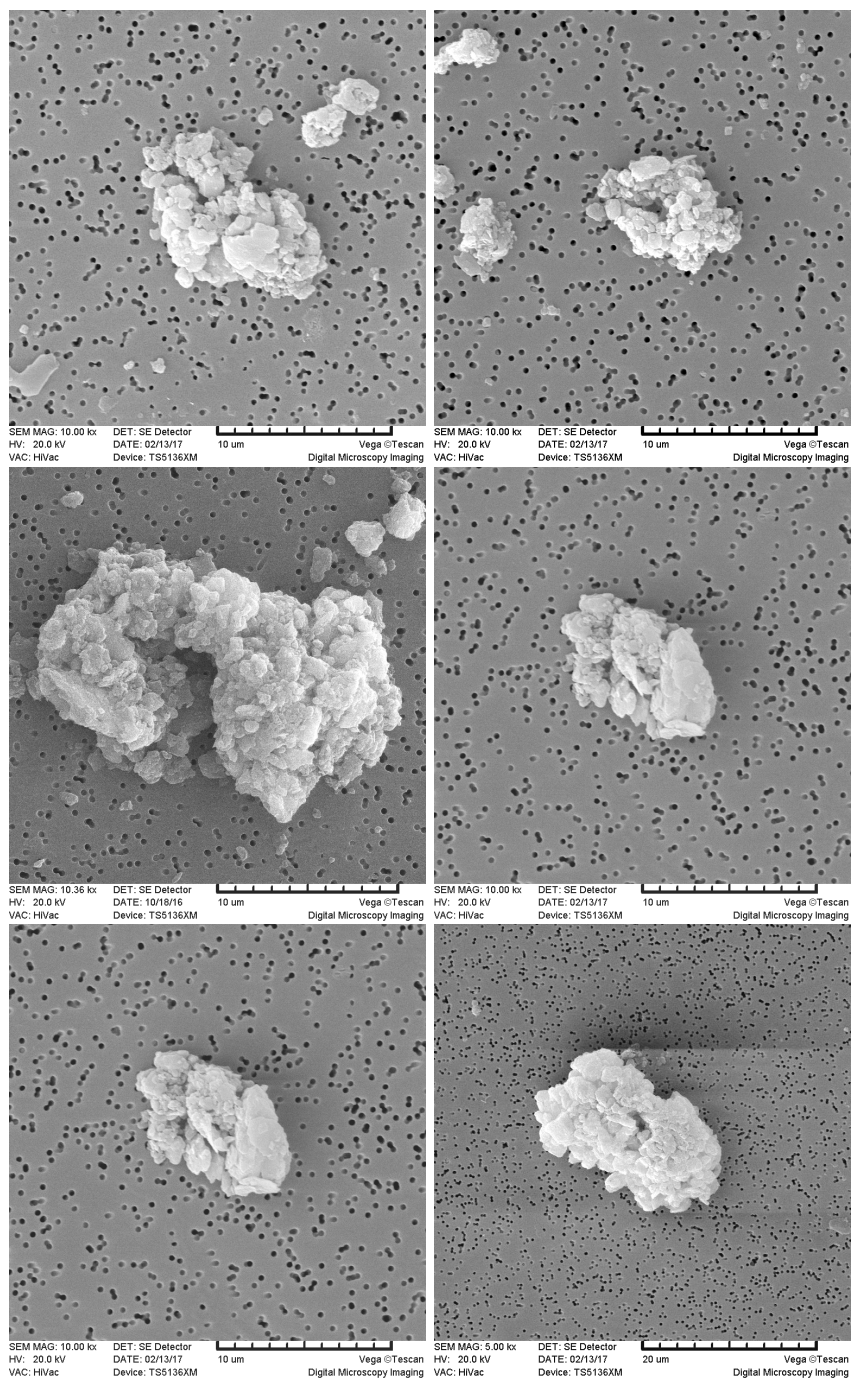


Figure 3.20: SEM images from sample EDC 5534, Dome C, Antarctica.

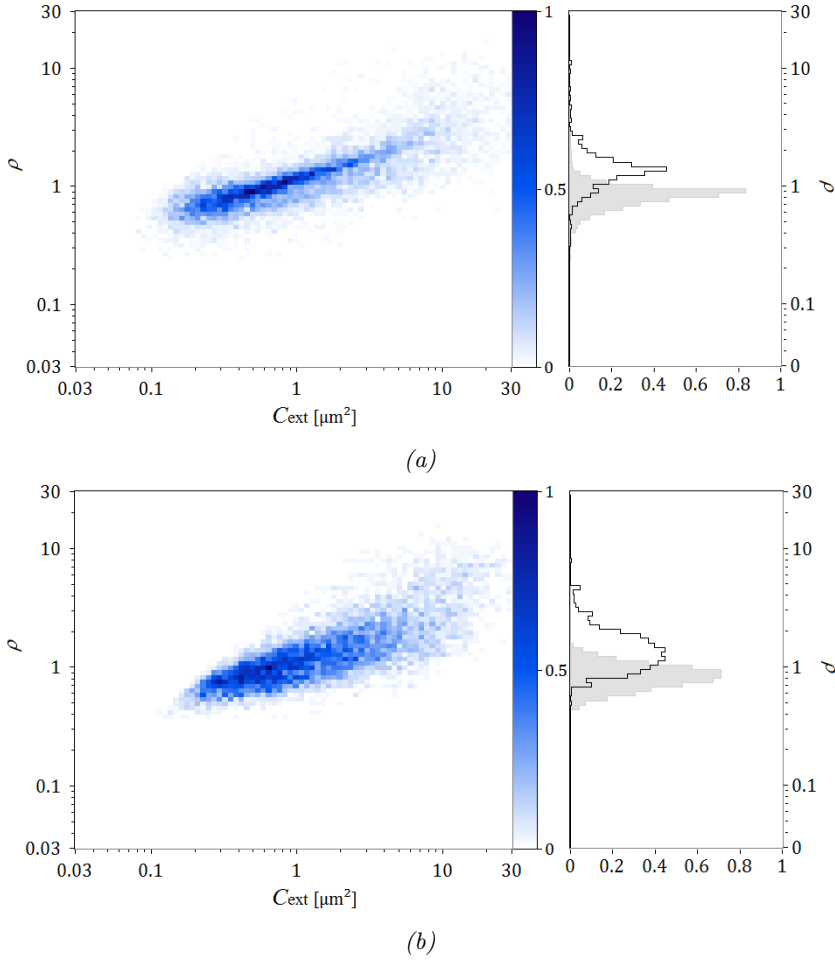


Figure 3.21: SPES data from sample EDC 5554, represented as a two-dimensional histogram normalised on its maximum (blue). On the vertical axis is reported the optical thickness, ρ , proportional to the ratio of $\Re S(0)$ to $\Im S(0)$, while on the horizontal axis is reported the extinction cross section, C_{ext} . The one dimensional histograms on the left correspond to vertical sections of the SPES data set at $C_{\text{ext}} = 0.5$ (grey) and $C_{\text{ext}} = 2$ (black). The top panel shows data obtained under high shear conditions; low shear conditions yielded the results shown in the lower panel. Notice the dramatic change in the width of the distribution, especially at larger values of the extinction cross section.

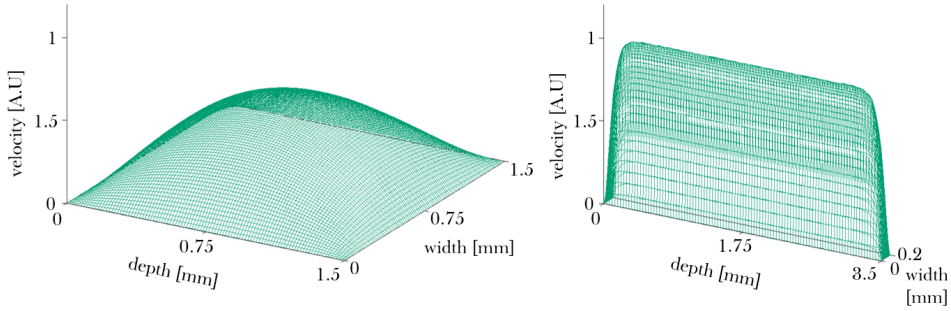


Figure 3.22: Velocity profile (arbitrary units) according to the Poiseuille approximation in the wide (left, 1.5×1.5 mm) and thin cells (right, 3.5×0.2 mm). Shear is proportional to the gradient of the surface.

tribution, while the histograms on the left are vertical sections at $C_{\text{ext}} = 0.5$ and $C_{\text{ext}} = 3$. The histogram obtained from the thin cell (top figure, high shear condition) exhibits a low dispersion vertical-wise. This indicates that the particles in the sample may be isometric, i.e. quasi-spherical albeit exhibiting surface roughness (see for example figures 3.19 and 3.20). Alternatively, a thin distribution is compatible with be prolate particles rotating on a plane orthogonal to the optical axis (Villa et al., 2016). The one-dimensional histograms are vertical sections of the SPES data set at $C_{\text{ext}} = 0.5$ (grey) and $C_{\text{ext}} = 3$ (black).

A test with the thick cell (low shear) relaxes the constraint on orientation. The sample yields a broad optical thickness distribution, as it can be clearly seen in the lower panel of figure 3.21. This leads to exclude that the particles in the sample are (mostly) isometric, and prevents us to attempt a sphere-wise inversion of optical data to assess the effective refractive index from a lookup table based on Lorenz-Mie theory.

As we have seen in detail in section 3.3, an asymmetric particle oriented randomly with respect to the laser beam yields a signal which is compatible with a wide range of refractive indexes and diameters. If, on the other hand, the distribution on the two-dimensional histogram does not change appreciably as a consequence of shear, we can safely assume that the morphology of the particles is not characterised by a substantial asymmetry, thus we can invert the scattering data and obtain the size distribution. This inversion leads to equivalent refractive indexes which are incompatible with the mineralogy of the samples, which is an indicator of the actual aggregate nature of the particles.

Some aggregate particles are shown in figures 3.19 and 3.20, displaying a Scanning Electron Microscope (SEM) overview of the samples we investigated. We

Table 3.1: Age and depth of the EPICA Dome C ice core samples chosen for analysis in Potenza et al. (2017a).

Sample	depth below surface [m]	climatic period	age [yr BP]	years per 7 cm	notes
5316	2923.4	14.2	548921	48	glacial
5534	3043.3	16.2	640193	160	glacial
5554	3054.3	16.4	661036	112	glacial
5768	3172.0	19.3	778334	78	interglacial

report some additional information about the samples in table 3.1. Among these, sample EDC 5534 exhibited a remarkable concentration of isometric mineral dust aggregates, as detailed in the following pages (Potenza et al., 2017a).

Single-Particle Extinction and Scattering Method Allows for Detection and Characterization of Aggregates of Aeolian Dust Grains in Ice Cores

M. A. C. Potenza,^{*,†,‡} L. Cremonesi,[†] B. Delmonte,[‡] T. Sanvito,[§] B. Paroli,[†] A. Pullia,^{‡,||} G. Baccolo,^{‡,||} and V. Maggi[‡]

[†]Department of Physics, University of Milan and National Institute for Nuclear Physics (INFN), Via Celoria 16, I20133 Milan, Italy

[‡]Department of Earth and Environmental Sciences, University Milano-Bicocca, Piazza della Scienza 1, I20126 Milan, Italy

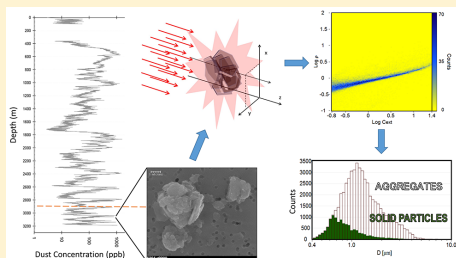
[§]EOS srl, Viale Ortles 22/4, I20139 Milano, Italy

^{||}Graduate School in Polar Sciences, University of Siena, Via Laterina 8, I53100 Siena, Italy

Supporting Information

ABSTRACT: Mineral dust aerosol in ice cores is one of the most important proxies for paleoclimate research. Under certain conditions, in the deeper part of ice cores, the pristine paleoclimate signal can be altered by *in situ* formation of dust aggregates, following the relocation of the impurities. Thus, aggregate detection is a critical indication for post-depositional processes. Clues for the presence of aggregates have been provided by anomalously large dust size distributions, while small aggregates were basically invisible to conventional dust analysis techniques. In this paper, we propose an optical approach to this problem based on the single-particle extinction and scattering (SPES) method, which allows researchers to distinguish between compact and non-compact particles through the analysis of samples populated by isometric particles contained in the core samples. This method can potentially be used during continuous flow analyses of ice cores. It allows for the detection of even the tiniest aggregates, falling within the typical size interval of aeolian mineral aerosol. This approach will potentially provide key evidence for assessing the integrity of paleoclimate records.

KEYWORDS: dust, optical properties, ice core analysis, aggregates, light scattering



INTRODUCTION

The undisturbed 800 000 year long record of aeolian dust provided by the European Project for Ice Coring in Antarctica (EPICA) Dome C ice core represents the longest ice core paleoclimate record of dust influx to Antarctica.¹ Dust flux is related to the primary supply of dust from the continents, which is, in turn, related to environmental conditions, long-range atmospheric transport, and the hydrological cycle.² Dust size, conversely, is an indicator of atmospheric transport and shows pronounced temporal and spatial variability at different time scales.³

An important piece of information about paleoclimate is buried within the bottom part of deep ice cores, where some of the data are consistent with a pristine paleoclimatic signal, while other data show anomalies. One example is represented by dust particles. In the deeper part of the EPICA ice core, where the temperature gradient increases and the ice temperature is close to the pressure melting point, relocation of impurities is known to occur, where ice grains slowly grow and recrystallize within the ice sheet. This process implies exclusion from the solid ice

grains and enrichment of particles in the melt (unfrozen liquid that separates grain boundaries). Such a post-depositional effect, responsible for the *in situ* formation of dust aggregates of different sizes, was first noticed in the deeper part of the EPICA Dome C ice core, through detection of anomalously large dust size distributions below ca. 2900 m depth.^{1,4,5} The presence of large dust aggregates was then confirmed by microscope observations. Sonication of samples allowed for partial dispersion of aggregates, but the size distribution record was not considered reliable for ice sections deeper than about 2850 m.

Because one of the main challenges in the future is to improve ice core records further back in time, it is essential to find a fast method, suitable for use in continuous flow analyses and capable of detecting the presence of dust aggregates in ice

Received: March 6, 2017

Revised: May 18, 2017

Accepted: June 9, 2017

Published: June 9, 2017

core samples, even within the typical size interval of aeolian dust particles, i.e., below about $5\ \mu\text{m}$ in diameter (equivalent spherical). Indeed, aggregates represent a critical indicator for post-depositional processes occurring in ice and potentially disturbing or altering the original climate signal.

In the case study considered in this paper, we focus on dust aggregates formed into the ice of some of the deepest EPICA Dome C ice core sections, where the occurrence of *in situ* aggregation is known.¹ Aggregate detection is essential to assess the occurrence of post-depositional processes and ultimately the integrity of paleoclimate sequences at depth.

From an optical point of view, aggregates are characterized by a non-uniform refractive index distribution, because the space is irregularly filled: the refractive index changes abruptly from that of the mineral part to that of the surrounding medium. In the case of aggregates composed by aeolian dust, these changes occur over length scales smaller than or comparable to the wavelength of light.

Usually, effective medium approximation is considered for describing aggregates, averaging some key properties of the inhomogeneous system. This approach provides the average polarizability of a given inhomogeneous particle by averaging the polarizabilities of the constituent materials, weighted by the corresponding volume fraction. In such a way, an equivalent refractive index of the whole system can be defined, reproducing the light scattering properties of a corresponding compact and uniform particle (Maxwell–Garnett model^{6,7}). Actually, obtaining the polarizability of a structured particle (and, therefore, the equivalent refractive index) is far from being obvious, and these approaches often prove to be inappropriate.⁷ Such limitation makes it almost impossible to discriminate aggregates from compact particles through optical single-particle methods (90° light scattering and extinction methods), and consequently, aggregates are usually recognized just from the presence of unexpected large sizes within the ice core sample.¹

Here, we approach the aggregate detection by the single-particle extinction and scattering (SPES) method, recently exploited for the characterization of the optical properties of aeolian dust in the old Dome C ice core. The SPES method^{8,9} is a novel optical non-invasive method, which can be operated in continuous flow analyses. It provides two independent optical properties for each particle, namely, the real and imaginary parts of the forward scattered field.¹⁰ These parameters are immediately related to the amount of power removed from the optical beam (extinction cross section) and the optical thickness of the particle (according to van de Hulst¹¹).

The SPES method allows for the exploitation of a novel approach recently proposed for the characterization of micro- and nano-sized particles.¹² It works on single particles, thus keeping the advantages achieved by other optical methods (90° light scattering and extinction methods). In addition, it is optically simple and self-calibrating and provides a powerful method for validating each signal, thus overcoming the main limitations of traditional optical methods. It has been proven to be very reliable in measuring highly polydisperse samples, with the advantage of giving an estimate of the equivalent refractive index of each measured particle.^{13,14}

The forward scattered light measured by the SPES method is mainly affected by size, composition (through the refractive index), and internal structure of dust grains. In this respect, for aeolian dust, the effect of the shape is by far larger than that of

the composition.⁹ In fact, changes in the mineralogical composition cannot give rise to appreciable differences of refractive index of single particles, while the shape can appreciably vary from isometric (cubic or rhomboedric crystals) to platelet- or needle-like objects.

Quite different is the case of dust aggregates found in the deeper part of the ice cores, made up by several closely packed individual grains sticking together to form an irregular complex structure, as evidenced in the pictures in the [Supporting Information](#). Although the single minerals composing the aggregate have a refractive index defined by their own crystallographic properties, the behavior of the forward scattered light, measured through the SPES method, is influenced by the aggregate structure.

An example of the optical response of non-compact structures has been shown by Villa et al.⁹ for a suspension of illite micrometer-sized aggregates. Here, we focus on the distinction between compact and non-compact structures to depict aggregates in ice core samples, which is a critical piece of evidence for assessing the integrity of the paleoclimate record.

MATERIALS AND METHODS

The SPES method is exploited to provide the optical thickness of each particle and recover an equivalent refractive index (see the [Supporting Information](#)), which can be easily associated with the aggregate/non-aggregate nature of single particles.

As introduced in previous works,^{9,13} here, we characterize the extinction cross section, C_{ext} , and the optical thickness, ρ , of each particle. The former is exactly the same quantity measured by the single-particle obscuration sensor (SPOS, as Abakus laser sensor), widely used to study dust in Antarctic ice cores.^{1,15,16} The fundamental point that we rely on to detect particle aggregates in liquid suspensions, such as the meltwater samples from ice cores, is that the optical thickness of an aggregate is lower than that of a single mineral grain of the same size. This is due to the non-uniform filling of the aggregate volume, in which irregular voids and cavities are left.

The reduction of the optical thickness of the aggregates is typically large enough to make the difference between compact and aggregate particles appreciable by the SPES method from a purely experimental point of view, i.e., in a model-independent way.

In the [Supporting Information](#), we describe the effect of the non-uniform internal structure of an aggregate on the optical thickness by introducing a simplified model based on the effective medium approximation,^{6,7,11} also known as the Rayleigh–Debye–Gans approximation.

In this paper, we limit the interpretation of SPES experimental data to the analysis of isometric particles to eliminate contributions from the shape/orientation and better distinguish aggregates from compact mineral particles.

Isometric particles, i.e., particles having the same size in the three dimensions, are characterized by negligible or small changes of the scattering field from their orientation, and this is a key point to recognize the isometric particles from experimental SPES data. By exploiting a twin measurement approach, i.e., operating the SPES method with two cells, one thin enough to orient particles ($0.2\ \text{mm}$)^{9,13} and the other thick enough to leave the particles to orient randomly ($1.5\ \text{mm}$), as shown by Villa et al., we are able to successfully identify and select the samples populated by isometric particles. In this way, we can safely adopt the approach described above.

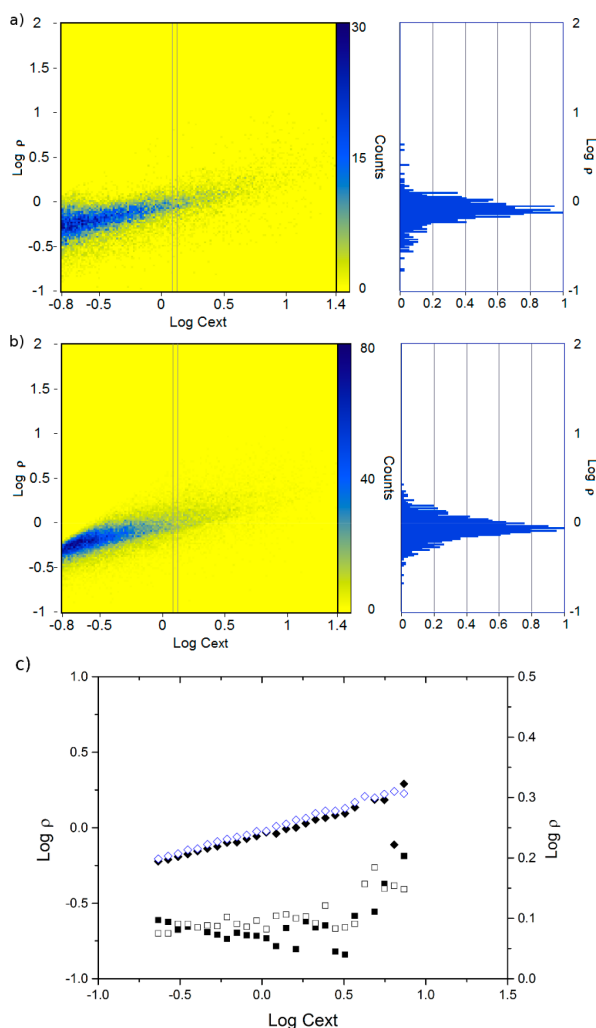


Figure 1. Sample EDC 5768: (left) SPES raw data as the (C_{ext}, ρ) histogram (yellow, zero; blue, maximum value) and (right) ρ distribution for C_{ext} within the two vertical lines, with (a) thin cell, (b) thick cell, and (c) mode (diamonds, left scale) and standard deviation (squares, right scale) of the ρ distribution overall, with the C_{ext} range for the thin cell (open symbols) and thick cell (solid symbols).

We note that this approach fully retains its physical meaning as long as the effective medium and Rayleigh–Gans–Debye approximations hold.^{6,7,9,11} This is not easily verified from experimental data and may be impossible in many cases. Nevertheless, the representation of the data described here is effective to show the differences between aggregates and compact particles, even up to the sizes where the description would in fact become more complex.

It is to be noted that the isometric compact mineral particles generally do not have perfect sphericity, instead often assuming

prismatic, rhombohedral, or cubic shapes or even more irregular forms, according to the crystal structures of the respective mineral species.

Although different orientations have limited effects for such particles, the shape has an important role.⁹ The most evident consequence of non-sphericity is a slight reduction of the optical thickness ρ with respect to spheres. This has to be taken into account when interpreting data and assessing an equivalent refractive index. This will be slightly smaller than the value of the bulk material composing the particle, as a consequence of a

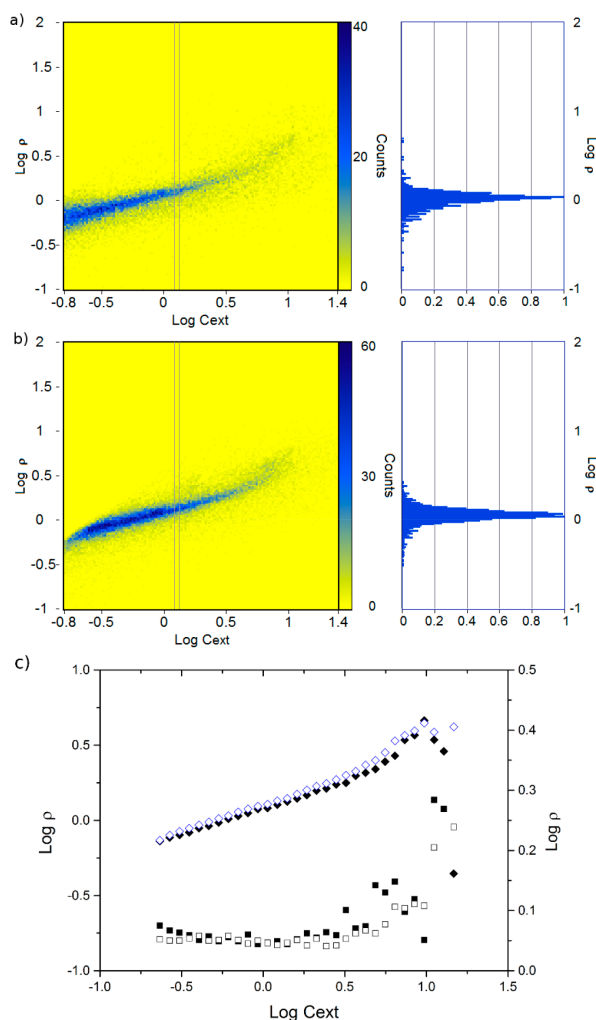


Figure 2. Sample EDC 5316: (left) SPES raw data as the (C_{ext}, ρ) histogram (yellow, zero; blue, maximum value) and (right) ρ distribution for C_{ext} within the two vertical lines, with (a) thin cell, (b) thick cell, and (c) mode (diamonds, left scale) and standard deviation (squares, right scale) of the ρ distribution overall, with the C_{ext} range for the thin cell (open symbols) and thick cell (solid symbols).

smaller average polarizability of the whole particle induced by its shape. Moreover, the refractive index has an influence on sizing, which we will properly take into account in the data analysis.

An aggregate constituted of mineral particles stuck together and partially separated by voids has an average optical thickness τ_0 smaller than a single compact particle of the same material, size, shape, and orientation. At first order, this simply reduces ρ , which can be measured from the SPES data.

Nevertheless, when the shape of an aggregate or of a compact particle is appreciably non-spherical, ρ and τ_0 are affected by particle orientations and, consequently, it is not possible to assign a unique pair (C_{ext}, ρ) to it.^{9,13} Numerical simulations show that a compact particle with a (still reasonable) refractive index and shape/orientation can provide the same SPES signal of a given aggregate. Even the entire set of pairs (C_{ext}, ρ) associated with a population of aggregates with different size distributions and properties (refractive index, internal structure, filling factor, etc.) can be well-reproduced by

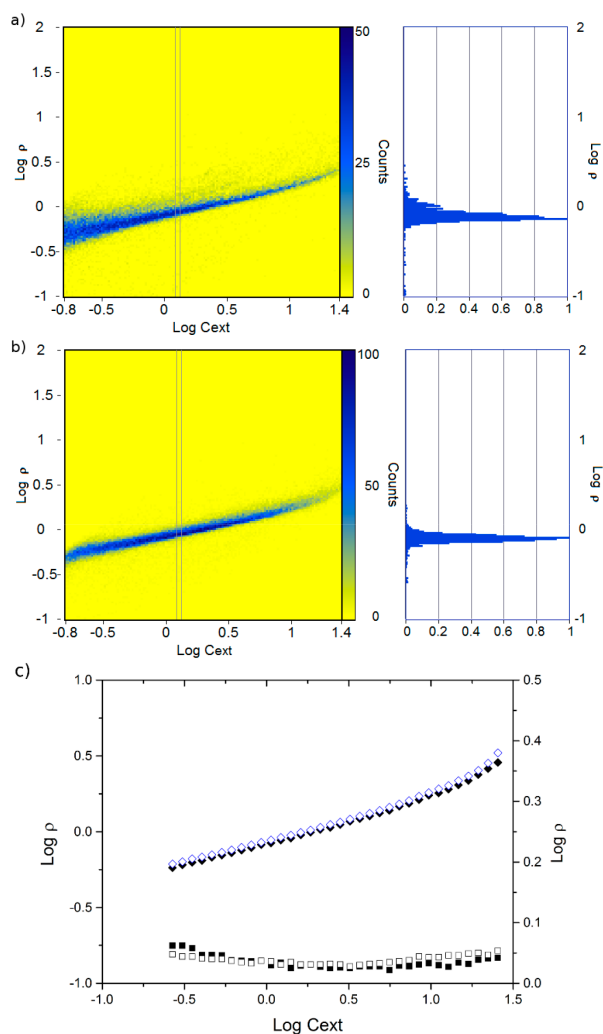


Figure 3. Sample EDC 5534: (left) SPES raw data as the (C_{ext}, ρ) histogram (yellow, zero; blue, maximum value) and (right) ρ distribution for C_{ext} within the two vertical lines, with (a) thin cell, (b) thick cell, and (c) mode (diamonds, left scale) and standard deviation (squares, right scale) of the ρ distribution overall, with the C_{ext} range for the thin cell (open symbols) and thick cell (solid symbols).

a distribution of particles with proper shape and orientation. More precisely, a population of aggregates can be closely reproduced by proper prolate (needle-like) particles oriented perpendicularly to the incoming light beam. This means that the result of SPES measurements performed on aggregate particles can be interpreted as a result of either prolate compact particles or aggregates.

As stated above, this problem is circumvented by sequentially operating two SPES devices: in the first, particles are brought into the light beam through a thin cell, inducing a shear that

gives preferable orientation to non-spherical particles, and in the latter, optically identical to the former, the cell is thick enough to avoid particle orientation.⁹ In this way, comparing the results of both devices, we first recognize samples populated by isometric particles and then measure the average optical thickness.

In the study by Villa et al.,⁹ a detailed discussion and interpretation of the results obtained by orienting or not the particles in the scattering volume is provided in terms of experimental results, numerical simulations, and a simple

mathematical model. As explained and experimentally proven in that paper, isometric particles necessarily give rise to populations with a limited spread in ρ in both cells (because orientations are almost ineffective in changing τ_0). Oblate (disk-like) particles produce distributions with appreciable spread in ρ in both cells, while prolate (needle-like) particles have a limited spread with the thin (particle-orienting) cell and appreciable spread with the thick (non-orienting) cell. As a result, by comparing the twin measurements with and without orientation, we select samples with limited spread in ρ in both cells and no (or limited) differences in oriented and non-oriented measurements. This guarantees that orientation is not really affecting the SPES results, as strongly expected for isometric particles, as discussed above. Here, we use this criterion to identify samples mainly composed of isometric particles and analyze them to measure the optical thickness and equivalent refractive index of each particle.

In Figures 1, 2, and 3, we show the SPES raw data obtained for samples EDC S768, EDC S316, EDC S534, respectively, as two-dimensional (2D) histograms in the (C_{ext} , ρ) plane. Measurements obtained with the thin cell are shown in each figure at the top, while measurements performed with the thick cell are shown at the bottom. Following Potenza et al.,⁹ log-log scales are used, and colors represent the number of events for each 2D bin, normalized to the maximum value of each plot (yellow). Yellow is zero, and blue is the maximum value. The main elongation of the data is given by size polydispersity of the sample, while the difference in the refractive indices and/or shape and orientation affect the vertical (ρ) broadening. Each data set is presented with a plot of a vertical section evaluated in correspondence of the vertical lines in the 2D histogram (the same C_{ext} range for all of the samples). These plots are used to evaluate both the mode (left scale) and width (standard deviation, right scale) in the case of unimodal distributions in ρ or to extract information from more structured distributions. In such a way, we have a quantitative evaluation of the correspondence between the measurements with the thin and thick cells and, therefore, how valid is the assessment of the isometric shape of the particles. When aggregates are present, they can be recognized by a smaller optical thickness ρ (or a smaller equivalent refractive index) compared to compact single mineral grains.

Data analysis is based on standard lookup tables (LUTs)⁸ specifically designed and generated to interpret SPES data for isometric particles. The LUT assigns to each measured particle the corresponding value of the equivalent refractive index, m , related to the average polarizability of the particle and the volume equivalent diameter, D .

We note that particle size distributions (PSDs) obtained from extinction cross sections when the equivalent refractive index is known for each particle are much more reliable than in cases when the refractive index is assumed *a priori*, as performed by traditional extinction measurements.¹² From the 2D (C_{ext} , ρ) plots, further checks can be performed to estimate, for example, how the equivalent refractive index is maintained across the size range, meaning how the filling factor is maintained uniform in the population. Another check is performed to verify if isometric shapes are maintained along the size range (see the Supporting Information). All of this information can then be used to give a quantitative evaluation of the uncertainties of the results.

For each sample, we show the 2D histogram of the number of counts as a function of the diameter and equivalent refractive

index, as obtained by the LUT. This plot gives information about the degree of compactness of the population of particles measured, thus showing the difference between compact and aggregate particles. The equivalent refractive index for compact particles can be converted into the corresponding bulk index by comparing the optical thickness of spheres and shaped, isometric particles. As shown below, the resulting indices range between 1.50 and 1.55, as expected for mineral dust.¹⁷ This allows us to distinguish aggregates from compact particles by simply imposing a threshold in the equivalent refractive index represented by the refractive index value in water, $m = 1.07$ (vertical dashed lines in Figures 4a, 5a, and 6a). This delineation comes after conducting accurate numerical simulations for isometric non-spherical particles of bulk indices

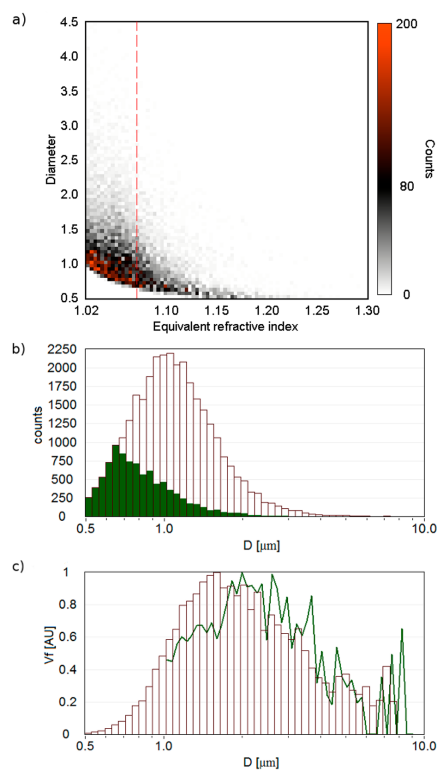


Figure 4. Results of the SPES analysis for the sample EDC S768 (see Figure 1). (a) Two-dimensional histogram indicates the number of counts obtained in the (D , m) plane, according to the analysis performed with the LUT, as described in the text. The vertical dashed line represents the threshold in m below which the events can be safely attributed to aggregates. (b) We show the number distribution as a function of the diameter accordingly to the results in panel a. The size distribution for aggregates ($m < 1.07$) is represented in green as a fraction of the total. (c) We compare the volume distributions obtained from data in panel b to Coulter counter measurements (green line) of the same sample.

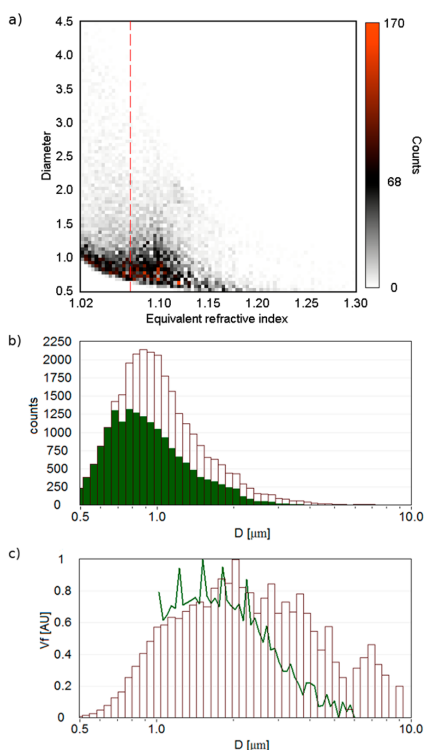


Figure 5. Same as in Figure 4 for the sample EDC 5316 (see Figure 2). (a) Two-dimensional histogram in the (D , m) plane. The vertical dashed line is the aggregate m threshold. (b) Number distribution (green, aggregates; white, compact particles). (c) Volume distribution from panel b compared to Coulter counter measurements (green line). Notice the marginal presence of aggregates, which nonetheless affects the volume size distribution at the largest sizes.

down to 1.47, showing that equivalent refractive indices lower than 1.43 can only be compatible with non-compact objects.

Each data set is then associated with the index and size distributions. In Figures 4b, 5b, and 6b, we distinguish the two populations of compact particles ($m > 1.07$, green) and aggregates ($m < 1.07$, white). We also converted the overall PSD from number to volume distribution to compare to Coulter data, also represented in the plots.

Finally, we stress that the comparison of the results obtained by processing data from both cells is fully compatible for all of the samples considered here, thus confirming once more the validity of the choice of selecting populations of isometric particles. Therefore, in the following section, we report the results obtained from the thin cell.

To provide further support to our results, we placed some of the samples in an ultrasonic bath to destroy aggregates, following the protocol adopted by Lambert et al.¹ In comparison of the SPES measurements before and after sonication, information about changes in the agglomeration state of the aggregates and their constituents can be obtained.

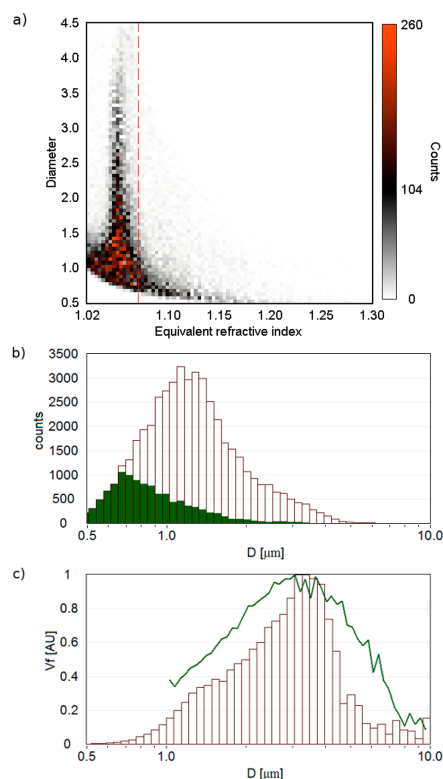


Figure 6. Same representation of the previous figures for the sample EDC 5534 (see Figure 3). (a) Two-dimensional histogram in the (D , m) plane. The vertical dashed line is the aggregate m threshold. (b) Number distribution (green, aggregates; white, compact particles). (c) Volume distribution from panel b compared to Coulter counter measurements (green line). The presence of aggregates is rampant even at the larger sizes, thus heavily affecting the volume size distribution in panel c.

RESULTS AND DISCUSSION

We present the SPES results obtained from samples selected from the deeper part of the EPICA Dome C ice core, where dust aggregate formation is known to occur below 2900 m depth approximately.^{1,4}

We report evidence of samples showing the presence of aggregates that we characterize following the procedure described above. We also show the case of a sample showing almost no aggregates and a sample of oblate particles that prevents our analysis from being performed. Some samples have been characterized using Coulter counter, optical microscopy, and scanning electron microscopy (SEM) to verify the results obtained through the SPES and our analysis methods.

As detailed in the Supporting Information, we selected samples mainly composed of isometric particles, such that the LUT could be exploited to recover the size and equivalent

refractive index of each particle. SPES raw data plotted in the (C_{ext} , ρ) plane, obtained with both cells and the comparison of the mode and width of the vertical distributions, are shown in the [Supporting Information](#).

Panel a shows the 2D histogram of the diameter versus equivalent refractive index, while panel b gives the corresponding PSD histogram for compact (green) and aggregate (white) particles, with stacked bars. Finally, in panel c, we report the corresponding volume fraction distribution, which is, in turn, compared to Coulter counter data (solid line).

[Figure 4](#) shows the results obtained for sample EDC 5768 (about 3172 m depth in the core). It is characterized by isometric particles ([Figure 1](#)) within a very good approximation. By applying the LUT discussed above, we turn out with a set of pairs (D , m), plotted in panel a as a 2D histogram. In this sample, we note that almost the entire population lies below the equivalent refractive index $m = 1.07$ (vertical line). Only a small fraction of the particles shows an equivalent refractive index still compatible with compact objects. Panel b shows the PSD obtained from the LUT for the compact particles ($m > 1.07$, solid histograms), and the aggregates ($m < 1.07$, white histograms). Notice that the whole PSD is characterized by compact particles at the smaller sizes, while aggregates become progressively more important with increasing size, as expected. However, aggregates appear also within the smallest size range, a feature that cannot be determined on the basis of Coulter counter measurements only. In panel c, we show the comparison between the volume distributions obtained by SPES data and the Coulter counter measurements performed on the same water sample. The same sample has been characterized via optical microscopy and SEM and shows the presence of aggregates with different sizes, as obtained by our analysis. Results are reported in the [Supporting Information](#), where a typical SEM picture is shown.

For comparison, in [Figure 5](#), we report the case of the sample EDC 5316 (2923 m depth in the core) presenting a very limited amount of aggregates, as suggested by Coulter counter measurements, optical microscopy, and SEM. Again, the analysis of the SPES raw data (see the [Supporting Information](#)) indicates the presence of isometric particles. The 2D (D , m) histogram (panel a), obtained through the LUT of above, shows that the majority of the particles lies above the threshold at the equivalent refractive index $m = 1.07$ (vertical line). Panel b shows the PSD obtained from the LUT for the compact particles ($m > 1.07$, solid histograms) and the aggregates ($m < 1.07$, white histograms). Aggregates exhibit mainly larger sizes but are present across the particle size spectrum. Thus, our results show that the whole population presents aggregates, although not so large as to be detected through anomalous Coulter counter size. This accounts for the apparent lack of aggregates suggested by Coulter measurements (solid line in panel c). Careful inspection via optical microscopy and SEM actually revealed the presence of small aggregates in accordance with our measurements (see the [Supporting Information](#)).

To check the reliability of these results, we placed the sample in an ultrasonic bath for 5, 10, and 15 min. The small fraction of aggregates apparently disappeared after a few minutes of sonication. In addition, the 2D histogram in the (C_{ext} , ρ) plane suggests the presence of a population of non-isometric particles (probably platelets, such as phyllosilicates), appreciably smaller compared to the size of aggregates measured before sonication. Moreover, the distribution of isometric, compact particles ($m > 1.07$) was almost unchanged in terms of both the PSD shape

and number of particles, as expected. This validates on the first order the approach used by Lambert et al.¹ for assessment of the dust concentration from Coulter counter measurements in the bottom part of the EPICA ice core (see the [Supporting Information](#)). We are aware, however, that in some cases, even sonication is not able to completely destroy aggregates.

[Figure 6](#) shows the case of a sample showing almost complete aggregation, sample EDC 5534 (about 3043 m depth in the core). This very concentrated sample appears very peculiar in Coulter counter measurements, showing large particles still lognormally distributed, interpreted as aggregates. SPES data also show a very extended population up to very large sizes. From the (C_{ext} , ρ) plots (see the [Supporting Information](#)), the isometric shape can be clearly assessed across the population. Applying the LUT, we obtain evidence that a low equivalent refractive index characterizes almost all of the sample (panel a). Applying the approach for aggregate detection described above, we deduce that this sample is mainly composed of aggregates (panel b), even at sizes where Coulter counter cannot give any information about possible aggregation. In panel c, we compare the volume size distribution obtained using the SPES method and Coulter counter. Differences between the optical and volume equivalent sizes are even more evident here, because of the non-compact structures characterizing the aggregates.

Besides the agreement with the results from Coulter counter measurements, this result is also in accordance with the high dust concentration of the sample, from which we expect a corresponding higher probability for particles to undergo aggregation within ice. We note that a high probability of aggregation is expected also for particles in meltwater. To circumvent this problem, we first diluted the samples and then performed measurements within a very short time after melting, much shorter than the characteristic time of aggregation for micrometer-sized particles suspended in solution with a similar concentration.^{9,18} However, measurements performed within a few hours from melting showed no appreciable differences, thus confirming the stability of the dust suspension during our measurements.

To better inspect the agglomeration state of these grains, we placed the diluted samples in an ultrasonic bath for 5, 10, and 15 min. The presence of aggregates decreased by increasing the sonication time, as expected, and at the end of the last sonication cycle, the 2D distributions of samples suggest a population of platelets for the constituents, which can reasonably be assumed to be phyllosilicates (see the [Supporting Information](#)). In particular, in the case of sample EDC 5316, the fraction of aggregates almost disappeared after a few minutes of sonication. Therefore, when the fraction of particles showing non-isometric shapes was removed from the analysis, the size distribution was almost unchanged in terms of both PSD shape and number of particles, as expected. This could validate the approach used by Lambert et al.¹ for the assessment of the dust concentration record from Coulter counter measurements in the bottom part of the EPICA ice core. Notice that we cannot exclude the presence of more compact, small isometric aggregates resilient to treatment by an ultrasonic bath.

In conclusion, our results appear to be in good accordance with a very basic understanding of any system composed of particles undergoing aggregation. Roughly, the presence of aggregates seems to be more pronounced for the samples with the highest concentrations, which is logical as a result of the

increased probability of two particles encountering each other and sticking together. Notwithstanding the complexity of the aggregation phenomena in ice cores, which differ significantly from basic aggregation processes of colloids in liquids, it seems that this relation is also valid for dust aggregation in ice. If confirmed by more extended analyses, this could represent a further piece of information for interpreting dust data from deep ice cores and understanding the formation of the aggregates themselves. An intrinsic limitation of our approach is that we cannot recognize aggregates characterized by very compact structures, almost completely filled, appearing as one larger grain.

The method proposed in this paper allows for the detection of dust aggregates of different sizes in liquid suspensions and can be potentially implemented in continuous flow analysis systems typically used in ice core research.

■ ASSOCIATED CONTENT

● Supporting Information

The Supporting Information is available free of charge on the ACS Publications website at DOI: 10.1021/acsearthspacechem.7b00018.

Application of the SPES method to the analysis of dust aggregates in meltwater samples from ice cores (PDF)

■ AUTHOR INFORMATION

Corresponding Author

*E-mail: marco.potenza@unimi.it.

ORCID

M. A. C. Potenza: 0000-0002-9379-6540

Notes

The authors declare no competing financial interest.

■ ACKNOWLEDGMENTS

This work is a contribution to the EPICA, a joint European Science Foundation/European Commission scientific programme, funded by the European Union (EU) and national contributions from Belgium, Denmark, France, Germany, Italy, the Netherlands, Norway, Sweden, Switzerland, and the United Kingdom. The main logistic support was provided by the French Polar Institute Paul-Émile Victor (IPEV) and National Antarctic Research Program (PNRA) (at Dome C) and Alfred Wegener Institute (AWI) (at Dronning Maud Land). This is EPICA publication 308.

■ REFERENCES

- (1) Lambert, F.; Delmonte, B.; Petit, J. R.; Bigler, M.; Kaufmann, P. R.; Hutterli, M. A.; Stocker, T. F.; Ruth, U.; Steffensen, J. P.; Maggi, V. Dust–climate couplings over the past 800,000 years from the EPICA Dome C ice core. *Nature* **2008**, *452*, 616–619.
- (2) Petit, J. R.; Delmonte, B. A model for large glacial–interglacial climate-induced changes in dust and sea salt concentrations in deep ice cores (central Antarctica): Paleoclimatic implications and prospects for refining ice core chronologies. *Tellus, Ser. B* **2009**, *61*, 768–790.
- (3) Delmonte, B.; Petit, J. R.; Andersen, K. K.; Basile-Doelsch, I.; Maggi, V.; Ya Lipenkov, V. Dust size evidence for opposite regional atmospheric circulation changes over east Antarctica during the last climatic transition. *Clim. Dynam.* **2004**, *23*, 427–438.
- (4) De Angelis, M.; Tison, J. L.; Morel-Fourcade, M. C.; Susini, J. Micro-investigation of EPICA Dome C bottom ice: Evidence of long term in situ processes involving acid–salt interactions, mineral dust, and organic matter. *Quat. Sci. Rev.* **2013**, *78*, 248–265.

- (5) Tison, J. L.; de Angelis, M.; Littot, G.; Wolff, E.; Fischer, H.; Hansson, M.; Bigler, M.; Udisti, R.; Wegner, A.; Jouzel, J.; Stenni, B.; Johnsen, S.; Masson-Delmotte, V.; Landais, A.; Lipenkov, V.; Loulergue, L.; Barnola, J.-M.; Petit, J.-R.; Delmonte, B.; Dreyfus, G.; Dahl-Jensen, D.; Durand, G.; Bereiter, B.; Schilt, A.; Spahni, R.; Pol, K.; Lorrain, R.; Souchez, R.; Samyn, D. Retrieving the paleoclimatic signal from the deeper part of the EPICA Dome C ice core. *Cryosphere* **2015**, *9* (4), 1633–1648.
- (6) Bohren, C. F.; Huffman, D. R. *Absorption and Scattering of Light by Small Particles*; John Wiley & Sons: New York, 2008.
- (7) Sorensen, C. M. Light scattering by fractal aggregates: A review. *Aerosol Sci. Technol.* **2001**, *35* (2), 648–687.
- (8) Potenza, M. A. C.; Albani, S.; Delmonte, B.; Villa, S.; Sanvito, T.; Paroli, B.; Pullia, A.; Baccolo, G.; Mahowald, N.; Maggi, V. Shape and size constraints on dust optical properties from the Dome C ice core, Antarctica. *Sci. Rep.* **2016**, *6*, 28162.
- (9) Villa, S.; Sanvito, T.; Paroli, B.; Pullia, A.; Delmonte, B.; Potenza, M. A. C. Measuring shape and size of micrometric particles from the analysis of the forward scattered field. *J. Appl. Phys.* **2016**, *119* (22), 224901.
- (10) Potenza, M. A. C.; Sanvito, T.; Pullia, A. Measuring the complex field scattered by single submicron particles. *AIP Adv.* **2015**, *5* (11), 117222.
- (11) van de Hulst, H. C. *Light Scattering by Small Particles*; Dover Publications: New York, 1981.
- (12) Potenza, M. A. C.; Milani, P. Free nanoparticle characterization by optical scattered field analysis: Opportunities and perspectives. *J. Nanopart. Res.* **2014**, *16* (11), 2680.
- (13) Potenza, M. A. C.; Sanvito, T.; Pullia, A. Accurate sizing of ceria oxide nanoparticles in slurries by the analysis of the optical forward-scattered field. *J. Nanopart. Res.* **2015**, *17* (2), 110.
- (14) Potenza, M. A. C.; Sanvito, T.; Argenti, S.; Cella, C.; Paroli, B.; Lenardi, C.; Milani, P. Single particle optical extinction and scattering allows real time quantitative characterization of drug payload and degradation of polymeric nanoparticles. *Sci. Rep.* **2016**, *5*, 18228.
- (15) Ruth, U. Concentration and size distribution of microparticles in the NGRIP ice core (Central Greenland) during the Last Glacial Period, Ph.D. Dissertation, Bremen University, Bremen, Germany, 2002.
- (16) Wegner, A.; Fischer, H.; Delmonte, B.; Petit, J.-R.; Erhardt, T.; Ruth, U.; Svensson, A.; Vinther, B.; Miller, H. The role of seasonality of mineral dust concentration and size on glacial/interglacial dust changes in the EPICA Dronning Maud Land ice core. *J. Geophys. Res.: Atmospheres* **2015**, *120* (19), 9916–9931.
- (17) Gaudichet, A.; Petit, J. R.; Lefevre, R.; Lorius, C. An investigation by analytical transmission electron microscopy of individual insoluble microparticles from Antarctic (Dome C) ice core samples. *Tellus, Ser. B* **1986**, *38B*, 250–261.
- (18) Hiemenz, P. C.; Dekker, M. *Principles of Colloid and Surface Chemistry*; Better World Books: Mishawaka, IN, 1977.

Fractal aggregates

We devote this chapter to the study of colloidal fractal aggregates of calibrated spheres based on polystyrene¹ as a further example of composite, non-spherical particles, whose peculiar structure attracted the attention of much research and are very well characterised. Sorensen (2001) and Bushell et al. (2002) outline the main experimental results and theoretical models on the subject by drawing on a wide range of sources. The significance this kind of aggregates is more general than it may seem. Despite they are not likely to be found as such outside a laboratory setting, they provide a model for a wide variety of particles resulting from aggregation processes. For example, they share a strong morphological resemblance with soot (figure 4.1) and combustion-related particles (Mackowski, 1995). Moreover, micro-plastics in the micron size range have recently become a matter of environmental concern (Bergmann et al., 2017).

From a morphological perspective, when small, solid particles randomly collide and bind together, the resulting structures often exhibit a certain degree of self-similarity and scale invariance. This earned them the name of fractal aggregates (Wang and Sorensen, 2002).

Examples of fractal aggregation are found in the growth of snowflakes or sedimentation in river deltas, some bacteria and micro-algae in biology, cosmic dust in astrophysics, the assembling of metal nanoparticles and carbon nano-tubes (Weitz and Oliveria, 1984, Fairbanks et al., 2011). Some of these systems have been found to be distinguished by fundamental universality properties (Lin et al., 1989, Weitz and Lin, 1986).

The structural properties of such aggregates depend on both the characteristics of the primary particles and the growth dynamics, including the probability of bonding as a consequence of collision. The main distinction is between Brownian aggregation and ballistic aggregation.

The radiative properties of a fractal aggregate are tightly and non-trivially related

¹Specifically, polystyrene sulphonate colloidal particles produced by polymerisation of styrene under conditions that induce spontaneous coalescent bead formation, stabilised by a negative surface charge.

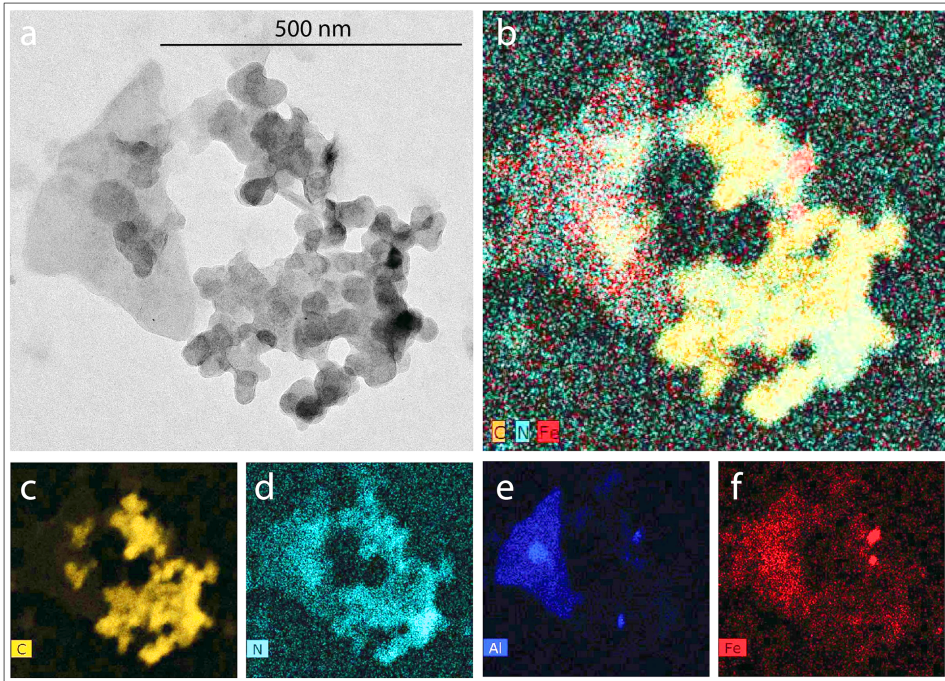


Figure 4.1: Dust particle attached to a black carbon aggregate incorporating aluminium and iron dust particles, dated to 1838 C.E. (a) Transmission Electron Microscope image (b) Overlaid carbon, nitrogen, and iron Energy-dispersive X-ray spectroscopy maps, showing the connection of the iron particles to the BC aggregate with nitrogen-rich coating. (c–f) Carbon, nitrogen, aluminium and iron maps respectively. Taken from Ellis et al. (2016)

to their structure, as it was anticipated in the derivation of the model in section 2.5. As will be thoroughly discussed later on, they can hardly find their place in the Lorentz–Mie theoretical setting of spherical particles².

4.1 Morphological features of fractal aggregates

Firstly, it should be defined what is meant by the *size* of such irregularly shaped particles. A common estimate is given by the radius of gyration, defined as the root mean square distance of the particles from the centre of mass of the aggregate:

²Besides, common solid geometry falls short of providing a satisfactory description of any fractal system (Lennon et al., 2015)

$$R_g^2 = \frac{1}{N} \sum_{i=1}^N |\mathbf{r}_i - \mathbf{r}_{cm}|^2 \quad (4.1)$$

where N is the number of primary particles, \mathbf{r}_i are their coordinates and \mathbf{r}_{cm} is the centre of mass, which can be set to zero by choosing a proper reference frame. Alternatively, the Hydrodynamic, Gyration or Stokes radius may be used to give an estimate of the size depending on the context (Potenza et al., 2010b).

We now introduce the fundamental scaling relation (Bushell et al., 2002) that describes the fractal nature of such aggregates

$$N = k_0 \left(\frac{R_g}{a} \right)^{d_f} \quad (4.2)$$

where d_f is called the *fractal dimension*, k_0 is a prefactor of order unity (Wang and Sorensen, 2002) and a is the radius of the particles. We will provide an experimental measurement of the prefactor, k_0 , and of the fractal dimension d_f .

The prefactor depends on the parameter chosen for defining the size of the aggregate³ and is related to the fractal dimension (Sorensen and Roberts, 1997).

The fractal dimension gives an indication of the compactness of the aggregate. It may range between 1 for a linear chain of particles, up to 3 for a bulk, compact structure as in solid geometry. In our case, the fractal dimension has an intermediate value, around $d_f \simeq 1.7$. Interestingly, this value approaching 2 suggests that the mass of the particle may be essentially distributed on a surface, as a thin foil. The closer d_f is to 1, the more voids such foil has. If we consider an aggregate of radius R growing isotropically, every new layer will contain a number of particles scaling as slightly less than R .

Central to the theoretical approach to the scattering from fractal aggregates is their structure factor (section 2.1). Let us now briefly dwell upon some general conditions the correlation function, $g(\mathbf{r})$, of an arbitrary aggregate of particles must meet. This quantity represents the probability of finding a particle at any given position relative to another particle⁴ and is closely related to the structure factor (see equation (2.2)).

We assume the particles in the aggregate all have a size (radius) can be set around a value a . Two quantities, a and R_g , define the relevant length scales of the scatterer. With these premises, a few general criteria might be established (Sorensen et al., 1992, Bushell et al., 2002):

³For instance, for a sphere of radius R $R_g = \sqrt{\frac{3}{5}} R$. However, this choice does not change the functional form of the law in equation (4.2)

⁴The variable \mathbf{r} in $g(\mathbf{r})$ stands for the vector joining the positions of a pair of particles. It is replaced by its modulus, r , if the probability is assumed to depend only on the mutual distance.

- i) Particles in the aggregate should be non-overlapping:

$$g(\mathbf{r}) = 0 \quad \text{if} \quad |\mathbf{r}| < 2a$$

The spatial arrangement of particles in the aggregate must include this anti-correlation.

- ii) Particles are in contact with each other, thus the probability of finding at least one neighbour tends to 1 with increasing r , thus g reaches its maximum:

$$g(\mathbf{r}) \rightarrow g_{\max} \quad \text{if} \quad R_g \gtrsim |\mathbf{r}| \gg 2a$$

this brings in a certain degree of correlation between the particle positions.

- iii) The aggregate is finite in size, so that the probability of finding a particle vanishes at a large distance from the centre of mass:

$$g(\mathbf{r}) \rightarrow 0 \quad \text{if} \quad |\mathbf{r}| \gg R_g$$

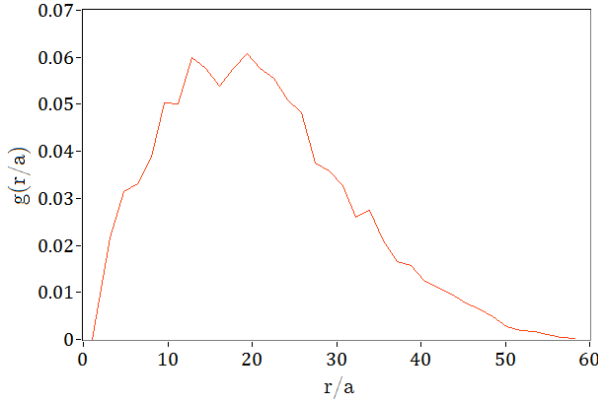


Figure 4.2: Correlation function of a simulated aggregate of 1000 spherical particles. Notice that g vanishes for $r < 2a$, as a result of the non-overlapping condition, and it vanishes for large r since the system is limited in size.

An example of the correlation function of a simulated fractal aggregate is shown in figure 4.2. The particle is composed of one thousand spherical monomers forming chains which in turn are arranged in an open, branched structure. The conditions outlined above and equation (4.2) provide the ground on which to build the model of the structure factor of fractal aggregates, $S_s(q)$. The scale-invariance of fractal aggregates is reflected in the trend of their structure factor. Its most notable feature

is that for large q (Sorensen, 2001)

$$S_s(q) \sim \frac{C}{(qR_g)^{d_f}} \quad (4.3)$$

where C is a constant of order unity. For vanishing q we have $S_s(q) \rightarrow 1$, as in the general case seen in section 2.1.

An exact expression of $S_s(q)$ is given in terms of Kummer's confluent hypergeometric function ${}_1F_1(a, b; z)$ (Sorensen et al., 2018)

$$S_s(q) = {}_1F_1\left(\frac{3-d_f}{2}, \frac{3}{2}, \frac{(qR_g)^2}{d_f}\right) e^{-(qR_g)^2/d_f} \quad (4.4)$$

The aim is to use this expression in equations (2.57): to simplify the integrals, we may adopt the following approximation that captures the asymptotic behaviour of equation (4.4) (see figure 4.3):

$$S_s(q) = \frac{1}{N} + \min\left\{\frac{N-1}{N}; C/(qR_g)^{d_f}\right\} \quad (4.5)$$

where the first term accounts for the excluded volume contribution (Parola et al., 2014). The slight discrepancy close to the roll-off of equations (4.4) and (4.5) is found to be negligible once the expression is integrated in equations (2.62).

The structure factor of fractal aggregates has been thoroughly characterised by experiment (Sorensen, 2001, Lattuada et al., 2003, Potenza et al., 2014) and is highly reproducible, and has a minimum number of free parameters. For a single aggregate, $S(q)$ might deviate from the curve shown in figure 4.3, especially at large q , due to the particular arrangement of the monomers defining its fine structure. To avoid such ambiguity, we will consider averages over different statistical conformations and orientations of fractal aggregates sharing the same parameters N, R_g , and d_f (see section 4.5).

Under the assumptions of the RDG model, the structure factor of a fractal aggregate averaged over all possible orientations can be expressed by combining equations (2.8) and (2.6) to yield

$$S_s(q) = \frac{P(q)}{N^2} \sum_{i \neq j=1}^N \text{sinc}(q|\mathbf{r}_i - \mathbf{r}_j|) \quad (4.6)$$

This requires to know the positions \mathbf{r}_i of the centres of all the particles in the aggregate and therefore is a viable option only with simulations (see for example figure 4.14). This model is in very good agreement with the curve given in figure 4.3.

The effectiveness of optical methods in the study of colloidal fractal aggregates is established by a large volume of publications concerning dynamic light scattering

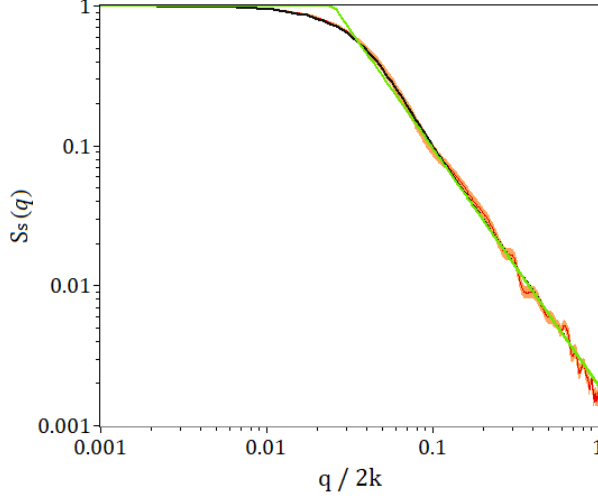


Figure 4.3: Structure factor of a fractal aggregate with $R_g = 1.5 \mu\text{m}$ and $d_f = 1.75$. A black solid line indicates the model in equation (4.4). The approximation given in equation (4.5) is shown in green. The red line with error bars is obtained by ADDA averaging over 100 random orientations.

(Berne and Pecora, 2000, Goldburg, 1999), low angle light scattering (Ferri et al., 1988) and turbidimetry (Ferri et al., 2015). In these approaches, statistical averages obtained with light scattering methods allow to set some of the fundamental physical parameters appearing in equation (4.2) and the static structure factor. Results can be compared with experimental data from other methods as well as with theory.

In this work, we focus on the complex amplitude of the field scattered forward by single aggregates (section 1.1), which is related to the structure factor by the optical theorem, as we have seen in section 2.5.

With the expression (4.5) we can integrate the formulae of the model given in section 2.5 for the special case of fractal aggregates.

As a reference, we may substitute the expression in equation (4.5) for the structure factor into equations (2.62) by taking $\frac{N-1}{N} \rightarrow 1$ and $kR_g \gg 1$. This leads to somewhat more explicit relations for the forward scattering amplitude in terms of the morphological parameters of scattering aggregates:

$$\Re S(0) = N\tilde{\alpha}^2 \left[a_1 + Ck_0 \left(b_1 - b_2 \left(\frac{Ck_0}{N} \right)^{\frac{2d_f-2}{d_f}} \right) \right] \quad (4.7a)$$

$$\Im S(0) = -N\tilde{\alpha} (1 + a_2 \tilde{\alpha}) \quad (4.7b)$$

where a_1 and a_2 are dimensionless constants which only depend on the product ka , i.e. the radius of the monomers and the wavenumber of the laser radiation, while b_1 and b_2 are dimensionless constants that depend on ka and d_f ; none of the constants depends on R_g or N . In our case, all these constants are of order unity⁵, while the dimensionless polarizability $\tilde{\alpha} = \alpha k^3 = 0.0352$. As a result, the formulas in 4.7 suggest that $\Im S(0) \propto \Re S(0)$, with a slope of order unity that does not depend on the fractal dimension of the particles (see section 4.3 for further details.).

For the sake of comparison, from equations (2.32) a scaling relation for fractal aggregates can be obtained by applying the Maxwell-Garnett approximation (section 1.5) (Potenza and Milani, 2014, Sorensen, 2001):

$$\Im S(0) \sim \Re S(0)^{d_f/(2d_f-2)} \quad (4.8)$$

In such picture, each aggregate is represented as an homogeneous sphere of radius R_g and its *equivalent* refractive index is obtained with equation (1.24). According to this model, the distribution of forward scattering amplitudes from polydisperse fractal aggregates should follow a power law that depends on their fractal dimension. In particular, the slope in equation (4.8) is greater than one if $d_f < 2$, and vice versa. Notably, the real part of the scattering amplitude vanishes if the fractal dimension approaches unity. Notably, it can be shown that the model in equations (2.62) reduces to (4.8) by substituting the structure factor of a spherical particle. The two models above give two conflicting scaling laws for the fractal aggregates. Taking advantage of the size polydispersity in our samples and the consequent extended distribution of $S(0)$, we can compare our data with both models without any free parameter. This approach will show the limits of equation (4.8), introduced by the Effective Medium Approximation, as already foreseen by Sorensen (2001).

4.2 Aggregates of polystyrene sulphonate spheres

We now turn to the procedure adopted for preparing the fractal aggregates we studied; the experimental methods are detailed in appendices A and B. An example of a simulated aggregate is shown in figure 4.4.

Among the reasons for the widespread investigation of colloidal fractal aggregates as a simple model for complex systems are the ease of control of the parameters driving their growth and the reproducibility of the resulting structures. Given the

⁵In particular, setting $ka = 0.659$ and $d_f = 1.75$ yields $a_1 = 0.56$, $a_2 = 1.07$, $b_1 = 4.22$ and $b_2 = 4.03$. We use laser light $\lambda = 0.635 \mu\text{m}$; in water $k = 13.2 \mu\text{m}^{-1}$, while the monomers considered here are polystyrene spheres 100 nm in diameter.

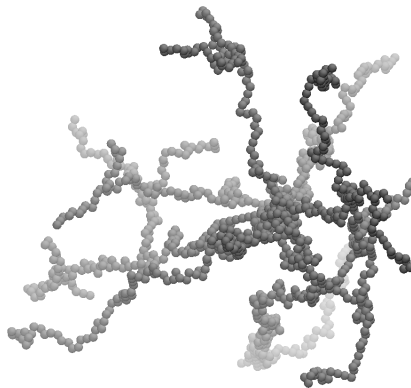


Figure 4.4: Fractal structure with $N = 1150$ and ratio $R_g/a = 49$, hence $d_f = 1.77$, generated *in silico* as described in section 4.5. The radius of gyration is $R_g = 2.45 \mu\text{m}$ if the monomer radius is taken $a = 0.05 \mu\text{m}$. This value can be set when running the DDA calculations.

scope of this work, we are more interested in the resulting structures than in the detailed dynamics of aggregation. While the size of the aggregates depends to some extent on aggregation time, it cannot be controlled precisely and is almost invariably polydisperse. However, we exploit this very feature to our advantage. Before proceeding to review the experimental results in the next section (4.3), we provide a brief description of the sample features.

Random diffusion is essential for producing the scale invariance that distinguishes fractals. The probability that two particles in a colloidal suspension collide at any given time is related to the diffusion coefficient, which determines the *characteristic collision time*. Polystyrene sulphonate beads are subject to inter-particle repulsive forces due to their surface negative charge that keep the sol colloidally stable against the weaker Van der Waals attractive interactions (figure 4.5).

When adding salt to the solution, the dissolved ions screen the electrostatic repulsion between monomers and cause the sol to undergo perikinetic aggregation⁶. Once two particles come in contact with each other, they may form a durable bond or come apart again depending on the effectiveness of the screening. Such sticking probability, in turn, determines the compactness of the resulting fractal structure.

Adjusting the external conditions causes the system to evolve in a range of dif-

⁶In colloidal suspensions, aggregation is called perikinetic when collisions between particles are caused by their Brownian motion, as opposed to orthokinetic aggregation where the process is driven by hydrodynamic motion such as convection or sedimentation.

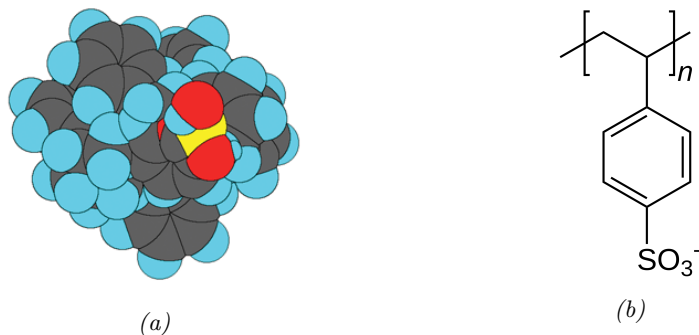


Figure 4.5: (a) Schematic of a section of a commercial polystyrene sulphonate microsphere surface displaying a sulphate group, responsible for the surface charge density of the particle (image taken from Thermo Fisher Scientific). Carbon atoms are depicted in grey, hydrogen in blue, sulphur in yellow and oxygen atoms in red. (b) Polystyrene sulphonate structure.

ferent regimes, with two limiting cases: the Diffusion-Limited Aggregation (DLA), and the Reaction-Limited Aggregation (RLA) (Lin et al., 1989). Previous research reviewed by Sorensen (2001) has shown that the first regime results in a faster aggregation, typified by a fractal dimension ranging between 1.7 and 1.8, and a power law time evolution of the average cluster size (Bushell et al., 2002). Conversely, RLA is a process proceeding at a slower pace, where the average cluster size grows exponentially with time. More importantly, it yields compact Clusters exhibiting a higher d_f , which typically ranges between 2 and 2.1 (Weitz and Lin, 1986, Sorensen and Roberts, 1997).

Different aggregation conditions were explored to find the most suited to our needs. The amount of salt and the monomer concentration determine the morphology of the aggregates (Carpinetti et al., 1990). We chose DLA over RLA to ensure that samples were well differentiated from compact particles while minimising the residence time in the beaker.

Monodisperse polystyrene sulphonate spheres⁷ of sub-wavelength diameter (100 nm monomers, Thermo Fisher Scientific, 3100A) were added in a borosilicate glass beaker of pure, filtered water at room temperature, where they enjoy a certain mobility as a result of random Brownian motion. Number concentration was $\sim 5 \cdot 10^{10}$ particles/ml.

We triggered salt-induced aggregation of the sol by adding a water solution of

⁷At the wavelength of the laser we used for the measurements, $\lambda = 0.635 \mu\text{m}$, the refractive index in vacuum is 1.59; the relative refractive index (in water) is $m=1.19$.

magnesium chloride (MgCl_2) to the suspension. At the very early stages of the process, the suspension was gently mixed by slowly spinning the beaker for a few seconds. Adapting the procedure used by Carpineti et al. (1990) to our samples, we employed a water solution of MgCl_2 at a final concentration of 38 mM, which ensures DLA in a matter of minutes; the aggregation characteristic time of such process⁸ was $\tau_0 \simeq 3 - 4$ s (Carpineti et al., 1990). The same procedure was applied to monomers 70 nm in diameter (Thermo Fisher Scientific, 3070A).

The samples were ready to be measured with SPES after some tens of minutes (~ 30 min). At different stages of the aggregation process, small portions of the sample have been gently picked up and diluted with pure water ~ 1 to $5 - 10$, in order to stop the aggregation process and to set the concentration of aggregates (scatterers) adequate for measurements, taken immediately after dilution. Samples have been flown at a speed $\sim 20 \frac{\text{mm}}{\text{s}}$ through the focal spot of the laser beam of the SPES instrument (appendix A) using a commercial flow-cell (Hellma 170-700 QS). The population of aggregates is polydisperse, which yields a distribution of moduli of the scattering amplitude spanning approximately two orders of magnitude. About $5 \cdot 10^3$ aggregates have been measured in each case.

There is evidence that shear stress favours an increase of compactness of fractal aggregates and, in extreme cases, it can have a detrimental effect on their morphology (Spicer and Pratsinis, 1996; Flesch et al., 1999). Tuning the fluid flow rate through the cell allows to impose different shear conditions to the samples. We made use of this versatility to find flow conditions where the structure of the colloidal aggregates is not appreciably perturbed by the imposed flow. We highlight that the sample is kept still during aggregation whereas the flow is imposed only during measurements on diluted samples and lasts for a negligible time (~ 10 s). This also keeps shear induced flocculation from altering the structure of the aggregates. A number of independent measurements have been performed on the same samples driven with a replica of the flowing system used for SPES measurements (section 4.4). This allowed to easily measure the static form factor of the aggregates whereby to assess their fractal dimension d_f independently. A dedicated apparatus based on Near Field Scattering was used for this purpose (see appendix B). In this respect, it should be pointed out that the optical methods we employ have an effective scattering volume whose smallest linear size is of the order of $10 \mu\text{m}$, so we do not measure particles larger than $R_g \sim 5 \mu\text{m}$ which give signals rejected during data analysis.

⁸The pace at which aggregation proceeds is given by the time scale of the collisions between monomers, $\tau_0 = \frac{3\eta}{4k_B T c_0}$, where η is the dynamic viscosity of water and c_0 is the particle concentration.

4.3 Experimental results

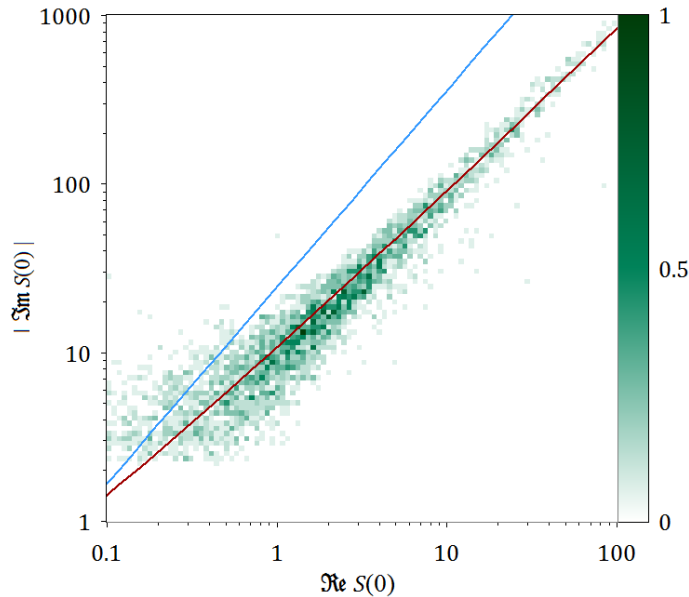


Figure 4.6: Experimental behaviour of $\text{Im}S(0)$ as a function of $\text{Re}S(0)$ from SPES measurements of aggregates obtained from monomers 100 nm in diameter. The two-dimensional histogram agrees with the theoretical behaviour predicted by equations (2.62) ($a = 0.05 \mu\text{m}$, $d_f = 1.75$, $k_0 = 1.20$, red solid line). The behaviour predicted by the Maxwell-Garnett model is shown as a blue solid line, equation (4.8)

In the following pages, we describe the main results from SPES measurements. The custom made instrument we used was assembled on an optical table, and is based on a diode laser-module ($\lambda = 0.635 \text{ nm}$). In its design, it is similar to the one adopted for the measurements detailed in sections 3.3 and 3.3. The technique and the flowing system are described in greater detail in appendix A. In figure 4.6 we show the experimental data obtained from aggregates composed of spheres 100 nm in diameter, 60 minutes after triggering salt-induced aggregation. The plot is a two-dimensional histogram where the counts are represented by a colour gradient scale normalised on its maximum (dark green). Abscissas and ordinates correspond to $\text{Re}S(0)$ and $|\text{Im}S(0)|$, respectively, represented on a log-log scale.

The distribution is clearly extended along the diagonal of the plot, indicating a broad distribution of the moduli $|S(0)|$ due to the polydispersity of the aggregate population (Potenza et al., 2015b). Moreover, the distribution is narrow across the

diagonal of the graph. This finding supports the conclusion that the aggregates in the sample are isometric.

A very important outcome is that $\Re S(0)$ is about one order of magnitude lower than $\Im S(0)$, consequently, the modulus of the forward scattering amplitude is equal to $\Im S(0)$ to a very good approximation, while the phase is small and approximately given by the ratio $\Re S(0)/\Im S(0)$. This is a feature common to all the samples we processed.

Overlaid to the experimental data are the molecular optics model (equations (2.62), red solid line) and the Maxwell-Garnett model (equation (4.8), blue solid line). The data are very well described by the former (section 2.5). Taking advantage of the pronounced polydispersity of the aggregate population, it is possible to compare the slope of the experimental data to theory without any free parameter. Interestingly, in figure 4.6 it can be observed that the two models become more similar at low $|S(0)|$, when the particles are small and their structure contributes less to their scattering properties (Rayleigh limit, section 2.2). Unfortunately, obtaining experimental data for this condition would require much smaller monomers and falls below the sensitivity of our instrument at its current design.

Data shows that $|ImS(0)|$ scales with $ReS(0)$ with a slope approaching unity, in agreement with the molecular optics model. As seen when discussing the approximate relations (4.7), this result does not depend on the fractal dimension d_f . At variance with this behaviour, the Maxwell-Garnett model (equation (4.8)) does not describe observations satisfactorily. All measurements consistently exhibit discrepancies in the slope similar to those evident in this figure. To provide an indication of this discrepancy, according to equation (4.8) the slope should be close to ~ 1.2 for $d_f \sim 1.7$. Equivalently, if we try to infer the fractal dimension from equation (4.8), we obtain a fractal dimension in the range $d_f \simeq 2 - 2.1$, which is incompatible with the samples we are analysing.

We measure the fractal dimension of our samples independently with a method based on Near Field Scattering, as reported in section 4.4. Some details on the experimental method are given in appendix B. With this information, we can set the value of the prefactor in 4.2 to $k_0 = 1.20 \pm 0.1$, by fitting the model (equation (2.62)) to the SPES experimental data.

Similar results arise from the study of fractal aggregates obtained from monomers 70 nm in diameter (figure 4.7). Further examples are given in figures 4.13 and 4.12 in section 4.5, where SPES data is compared to both theoretical models and DDA simulations.

Alternatively, data can be represented in terms of the modulus and phase of the complex scattering amplitude. As an example, in figure 4.8 we report the phase

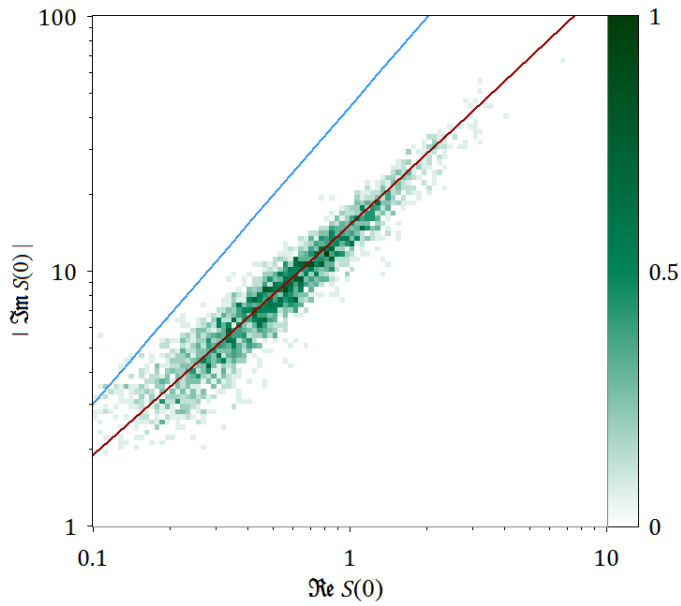


Figure 4.7: Experimental SPES data represented on a two-dimensional histogram for fractal aggregates of monomers 70 nm in diameter after 35 minutes. The model in equations (2.62) is reported as a red solid line ($a = 0.035 \mu\text{m}$, $d_f = 1.75$, $k_0 = 1.20$). As in figure 4.6, the Maxwell-Garnett model is shown as a blue solid line.

distribution in a sample at a given stage of the aggregation process (35 minutes). The monomers are 70 nm in diameter. Again, a 2D histogram is obtained from single particle measurements. In the top-right inset, we report the average phase of each sample, as a function of the aggregation time. The phase is almost constant, and in very good agreement with the theoretical model in equations (2.62). Table

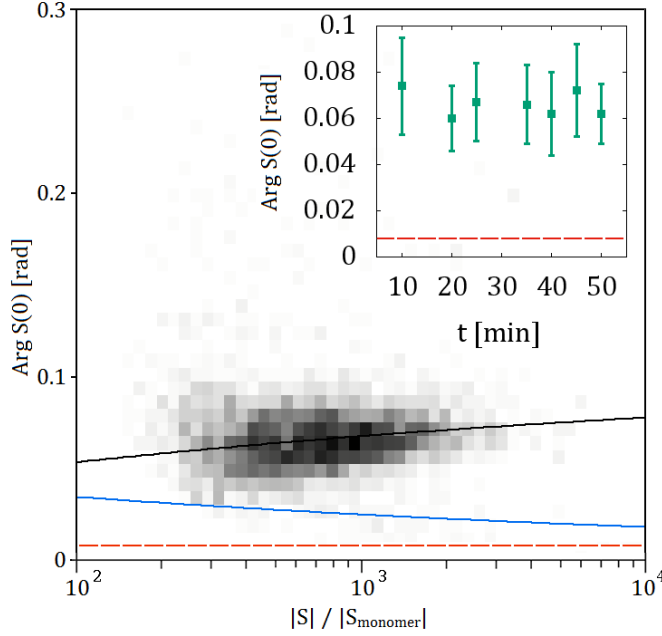


Figure 4.8: Distribution of the phase lags of aggregates of 70 nm monomers after 35 min aggregation. The phase lags are essentially uniform, but they disagree with the Maxwell-Garnett model (blue solid line). The solid black line corresponds to the RDG model. For reference, the red dashed line indicates the phase of the monomer as calculated by ADDA. The inset shows the evolution of the average phase as a function of the aggregation time, upon which it does not show an appreciable dependence.

4.1 illustrates an overview of the SPES results, which all gave consistent outcomes. The minimum salt concentration at which DLA aggregation was successful was 14 mM. In particular, we repeated the aggregation process several times increasing salt concentration up to 100 mM, and aggregation time up to two hours. Neither of those parameters caused evident changes in the average phase of the scattering amplitude, as it can be seen in the fourth column of the table below. A further increase in aggregation time was avoided due to the onset of deposition.

Table 4.1: Overview of the experimental data for the average phase $\langle \text{Arg } S(0) \rangle$ relative to different aggregation conditions. The first three columns report monomer diameter $2a$, aggregation time and salt concentration, respectively. For reference, Mie calculations yield $\text{Arg } S(0) = 0.008 \text{ rad}$ and $\text{Arg } S(0) = 0.02 \text{ rad}$ for 70 nm and 100 nm polystyrene monomers, respectively.

monomer diameter [nm]	time [min]	MgCl ₂ concentration [mM]	$\langle \text{Arg } S(0) \rangle$ [rad]	\pm
70	10	38	0.07	0.02
70	20	38	0.06	0.01
70	20	38	0.07	0.03
70	25	38	0.07	0.02
70	30	38	0.06	0.03
70	35	38	0.07	0.02
70	35	38	0.07	0.02
70	40	38	0.06	0.02
70	45	38	0.08	0.02
70	50	38	0.06	0.01
70	60	38	0.07	0.03
100	30	38	0.10	0.03
100	30	15	0.11	0.03
100	60	30	0.10	0.04
100	60	18	0.13	0.03
100	60	30	0.13	0.03
100	60	50	0.09	0.02
100	60	100	0.09	0.02
100	60	15	0.12	0.03
100	100	14	0.12	0.03
100	120	18	0.13	0.03
100	120	30	0.11	0.03
100	120	15	0.11	0.03

4.4 Near Field Scattering measurements

We exploited an optical method based on Near Field Scattering (NFS) able to operate on flowing samples to characterise independently the samples from the previous section. In particular, we determined the fractal dimension, d_f , and the average phase, $\langle \text{Arg } S(0) \rangle$, of the field scattered by the aggregates with respect to the reference incoming field.

We describe the experimental setup and procedure in appendix B, and we report measurements of calibrated polystyrene spheres compared with Mie calculations. We refer the reader to Potenza et al. (2010b), Mazzoni et al. (2013) and Ferri et al. (2004) for a detailed description of the NFS technique and the underlying model. Briefly, our setup adopts a self-reference interference scheme, similarly to the SPES method, and includes a laser source emitting in the visible spectrum (He-Ne) and a cylindrical lens which focuses the emerging Gaussian beam on a flow-cell. The cylindrical layout allows to overcome the motion blur caused by the flow, and to gather statistically uncorrelated images of the light scattered by the sample in the near field. One-dimensional speckle patterns are recorded by a camera, which are then Fourier-transformed and averaged during data analysis.

Samples were driven through a flow-cell of the same kind (Hellma 170-700 QS) as in the SPES measurements presented so far. We ensured that the conditions undergone by the samples were exactly the same in both cases. This was to check that the samples were not perturbed by the imposed flow and attain consistent information on their morphology.

We outline the results of such measurements in figures 4.9 and 4.10, relating to fractal aggregates of 70 nm and 100 nm polystyrene (sulphonate) monomers, respectively. The figures give a picture of the structure factor of the aggregates, which are in good agreement with the model given in equation 2.5.

With our NFS setup we have access to the average power spectrum of the population of particles up to $q \sim 4 \mu\text{m}^{-1}$, corresponding to a scattering angle in the range $0.1^\circ - 23^\circ$. Measurements are characterised by low angle oscillations given by the interference between the scattered spherical waves and the transmitted plane wave. These oscillations, named after Talbot, can be fitted to NFS data to deliver the information about the phase $\text{Arg } S(0)$.

There are two ranges to be considered: for $q > 0.6 \mu\text{m}^{-1}$ a linear trend is well visible in the log-log plots. A linear fit to such trend gives a measurement of the fractal dimension, which was found to be $d_f = 1.75 \pm 0.01$ and $d_f = 1.76 \pm 0.01$ for the aggregates of 70 nm and 100 nm monomers, respectively. This measurement is crucial to our purposes, since in section 4.3 we demonstrated that it is not possible to infer the fractal dimension from the experimental behaviour of the complex

scattering amplitude at $\theta = 0$.

On the other hand, the low-end of the spectrum ($q < 0.6 \mu\text{m}^{-1}$) is affected by Talbot oscillations like the ones shown in figures 4.9 and 4.10 (lower panels) which are related to the phase of the forward scattering amplitude, $\text{Arg } S(0)$. In order to retrieve this parameter, the following function is used for a least-square fit of experimental data:

$$T(q) = 1 + \cos\left(\frac{q^2}{k}\tilde{z} - 2 \text{Arg } S(0)\right) \cdot \text{sinc}\left(\frac{q^2 L}{2nk} + \varphi_0\right) \quad (4.9)$$

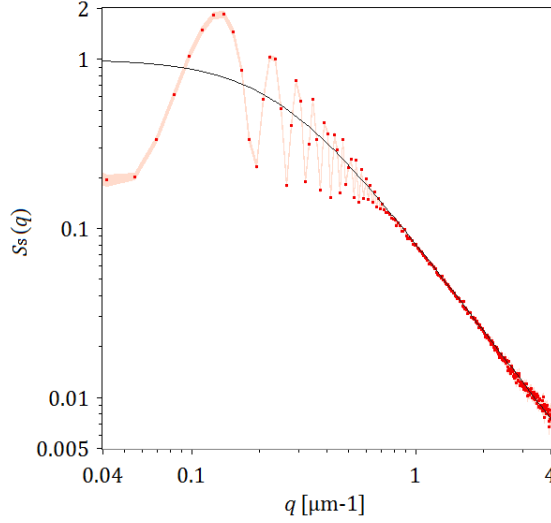
where k is the wavenumber of the incoming radiation, whereas \tilde{z} , L , and φ_0 are experimental parameters (see appendix B).

Notwithstanding the polydispersity of the aggregate population, the oscillations in the power spectra are well visible in each average. This suggests that $\text{Arg } S(0)$ is almost the same for all the aggregates present in the sample, since the oscillations would otherwise cancel out. A mild variability of the phase reflects in the slight discrepancies at low q values, $q < 0.1 \mu\text{m}^{-1}$, and results in a slight systematic over-estimation of $\text{Arg } S(0)$. As expected, measurements taken at several aggregation stages all gave consistently the same average phase of $S(0)$. For comparison, we report an overview of the main SPES results in the fourth column of table 4.1 (section 4.3). The results from NFS are in fair agreement with SPES : $\text{Arg } S(0) \simeq 0.09$ rad and $\text{Arg } S(0) \sim 0.16$ rad for 70 nm and 100 nm monomers, respectively (panels (b) in figures 4.9 and 4.10).

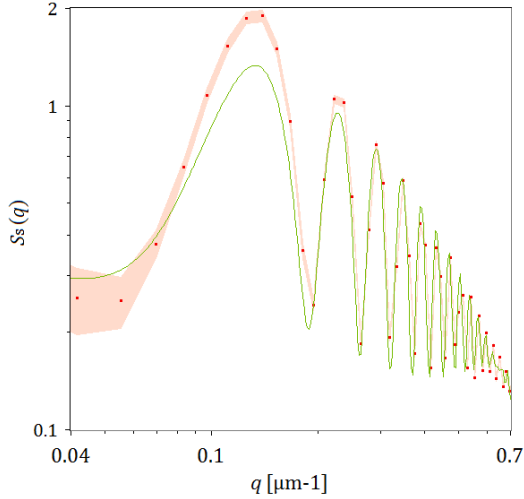
4.5 Simulations

The agreement between experimental data and the theoretical models is supported by many computer simulations based on the Discrete Dipole Approximation (DDA, see appendix C), which we present in this section.

Fractal structures were generated *in-silico* by using an algorithm similar to (Ringl and Urbassek, 2013, Brown et al., 2010). This procedure allows to easily grow aggregates with a tuneable compactness (i.e. the number density of monomers). Monomers were added randomly and sequentially at neighbouring positions to form chains, until the desired number of monomers in the aggregate was reached. A simple inter-particle repulsive potential can be tweaked in order to favour more extended or more compact conformations. In addition, such chains can be branched at any given site with a given probability ($p \sim 0.02 - 0.05$) at each step of the algorithm, which also impacts the ultimate compactness of the aggregate. The radius of gyration and the fractal dimension are evaluated with equations (4.2) and (4.1). Once the position of every primary particle was set, the scattering amplitudes were

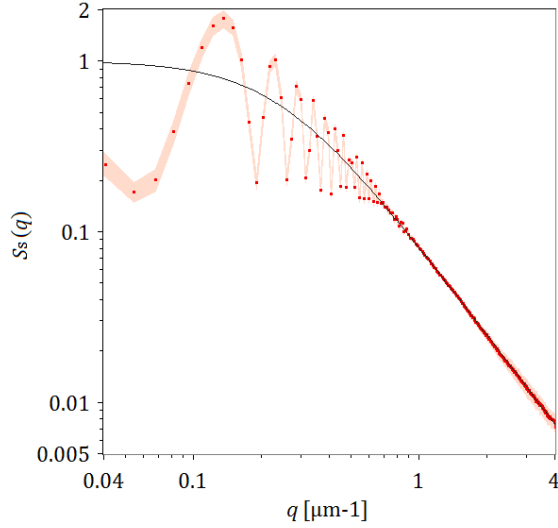


(a) NFS data from aggregates of polystyrene monomers 70 nm in diameter (red squares) after 45 minutes at room temperature. The pink area corresponds to the error bars. Fitting experimental data with the model (black solid line, equation 4.5) gives the slope of the spectrum at high q which is compatible with a fractal dimension $d_f = 1.75 \pm 0.01$.

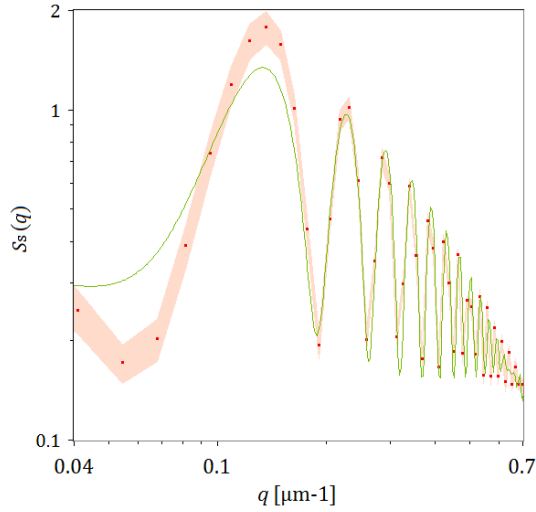


(b) Enlargement of panel (a) in the low- q region. Talbot-like oscillations are found up to $q \simeq 0.6 \mu\text{m}^{-1}$, which give the average phase of $S(0)$ for the polydisperse sample. The model in equation 4.9 is shown with a solid line (green). Several measurements give $\text{Arg } S(0) \simeq 0.09 \text{ rad}$ in fair agreement with SPES results.

Figure 4.9



(a) NFS data from aggregates of 100 nm polystyrene monomers (red squares) after 50 minutes at room temperature. The pink area corresponds to the error bars. A fit as in figure 4.9 (black solid line) gives the fractal dimension of the aggregates in the sample, $d_f = 1.76 \pm 0.01$.



(b) Detail of panel (a) in the low- q region as in figure 4.9. Measurements give $\text{Arg } S(0) \simeq 0.16 \text{ rad}$, in agreement with SPES results.

Figure 4.10

computed via the ADDA code (Yurkin and Hoekstra, 2011) averaging over different orientations for each particle (see appendix C).

Simulations showed that orientation has a negligible effect on the scattering amplitude of these particles at $\theta = 0$, thus averaging over ~ 20 orientations was enough to ensure a negligible standard deviation for $\theta \gg 0$. However, many more simulations were required in order to reduce the effect of the statistical conformations over the average structure factors (see figure 4.14).

Overall, we ran about $5 \cdot 10^4$ scattering simulations over twelve months, with masses ranging approximately between 50 and 5000 monomers, and R_g ranging between $0.3 \mu\text{m}$ and $6 \mu\text{m}$ ($a = 50 \text{ nm}$).

Simulations also allow the exact calculation of the corresponding gyration radii, R_g , for the set of N monomers that make up the aggregate. With this information, two additional counterparts were generated for each fractal aggregate: a cluster of non-overlapping monomers and a homogeneous spherical particle (see equations (4.10)). An example with $N = 1000$, $d_f = 1.75$ and $k_0 = 1.2$ is given in figure 4.11. The first consists in randomly distributing the same number of monomers, N , within a sphere of radius R_g , thus breaking almost all the links (correlations) in the monomer chains of the corresponding fractal aggregate. The only constraint in this configuration is that the monomers must be non-overlapping, which introduces a certain degree of anti-correlation. The simulated scattering results were averaged over ten different conformations of such particles.

The second consists in approximating the aggregate with a homogeneous sphere of radius R_g (Sorensen (2001)), whose refractive index is set according to the Maxwell-Garnett model. To this purpose, the volume fraction is evaluated by $f = N \cdot R_g^3 / a^3$. In figure 4.11 are shown the normalised structure factors corresponding to these three kinds of particles. Their expressions are, respectively:

$$S_s(q)_{\text{fractal}} = \frac{1}{N} + {}_1F_1\left(\frac{3-d_f}{2}, \frac{3}{2}; \frac{(qR_g)^2}{d_f}\right) e^{-(qR_g)^2/d_f} \quad (4.10a)$$

$$S_s(q)_{\text{cluster}} = \frac{1}{N} + P(qR_g) \quad (4.10b)$$

$$S_s(q)_{\text{sphere}} = P(qR_g) \quad (4.10c)$$

where $P(qR_g)$ is the form factor defined in equation (2.8). The term $\frac{1}{N}$ corresponds to the excluded volume condition on the positions of the centres of the monomers; monomers are otherwise uncorrelated in the clusters. According to the equations (4.10), this term is what differentiates a homogeneous spherical particle from a cluster of uncorrelated monomers (see the plots in figure 4.11). The same excluded volume term is also present in the formula relating to fractal aggregates, but in most cases is negligible since $N \gg 1$.

The real and imaginary part of the forward scattering amplitude are calculated by means of the molecular optics model given in equations (2.62) in all three cases, substituting the proper structure factor. As discussed in section 4.5, the model in equations (2.62) can be adopted for all three kinds of particles. The corresponding

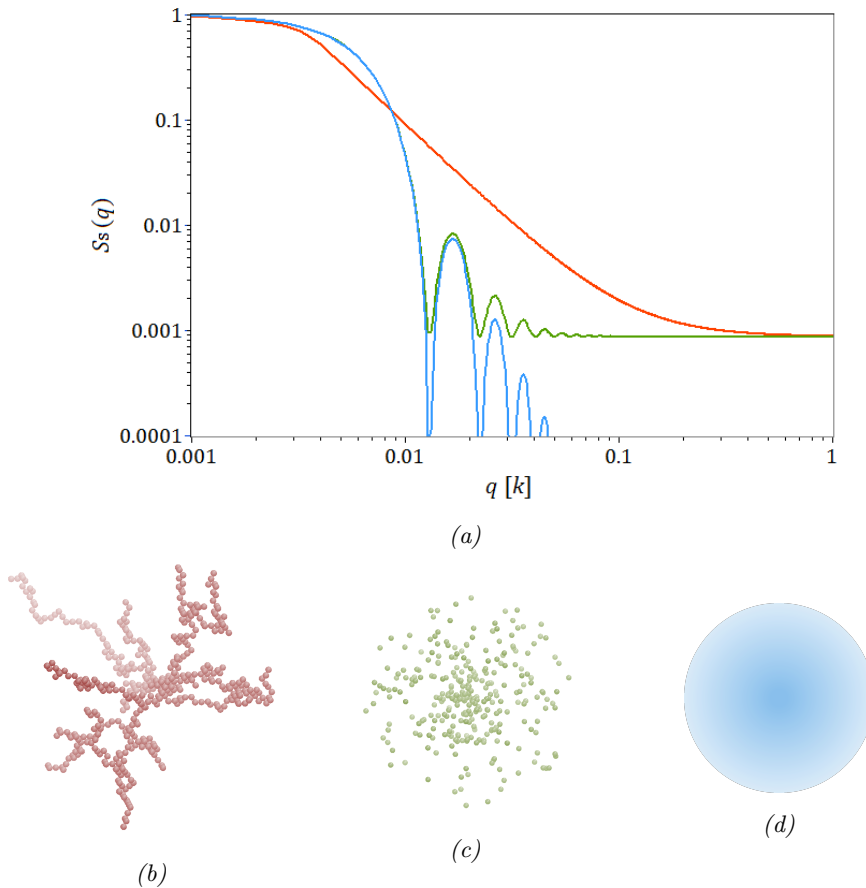


Figure 4.11: Particles with different morphologies used for the simulations reported in figures 4.12 and 4.13 (here $N = 11500$, $d_f = 1.75$ and $k_0 = 1.2$). (a) Structure factors used in the scattering theoretical model, the colours of the curves are corresponding to the morphologies shown in the panels below. Notice the change in the slope at $q \sim k = 10 \mu\text{m}^{-1}$ of the red curve due to the excluded volume contribution. The contribution of this is much more evident for uncorrelated clusters (green solid line) (b) representation of a simulated fractal aggregate; (c) uncorrelated cluster; (d) Maxwell-Garnett equivalent sphere.

scattering amplitudes are reported as orange, green and blue squares in figure

4.12, without any free parameter. Experimental data compares quite nicely with simulations relating to fractal aggregates (orange squares) with fractal dimension $d_f = 1.75$, $k_0 = 1.20$ and ranging number of monomers, N . We also report the scattering amplitudes predicted by the model where the monomers are randomly distributed within a sphere of radius R_g (green squares in figure 4.12). Finally, the curve predicted by the Maxwell-Garnett model is shown as a blue line together with simulations.

Similar simulations have been carried out with monomers 70 nm in diameter with analogous results that are reported in figure 4.13. The comparison of simulations

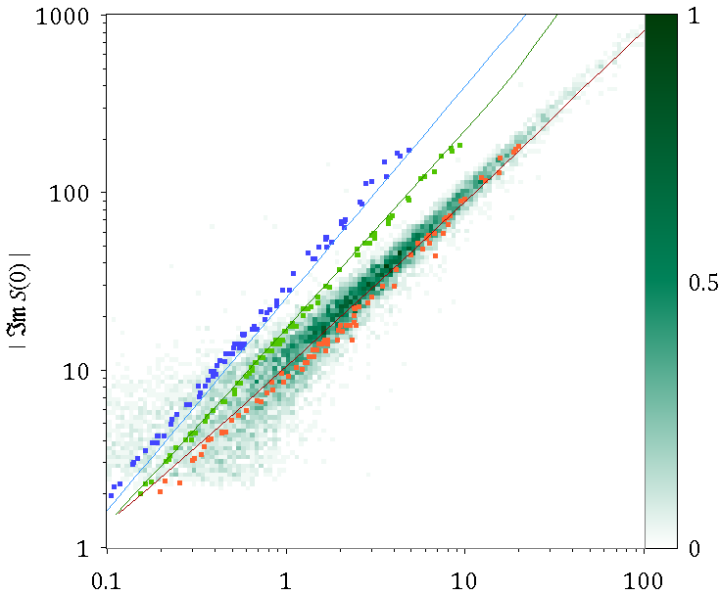


Figure 4.12: Experimental behaviour of $|\Im S(0)|$ as a function of $\Re S(0)$ from SPES measurements for aggregates obtained from monomers 100 nm in diameter. The two-dimensional histogram agrees with both the theoretical behaviour predicted by equations (2.62) ($a = 0.05 \mu\text{m}$, $d_f = 1.75$, $k_0 = 1.20$, solid orange line) and with simulations (orange squares) resulting from fractal structures generated as described in the text. Simulations of uncorrelated clusters and Maxwell-Garnett equivalent spheres are reported as green and blue squares respectively, whereas each corresponding theoretical model is shown with a solid line of the same colour.

to the corresponding models suggests that the imaginary part of the scattering amplitude is minimally affected by correlations. Moreover, homogeneous spheres, uncorrelated clusters and fractal aggregates all give $|\Im S(0)| \sim Nk^3\alpha$, where α is the polarizability of one monomer and N is the number of monomers in the

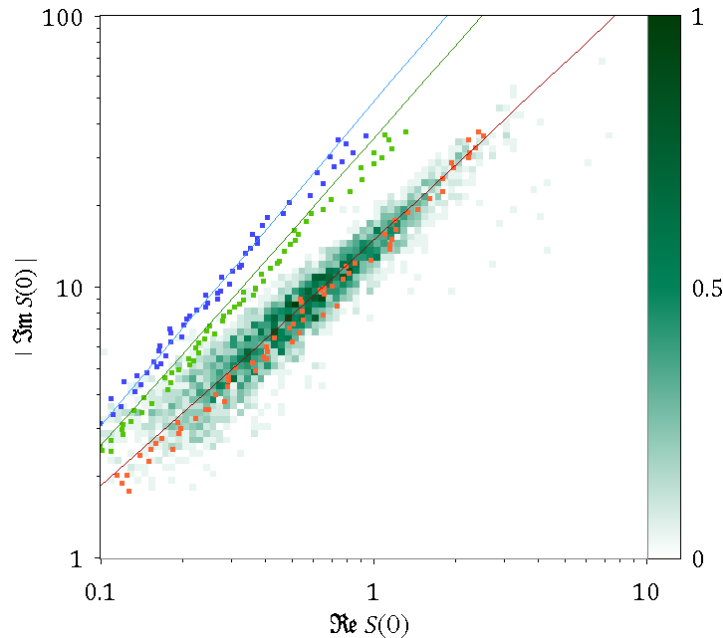


Figure 4.13: Same as in figure 4.12 with aggregates of 70 nm polystyrene sulphonate spheres.

aggregate. Since $|\text{Im}S(0)| \gg \text{Re}S(0)$, the mutual positions of the monomers inside the aggregate and its orientation have a limited impact on scattering. To this extent, the monomers can be treated as coherent emitters: we observe that the N monomers inside the aggregate yield

$$|S(0)| = N|s_0(0)| \quad (4.11)$$

where $s_0(0)$ is the modulus of the scattering amplitude in the forward direction of a single monomer. An implication of this is that the number of particles N can be, at first order, retrieved by the modulus of the scattering amplitude, if the monomers are known. This agrees with the RDG model.

Cross-checks verified that numerical simulations correctly describe light scattering by fractal aggregates, by recovering the structure factors experimentally: once compared to both the theoretical model and the experimental NFS results the agreement is very good. We note that the structure factor of such structures in figures 4.14 and 4.15 is well described by the approximation (4.5) for $qR_g \gg 1$.

We checked the fractal dimension according to equation (4.2) by counting the number of monomers inside a sphere of increasing radius centred on the centre of mass, for a given k_0 . This gives an estimate of the density of the aggregates and

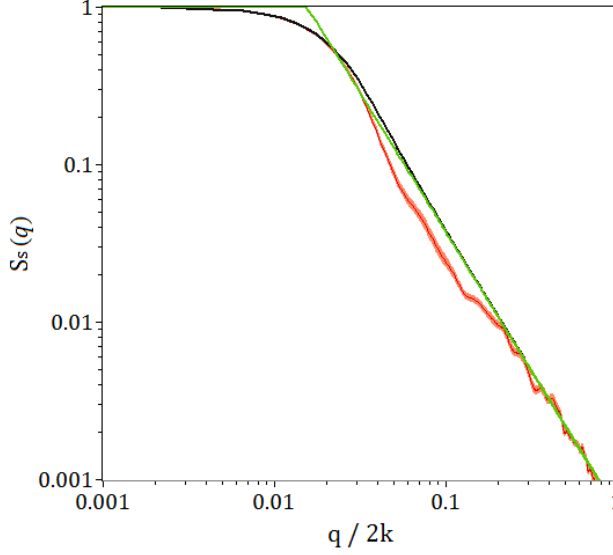


Figure 4.14: Log-log plot of the average spectrum of the particle in figure 4.4, normalised on its maximum occurring at $q = 0$ ($N = 1150$, $R_g = 2.45 \mu\text{m}$ and $d_f = 1.76$). The average is taken over 100 different orientations of the same particle (red solid line). The vertical width of the red curve corresponds to the error bars. The curve is compared to the RDG formula (4.6) (black solid line), and with the approximation in equation (4.5) represented as a green solid line. The slope at large q values gives $d_f = 1.76$. With the exception of the low- q region close to the roll off, the two models are essentially equivalent.

allows to check the value of the prefactor, which was found to be $k_0 \sim 1.2$, in agreement with typical values reported in literature (Gmachowski, 2002, Lattuada et al., 2003, Heinson et al., 2012).

Similarly, the power spectra of the resulting structures are calculated via the ADDA discrete dipole approximation code, which can be directly related to the structure factors.

As an example, in figure 4.14 we show the calculated $S(q)$ of a particle with $N = 1150$, $R_g = 2.45 \mu\text{m}$ and $d_f = 1.76$. The size of the particle is in good agreement with the Guinier approximation in the low q limit of the spectrum, $qR_g \lesssim 1$, $S(q) \sim 1 - (qR_g)^{2/3}$. The overall trend of the spectrum agrees with both the RDG formula (equation (4.6)) and the approximation in equation (2.62). However, since this curve refers to a particular conformation, the high q end of the spectrum is affected by the fine structure of the aggregate, as it can be noticed from the discrepancy up to around $q/2k = 0.2$ between the simulation and the model. To overcome

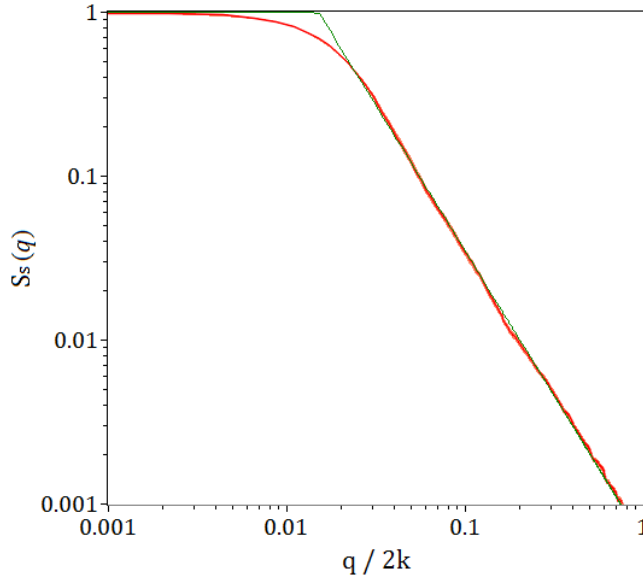


Figure 4.15: Average of 700 normalised structure factors (red solid line) of fractal aggregates with $N = 1150$, $R_g = 2.45 \mu\text{m}$ and $d_f = 1.76$. The average is taken over both random orientations and statistical conformations, and it superimposes perfectly with the RDG approximation (not reported). The vertical width of the red curve corresponds to the error bars. The curve is compared to the approximation in equation (4.5) represented as a green solid line. The slope agrees with $d_f = 1.76$.

this variability, several randomly oriented particles with the same parameters N , R_g and a were generated to increase the sampling of conformations. The fractal dimension, d_f , was checked against the trend of the resulting average (figure 4.15). Such value of $d_f = 1.76 \pm 0.02$ is in agreement with the slope of the structure factor in equation (4.5). The reader might refer to figures 4.10 and 4.9 in section 4.4 for a comparison with experimental data.

Conclusions

The purpose of this thesis was to determine the effects of shape and structure on radiative properties of non-absorbing particles, going beyond the common spherical approximation in interpreting the experimental results.

In collaboration with the EuroCold research group (Università degli Studi di Milano-Bicocca), we applied the SPES method to mineral dust from deep Antarctic ice core samples (Vostok, Dome C and Dome B) and alpine samples (chapter 3). The effect of particle shape on the extinction cross section and optical depth of micrometric particles was investigated on Alpine samples (Rutor, Dent du Géant) and on Greenlandic RECAP ice core samples in collaboration with Dr. Marius F. Simonsen from the Center for Ice and Climate research group in Copenhagen. In this investigation, the forward scattered fields of particles in Holocene and Glacial samples were measured in the clean room of the EuroCold laboratories in Milan. A specifically designed sample circulation system allowed to impose orientation constraints on the flowing particles. Combining SPES data with an extensive database of simulations based on the Discrete Dipole Approximation, it was possible to estimate the aspect ratio of the particles, which was found to vary considerably among different sites. As a matter of fact, there is a known discrepancy between the results obtained from two widely used commercial instruments for particle sizing, namely the Coulter Counter and the Optical Particle Counter. This was found to be due to the orientation of non-spherical particles with respect to the laser beam. A protocol for characterising the aspect ratio from this discrepancy was developed, which agreed with the estimates given independently from SPES data, as well as from microscopy images.

The research on samples from Dome C was focused on particle aggregates formed in situ in deep ice cores. We especially developed for the purpose an experimental protocol whereby it was possible to distinguish compact particles from aggregates of smaller particles. This is a known issue affecting paleoclimate research by altering the pristine size distribution of mineral dust in ice cores. Thanks to the

single particle approach, this was achieved throughout the whole size range of the population, while simultaneously measuring the optical thickness of each particle. In the attempt to invert scattering data by means of a spherical approximation, one obtains a refractive index which is not compatible with any known mineral in sample, indicating that the sample cannot be interpreted as a population of compact particles.

A thorough characterisation of colloidal fractal aggregates was carried out (chapter 4). These particles are very well characterised in literature and served as a benchmark for testing the effect of the internal structure of a particle on its radiative properties. Specifically, such particles have a well-known structure factor and are easily reproducible, in addition to being a model for many aggregation processes. By the Single Particle Extinction and Scattering (SPES) method we measured the complex scattering amplitude in the forward direction, $S(0)$, without any free parameter or calibration. Quantitative evidence of the effects given by correlations among the fields radiated by each monomer inside a fractal aggregate was provided. It was also possible to test the most common theoretical models with very few free parameters, i.e. the Rayleigh–Debye–Gans (RDG) and Effective Medium Approximations.

It was found that the RDG approximation can effectively be used to predict the scattering parameters from aggregate particles, including their complex scattering amplitude, $S(0)$. Conversely, it was established that the Maxwell-Garnett approximation cannot be applied to fractal aggregates, notwithstanding their low density. Specifically, it was found that the expected extinction cross section is lower than the measured one by a factor of ~ 2 on average, up to ~ 3 for the largest particles. This affects any attempt to invert experimental scattering data. For example, in the present case the size of the particles would have been overestimated by a factor of ~ 1.5 . Due to the overlook of correlations, such approximation gives an inaccurate prediction for the phase of the forward scattered field, as is clear from experimental data. These results were also supported by numerical calculations.

The single particle approach followed in this thesis ensured results that are not affected by polydispersity, allowing for a thorough study of the samples while avoiding the complexity of inverting the collective response of the whole particle population. Optical parameters are accessed directly, and results are model-independent.

By a dedicated theoretical model it was possible to determine both the fundamental parameters in fractal morphology (the prefactor, k_0 and the fractal dimension, d_f) by combining SPES and Near Field Scattering measurements. Such independent perturbative model (outlined in section 2.5) was developed by Professor Alberto Parola from Insubria University in Como, with whom we collaborated. A particular attention was devoted to the structure of the aggregate and to the intercoupling

of the dipoles it comprises by including explicitly both the structure factor and the form factor. With this theoretical tool we were able to support the experimental findings while providing an independent proof that the RDG model satisfies the optical theorem.

The model also explained why correlation effects are hidden in traditional experiments measuring the intensity of the scattered field. In non absorbing sparse particles, $\Im S(0)$ is shown to be dominated by the term $\sim N\alpha k^3$ in agreement with RDG scattering. On the other hand, data from our samples give $\Re S(0) \ll \Im S(0)$ as expected according to the theoretical model and simulations. The modulus of the scattering amplitude is weakly affected by the term due to the internal structure of the scatterer, for example correlations between its constituents. On the other hand, these dramatically affect $\Re S(0)$. This is proportional to the extinction cross section, which is then the parameter mainly affected by correlations. Nonetheless, the simultaneous measurement of both the forward complex field components is essential to separate their contribution.

The effect of shape, structure and correlations can go beyond the detailed study of the forward scattered fields of the particles we chose to investigate. Many experimental methods adopted for sizing and analysis of nanoparticles, dust and fine powders, in fact, rely on simplified assumptions about the scattering properties of the unknown measured objects, typically interpreted in terms of homogeneous spheres (Mie inversion). Moreover, global radiative forcing models showed to be very sensitive to the shape of the particles. With rare exceptions, particles have a highly non-spherical morphology and are often aggregates or agglomerates of many building blocks, especially at the smallest sizes. Optical properties of nano- and micro-metric particles such as scattering and absorption cross sections and optical thickness exhibit a significant dependence upon the size, geometrical structure and composition of the particle. A main issue emerging from this study is that exact Mie calculations predict rather peculiar behaviours that hardly lend themselves to generalisation, especially as regards the angular dependence of scattering. This is significant in many fields of research, as in the characterisation of radiative transfer processes, aerosol composition and influence upon climate and astrophysics.

To conclude, we list a few projects that could be set up as an interesting progression of the present work.

A systematic study on airborne particles. The experimental results reported throughout this thesis deal with particles suspended in water, which is the optimal configuration for colloidal and melted ice core samples. However, the method used to characterise such samples has been recently adapted to be fully operational in measuring particles in the atmosphere⁹. Moreover, the in-

⁹The instrument was loaded onto a small hot air balloon to measure the lower layers of the

strument currently hosts two additional sensors at 45° and 90° , and is currently being used to measure particles in Concordia Research Station in Antarctica and in northern Italy urban sites. A much more complete characterisation of airborne particles can be achieved in situ, also with regard to the differential scattering cross section (phase function). An analysis of data collected over several months by two identical SPES instruments in Antarctica and in Milan is being carried out¹⁰.

Addressing the case of absorbing particles. The independent scatterers approximation is commonly accepted also in case of absorbing particles (e.g., see Sorensen et al., 2018). This assumes that the total absorption cross section of an aggregate of N identical particles is simply N times the absorption cross-section of its constituents. For example, absorption and scattering by soot is considered to follow the RDG model for fractal aggregates. Such particles have been shown to have a dramatic impact on climate due to their strong interaction with solar and terrestrial radiation. In view of the results outlined previously, further inspection on the critical aspects of morphology impacting absorption and scattering would be valuable. moreover, this would be a requirement for applying the SPES method to atmosphere monitoring, given the abundance of absorbing particles.

Expanding on the molecular optics model. The model presented in section 2.5 may be adapted to the case of non-spherical, compact particles capturing the features of mineral dust. To this end, an average (effective) structure factor might be produced from an orientational average. The variability of scattering upon orientation (as detailed in Chapter 3) may be formally linked to the spread of the optical thickness distribution within this theoretical framework. This would be a fruitful area for further research, with a view to providing more quantitative constraints on the morphological parameters of the particles. This may include improving the protocol for inverting the aspect ratio of mineral dust from multiparametric measurements.

atmosphere (planetary boundary layer) in Aosta. We refer to Cremonesi et al. (2019) for a technical description of the instrument.

¹⁰The preliminary results are currently under analysis and they could not be included in this thesis.

Publications

- i) Potenza, M. A. C., Cremonesi, L., Delmonte, B., Sanvito, T., Paroli, B., Pullia, A., Baccolo, G., and Maggi, V. (2017). Single-particle extinction and scattering method allows for detection and characterization of aggregates of aeolian dust grains in ice cores. *ACS Earth and Space Chemistry*, 1(5): 261.
- ii) Potenza, Marco A. C., Nazzari, D., Cremonesi, L., Denti, I., and Milani, P. (2017). Hyperspectral imaging with deformable gratings fabricated with metal-elastomer nanocomposites. *Review of Scientific Instruments*, 88(11): 113105.
- iii) Simonsen, M. F., Cremonesi, L., Baccolo, G., Bosch, S., Delmonte, B., Erhardt, T., Kjær, H. A., Potenza, M. A. C., Svensson, A., and Vallenga, P. (2018). Particle shape accounts for instrumental discrepancy in ice core dust size distributions. *Climate of the Past*, 14(5): 601.
- iv) Ceratti, D. R., Rakita, Y., Cremonesi, L., Tenne, R., Kalchenko, V., Elbaum, M., Oron, D., Potenza, M. A. C., Hodes, G., and Cahen, D. (2018). Self-healing inside Abbr3 halide perovskite crystals. *Advanced Materials*, 30(10): 1706273.
- v) Minnai, C., Cremonesi, L., Milani, P., and Potenza, M. A. C. (2019). A very simple scheme for spectrally resolved imaging by means of curved polymeric gratings. *Materials Research Express*, 6(6): 065044.
- vi) Cremonesi, L., Passerini, A., Tettamanti, A., Paroli, B., Delmonte, B., Albani, S., Cavaliere, F., Viganò, D., Bettega, G., Sanvito, T., Pullia, A., and Potenza, M. A. C. Multiparametric optical characterization of airborne dust with single particle extinction and scattering. *Accepted by Aerosol Science and Technology* (Dec 2019).

Appendices

APPENDIX A

Single Particle Extinction and Scattering

Single Particle Extinction and Scattering (SPES) is an optical method based on a self-reference interferometric scheme where the zero-angle field scattered by one particle passing through a focused laser beam is superimposed to the transmitted field used to probe the sample (Potenza et al., 2015c,a). It provides two independent parameters directly related to the real and imaginary part of the forward scattering amplitude, $\Re S(0)$ and $\Im S(0)$, from single particles suspended in a fluid, as opposed to statistical approaches measuring many particles in the sample at the same time. More importantly, the measurement of these two parameters is simultaneous, therefore with the same particle orientation and illumination conditions.

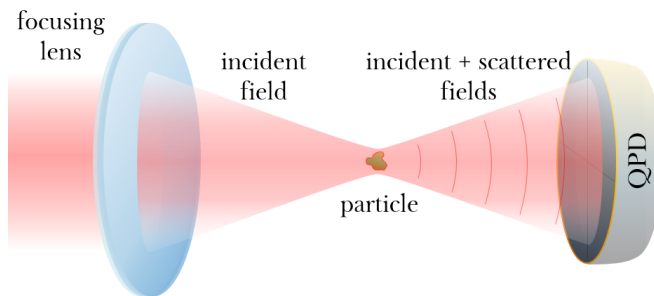


Figure A.1: Sketch of the main part of the SPES optical setup. A lens focuses a collimated Gaussian beam to a diameter of some micrometres, the field scattered by any particle in the focus of the beam is collected by a four quadrant photodiode. The layout gives space for additional sensors at $\theta = 45^\circ$ and $\theta = 90^\circ$ as in the latest versions of the instrument.

The method is based on a very simple optical layout. A laser beam about 0.8 mm in width (ULN Lablaser 5 mW, 635 nm, Coherent ltd) is expanded with an objective, spatially filtered, and collimated with a lens. An additional lens focuses the beam and guarantees an almost Gaussian field profile with a beam waist of 15 μm .

The beam waist can be adjusted with a proper choice of the focal lengths of these optical components. We show the main part of the optical setup in figure A.1). The sample is driven through the focal region, the effective scattering volume of the instrument; an appropriate low-concentration of the samples ensures that the presence of more than one particle is an exceptional occurrence.

In the far-field, downstream of the beam waist, the faint field scattered in the forward direction by the particle and the intense transmitted beam interfere on a segmented sensor, a four quadrant photodiode (QPD), as shown in figure A.1. The beam is almost unaffected by the presence of the particle, so that almost no power is removed from it. This also allows to rely on a continuous monitoring of the light intensity: the system does not need any calibration.

Since the intensity distribution changes homotetically with the focus-sensor distance, the sensor can be placed along the optical axis at any distance from the focus, provided that the whole beam is collected. A limited number of elements (four) in the sensor is enough for this technique, while allowing for a high detection rate. Low-noise current preamplifiers split the current from each quadrant into the intense constant signal that gives the power of the beam, and the fast zero-averaged signals proportional to the power fluctuations introduced by a particle disturbing the beam. The currents are transformed into amplified voltage signals and sent to a USB oscilloscope to be digitalized at ~ 1 MHz sampling frequency, much higher than any characteristic frequency of the signals.

The sensor provides a differential, calibration-free measurement of the intensity modulations due to interference. These can be traced back to the real and imaginary part of the forward scattering amplitude, $S(0)$. The only instrumental parameter to be determined is the beam waist, which affects the modulus of the forward scattering amplitude but not $\Re S(0)$ and $\Im S(0)$ individually.

A differential measure of the intensities at opposite quadrants of the sensor allows to quantitatively assess if the particle is placed symmetrically with respect to the laser beam and the direction of the flow (Potenza et al., 2015c). The data analysis proceeds with fitting simple algebraic combinations of these signals with smooth functions. A flexible accept-reject routine is implemented in addition to custom trigger settings.

Sample circulation system

The sample circulation system is connected through a fluorinated ethylene propylene tube to a commercial quartz flow cell (Hellma 170.700-QS) - 0.2 mm thick and 3.5 mm wide - where the sample is intersected by a tightly focused laser beam¹.

¹Alternatively, a larger 1.5 mm \times 1.5 mm cell is used to lower the shear stress.

The setup for driving the particles are driven by a uniform, laminar flow at a constant speed can be adapted according to specific needs. For example, either a flow cell or a system of nozzles can be used, depending on whether the sample is gaseous or liquid.

Measurements on extremely low-concentrated samples like particles in melted ice-core sections require to be sheltered from the laboratory environment (a clean room). The particles are driven through the system by means of a closed, electronically controlled intake mechanism with adjustable flow rate. This device lowers the pressure alternatively at the ends of the line with a pair of syringes, causing the suspension to flow back and forth many times at a constant speed. The typical flow rate adopted for such measurements (some mL min^{-1}) makes this method suitable to operate in continuous flow analysis systems. The requirements on the flow rate depend on both the scattering volume and the geometry of the flow cell.

More fragile particles as the fractal aggregates of section 4.2 are subject to a more delicate treatment by letting them pour freely from a container. The experimental setup comprises a container where the sample to be measured is kept at atmospheric pressure some centimetres above the cell. Downstream, the sample is driven to another container that serves as a drain.

The system described above refers to liquid suspensions which are the scope of the present work. Aerosols require a dedicated circulation system which also replaces the flow cell. In brief, the setup must include a suction compressor with which a thin air flow is generated between two nozzles, placed immediately above below the focal region. The main difference of this layout compared to the instrument dedicated to liquid samples is the general higher sensitivity to noise, counterbalanced by a wider sensitivity window due to the higher jump of the refractive index of the particles with respect to the surrounding medium.

Application examples

The instrument design can be specialised to measure particles suspended in either water or air. It has been extensively employed on both liquid samples and in air monitoring campaigns (Mariani et al., 2017, Potenza et al., 2017a, Cremonesi et al., 2019).

Size and refractive index can be accurately obtained for single particles endowed with spherical or isometric shape. More insight on the morphology of the particles can be obtained through statistical analysis of the population by taking advantage of polydispersity or orientation variability (Potenza et al., 2015b, Villa et al., 2016), as seen in sections 3.3, 3.4 and 4.3 of the present thesis.

According to Mie theory, monodisperse suspensions of spherical particles yield narrow peaks in the complex $S(0)$ plane. In figure A.2 are shown the results for colloidal suspensions of polymeric beads, namely polystyrene (PS) and polymethylmethacrylate (PMMA) spheres of several diameters. The experimental data are compared to ADDA calculations (see appendix C). Since the refractive index of PS, $m = 1.59$ is higher than the refractive index of PMMA, $m = 1.49$ the corresponding peaks are located lower on the plane, accordingly to Mie calculations (yellow and orange solid lines). Thanks to the simultaneous measurement of two parameters, it is possible to distinguish the refractive index of the spheres. For example, measuring only extinction would lead to the superposition of the signals from PS $0.75\text{ }\mu\text{m}$ and PMMA $1\text{ }\mu\text{m}$ particles.

The outstanding evidence of polydispersity is a variability in the modulus of the forward scattering amplitude, $-S(0)-$. As an example, a two dimensional histogram of SPES data from a sample containing ceria nanoparticles is shown in figure A.3, taken from Potenza et al. (2015b). In this case, the isometric (almost spherical) shape of the particles yields a thin distribution along the vertical axis in agreement with Mie theory, while the main elongation is due to the sample polydispersity. Inversion is straightforward by setting the refractive index $n = 1.95$, which gives a diameter distribution ranging from 120 nm to 400 nm .

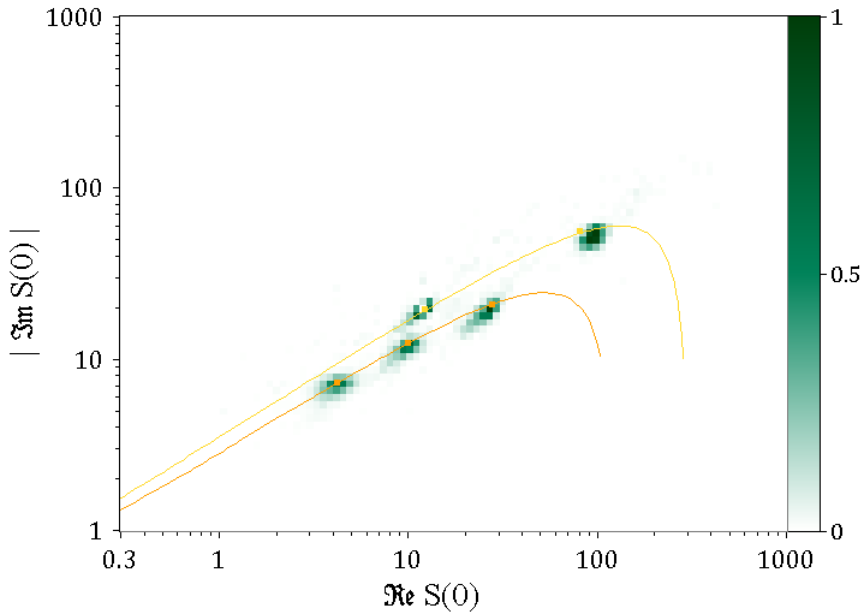


Figure A.2: SPES data relating to calibrated spherical polymeric particles displayed on a two dimensional histogram. The spheres were suspended in pure filtered water. Left to right: PS 0.6 μm in diameter, PS 0.75 μm , PMMA 1 μm , PS 1 μm and PMMA 1.7 μm and Yellow and orange dots are the corresponding numerical calculations by the ADDA code (see appendix C). For reference, yellow and orange solid lines represent Mie calculations for spheres 1.49 and 1.59 in refractive index, respectively. notice the separation due to the difference in refractive index.

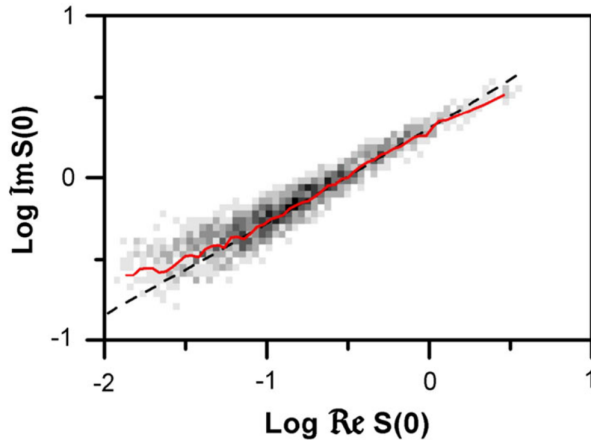


Figure A.3: Experimental data for polydisperse ceria nanoparticles represented as a two-dimensional histogram $\text{Im}S(0)$ vs $\text{Re}S(0)$. Grey tones indicate the number of particles within each two-dimensional bin, normalised to the maximum value (black). The main elongation is due to polydispersity, while the vertical-wise thin distribution is attributable to the isometric shape of the particles. The red solid line is the mode of the distribution, evaluated in the vertical direction. The dashed line corresponds to a population of spherical particles which best fits the experimental data distribution, namely $n = 1.95$. From Potenza et al. (2015b)

APPENDIX B

Near Field Scattering on flowing samples

We devote this appendix to outline an optical technique based on Near Field Scattering (NFS) for characterising colloidal samples under constant flow, which we adopted to obtain the results on colloidal fractal aggregates discussed in section 4.4.

In summary, it measures the speckle field due to the interference of the faint light emerging from a random distribution of scattering centres (the sample) and the intense, almost undisturbed transmitted beam. This speckle field contains information on the density correlation function of the scatterers in the sample (Magatti et al., 2008). Among the advantages of Near Field Scattering we enumerate its stability and simple optical layout (Mazzoni et al., 2013).

A range of scattering angles close to $\theta = 0$ can be recorded simultaneously, while the stray light affecting measurements can be subtracted during data processing. A dedicated data processing further reduces the need of optical stability to time intervals of the order of the time lapse between two acquisitions. In practice, a time stability of up to a few seconds is enough. As with the SPES set-up described in appendix A, the design of the instrument makes this technique suitable to be included in Continuous Flow Analysis systems.

Commonly, the exposure time must be short with respect to any change in the speckle pattern to prevent blurring, whereas the time lag between two subsequent acquisitions must be long enough to allow a change in the positions of the scattering centres so that the speckle patterns are uncorrelated (Ferri et al., 2004). The instrument outlined here is able to effectively overcome these limitations and can be operated on flowing samples, still maintaining the basic approach and advantages of the NFS method.

The optical layout is shown in figure B.1. A He-Ne Gaussian beam (632.8 nm wavelength, 5 mW power, 0.5 mm beam waist) is spatially filtered, expanded and collimated through an achromatic doublet 50 mm in focal length. The beam is then focused by a cylindrical lens (80 mm focal length), with the optical power in the vertical direction. Specifically, the focal line is orthogonal to the sample flow and has a major semi-axis of 5 mm (horizontal) and minor semi-axis of 10 μ m

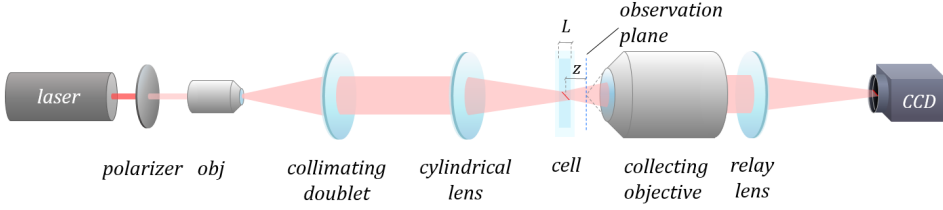


Figure B.1: Schematic of the optical layout. A He-Ne laser (632.8 nm) beam is spatially filtered and expanded through a 20 \times objective and a collimating doublet. A cylindrical lens focuses the beam in the vertical direction at the centre of a flow cell. The emerging light is collected at a distance $z = 10$ mm by a microscope objective and a relay lens forms a magnified image onto a CCD sensor.

(vertical). The focal line is placed at the centre of a plane parallel quartz flow-cell (Hellma 170.700-Qs, 200 μ m optical path) through which the sample is driven in a controlled manner.

Since the sample thickness is lower than the Rayleigh range of the focal line, all the scattering centres are illuminated by plane waves, hence the scattered fields are emitted as spherical waves. 10 mm downstream the sample, the transmitted beam and the scattered wave-fronts are collected in the observation plane, placed much further than the Rayleigh range. This guarantees both the far-field condition in the vertical direction and the deep Fresnel condition (near-field) for the horizontal direction. Finally, the collection optics is composed by an afocal, long distance microscope objective (Edmund Optics 59878, 20 \times) and a field lens to magnify 10 \times the observation plane onto the sensor surface. A digital CCD camera recording a region of interest 1048 \times 16 pixels at a rate of 100 frames/s was used. Signal noise (mainly shot noise) can be reduced by averaging the pixel values along the vertical direction.

The sample is driven through the light beam under laminar flow to match the conditions of the SPES measurements reported in this work. This also guarantees a fast refresh of the entire speckle field.

By strongly reducing the extension of the illuminated region along the flow direction, the renewal of speckle field can be optimised. The vertical extension of the focal line, in fact, sets the minimum time lag between two subsequent acquisitions, i.e. the minimum time required for all the scattering centres to move out of the illuminated region. In a traditional NFS configuration, this would introduce substantial motion blurring, cancelling out part the speckle pattern. The low-power laser (5 mW) prevents this issue by simply reducing the exposure time without undermining the dynamics of the images. The motion blurring is overcome by transilluminating the cell by a highly astigmatic laser beam.

From an optical point of view, this introduces a substantial increase in terms of system sensitivity, especially when measuring faint scattered fields as in very diluted samples. The focal line intensity is appreciably larger than the intensity of the beam at the sensor plane, which increases the amplitude of the scattered waves. The contrast of the interference pattern is then proportionally enhanced.

The constant flow is obtained by draining the sample from a container at normal pressure, as in Alaimo et al. (2006) and in the SPES measurements of chapter 4.3. A 1 mm internal diameter tube delivers the liquid to the flow-cell. A flux of $\sim 0.7 \text{ mL min}^{-1}$ provides a speed of $\sim 20 \text{ mm s}^{-1}$ at the centre of the cell, i.e. at the maximum speed of the Poiseuille flow. With the chosen width of the focal line, the time required to renew the sample into the illuminated region shortens down to approximately 1 ms.

Let us refer to the observation plane, the sensor being just collecting light intensity which is magnified by the microscope objective. We will also limit our considerations to a limited extension in the vertical direction of the observation plane. This is particularly useful especially from an experimental point of view, since a sensor with limited vertical extension does take huge advantage in terms of the acquisition speed (the number of pixels to be read is much less than in the traditional NFS). Notice that the focal line illuminates only particles within a thin region elongated in the horizontal direction, orthogonal to the optical axis.

Let us consider an astigmatic laser beam of wavelength λ focused in the y direction (i.e. vertical direction) by a cylindrical lens of focal length f . In the Gaussian beam approximation, the vertical extension of the beam at the focal line and at the observation plane at a distance z are, respectively:

$$w_0 = \frac{\lambda f}{\pi w}; w(z) = w_0 \sqrt{1 + \left(\frac{z}{z_R}\right)^2} \quad (\text{B.1})$$

where we use the usual definition of the Rayleigh range in a medium with refractive index n :

$$z_R = \frac{\pi w_0^2}{\lambda} n \quad (\text{B.2})$$

By using the properties of a Gaussian beam, the field amplitude impinging onto the particles within the focal line ($|y| < w_0$ and $|z| < z_R$; $k = 2\pi/\lambda$) is:

$$E_0 = \sqrt{\frac{w}{w_0}} e^{i(kz - \frac{1}{2} \arctan(z/z_R))} \quad (\text{B.3})$$

On the sensor plane, where we assume $z \gg z_R$ and $y = 0$, we obtain the reference field amplitude:

$$E_R = \sqrt{\frac{w}{w(z)}} e^{i(kz - \frac{\pi}{4})} \quad (\text{B.4})$$

Without entering into details, we just notice that the superposition of the reference field B.4 and the field scattered by objects illuminated by the field B.3 will generate an intensity distribution of the form:

$$I(x) = \left| 1 + \sqrt{\frac{w(z)}{w_0}} \sum \text{spherical waves} \right|^2 \quad (\text{B.5})$$

The prefactor of the interference term shows the enhancement of the contrast mentioned above. By introducing the formal expressions for the spherical waves emerging from N identical scattering centres within the focal line, and with some mathematics, one finds that the power spectrum of the intensity distribution $I(x)$ provides the static form factor multiplied by the enhancing term and the *Talbot* transfer function, T , typical of deep Fresnel speckles (see below):

$$P(\cos\theta) = \frac{|S(\cos\theta)|^2}{k_0^2} N \frac{\pi w^2}{f^2} T \quad (\text{B.6})$$

where S represents the dimensionless amplitude of the field scattered at angle θ . Following the approaches described in Ferri et al. (2004), Mazzoni et al. (2013), Potenza et al. (2010a), the self-reference interferometric scheme gives independent information about both the static form factor from the spatial power spectrum of the NFS speckles (equation B.6) and the phase lag of the scattered waves from the Talbot oscillations (Van de Hulst, 1981). The optical layout described here gives access to the power spectrum up to $q \sim 4 \mu\text{m}^{-1}$, corresponding to a scattering angle in the range $0.1^\circ - 23^\circ$. Two wave vector ranges are considered: for $q > 0.6 \mu\text{m}^{-1}$ the power spectrum gives the static form factor of the scattering centres. In case of fractal aggregates, the asymptotic behaviour gives the independent measurement of the fractal dimension (Weitz and Lin, 1986). On the other hand, the low- q region ($q < 0.6 \mu\text{m}^{-1}$) is characterised by Talbot oscillations (see figures B.4 and B.5), delivering the information about the phase lag of the scattered waves. Following Potenza et al. (2010a) and Mazzoni et al. (2013), experimental data in the low- q region are fitted to the following function:

$$T(q) = 1 + \cos\left(\frac{q^2}{k} \tilde{z} - 2 \text{Arg } S(0)\right) \cdot \text{sinc}\left(\frac{q^2 L}{2nk} + \frac{\pi L}{8z_R}\right) \quad (\text{B.7})$$

where k is the wavenumber of the incoming radiation, n is the refractive index of the medium (water), L is the cell thickness, and \tilde{z} is the effective distance between the focal line and the observation plane, including the optical path through the cell and its walls. The phase lag introduced by the particles, $\text{Arg } S(0)$, is the only free parameter to be fitted to experimental data.

The performance of the system has been tested with diluted colloidal suspensions

of polystyrene spheres under different flow conditions. In particular, we recovered the size of spherical particles and the phase of the zero-angle scattering amplitude, $S(0)$.

As described in Ferri et al. (2004) and Mazzoni et al. (2013), calibration is needed in order to compensate for the modulation transfer function of the optical system. This affects the amplitude of the interference patterns at large q values and must be compensated to measure the corresponding static form factor correctly. The calibrated samples allow checking the reliability of the method in determining the static form factors and the phase of the forward scattering amplitude of fractal aggregates. Firstly, we acquired an extensive data set with a flow of pure, filtered water as a baseline. The average power spectrum has then subtracted to all the spectra retrieved afterwards. We then measured calibrated colloidal particles 600 nm in diameter (Thermo Fisher Scientific), which give an almost flat power spectrum. In figure B.2 data relating to the power spectral density of the

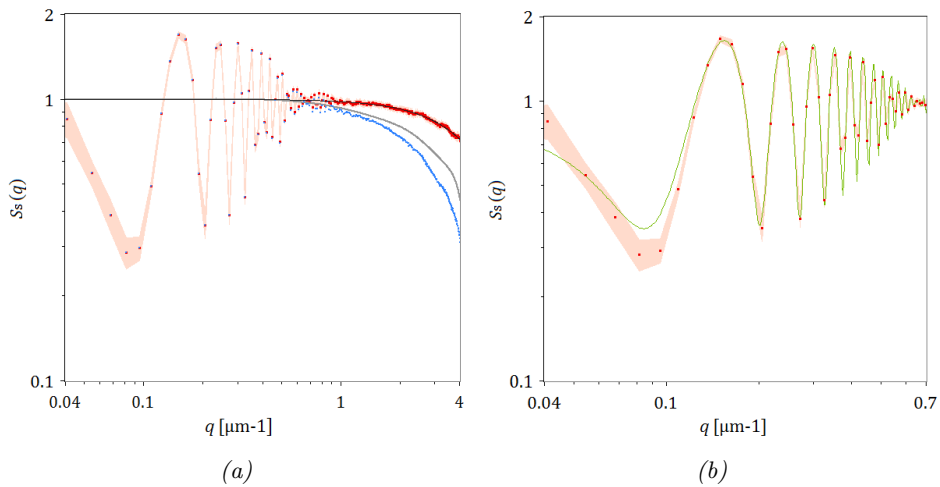


Figure B.2: (Left) Average of 10 normalised spectra from polystyrene particles 600 nm in diameter (red squares connected by the red solid line), compared to the corresponding Mie curve (black solid line). The pink area corresponds to the error bars. This measurement has been used for calibrating the instrument. The uncalibrated data is shown with a solid blue line, whereas the calibration curve is reported with a solid grey line. (Right) Detail of the oscillations in the low- q region. Detail of the Talbot-like oscillations up to $q \sim 0.6 \mu\text{m}^{-1}$. The phase lag can be retrieved by fitting to data equation (4.9) (green solid line), which yields $\text{Arg } S(0) = -1.00 \pm 0.03 \text{ rad}$. Mie calculations give $\text{Arg } S(0) = -1.05 \text{ rad}$

NFS speckles formed by polystyrene spheres 600 nm in diameter are reported. The data set is the average of the power spectra obtained from 10 independent frames, each averaged over the vertical extension of the region of interest (16 pixels). For $q > 0.6 \mu\text{m}^{-1}$, the data have been adapted to the expected Mie curve, thus obtaining the needed modulation transfer function to calibrate the instrument (grey solid line). Uncalibrated data are reported as blue dots.

In the low- q region, $q < 0.6 \mu\text{m}^{-1}$ the curve describing the Talbot oscillations (equation (4.9), green solid line) has been fitted to data. This gave $\text{Arg } S(0) = -1.00 \pm 0.03\text{rad}$ to be compared with $\text{Arg } S(0) = -1.05\text{rad}$ expected from Mie calculations. Interestingly, this result does not need any calibration, since the modulation transfer function affects data at large q values.

Calibration was then tested with particles $0.5 \mu\text{m}$ in diameter, with equivalent results: compensating raw data with the curve obtained above gave good agreement with Mie theory (figure B.3). Moreover, by fitting data with equation (4.9), we obtained $\text{Arg } S(0) = -1.1 \pm 0.03\text{rad}$, to be compared with the theoretical value $\text{Arg } S(0) = -1.15\text{rad}$.

We report in figures B.4 and B.5 the results obtained from diluted colloidal suspensions of calibrated polystyrene spheres 2 and $2.9 \mu\text{m}$ in diameter, monodisperse within $\sim 5\%$. The same data analysis procedure has been followed, now using the calibration curve obtained above to compensate for the modulation transfer function. Results are compared to the Mie curves without any free parameter.

In addition to the phase, the fit also gives the diameter of the spherical particles, which is found to be in excellent agreement with the nominal diameter of the samples. Notice the systematic discrepancy of the data sets close to the local minima, at $q = 3.3 \mu\text{m}^{-1}$ and $q = 1.9 \mu\text{m}^{-1}$, due to the small size polydispersity of the colloidal samples. Fitting Talbot oscillations to data gives $\text{Arg } S(0) = 0.2 \pm 0.05\text{rad}$ and $\text{Arg } S(0) = 0.33 \pm 0.05\text{rad}$ for $2.0 \mu\text{m}$ and $2.9 \mu\text{m}$ particles, respectively. On the other hand, Mie calculations give $\text{Arg } S(0) = 0.17\text{rad}$ and $\text{Arg } S(0) = 0.2\text{rad}$, respectively. The slight discrepancy can be ascribed to polydispersity as well.

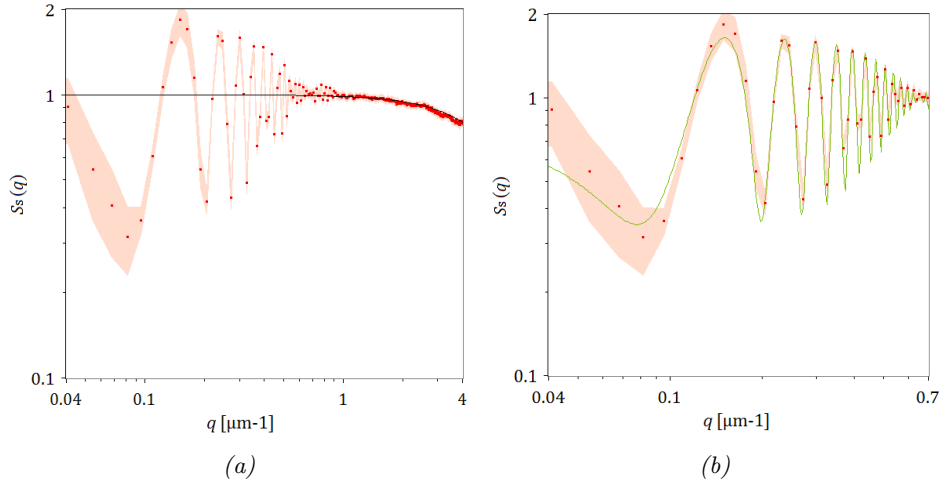


Figure B.3: (a) Average of 10 spectra from polystyrene particles 500 μm in diameter (red squares connected by the red solid line). The experimental data is in very good agreement with the corresponding Mie curve (black solid line). The pink area corresponds to the error bars. As expected, particles whose size is comparable to the wavelength give an almost flat spectrum throughout the q range. (b) Enlargement of the oscillations in the low- q region compared with the model (green), which gives $\text{Arg } S(0) = -1.1 \text{ rad}$.

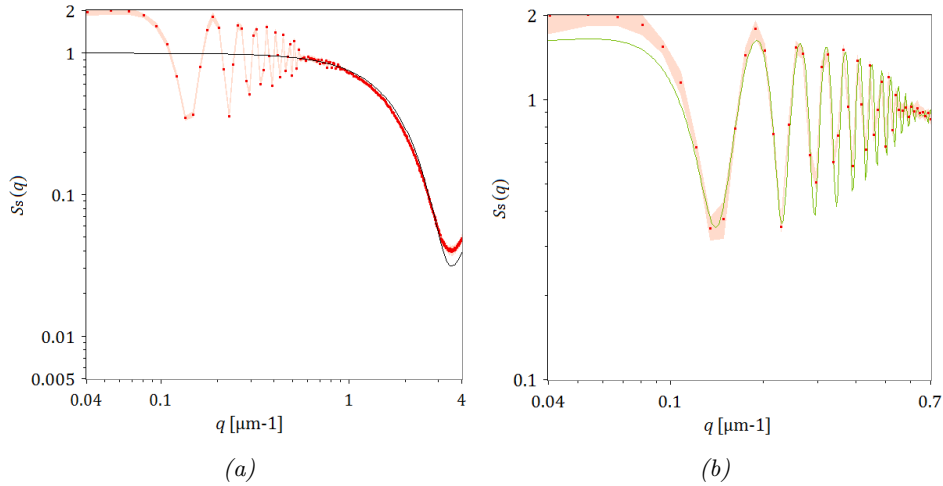


Figure B.4: Same as figure B.3 with 2.0 μm particles. The fit gives $\text{Arg } S(0) = 0.27 \text{ rad} \pm 0.05$.

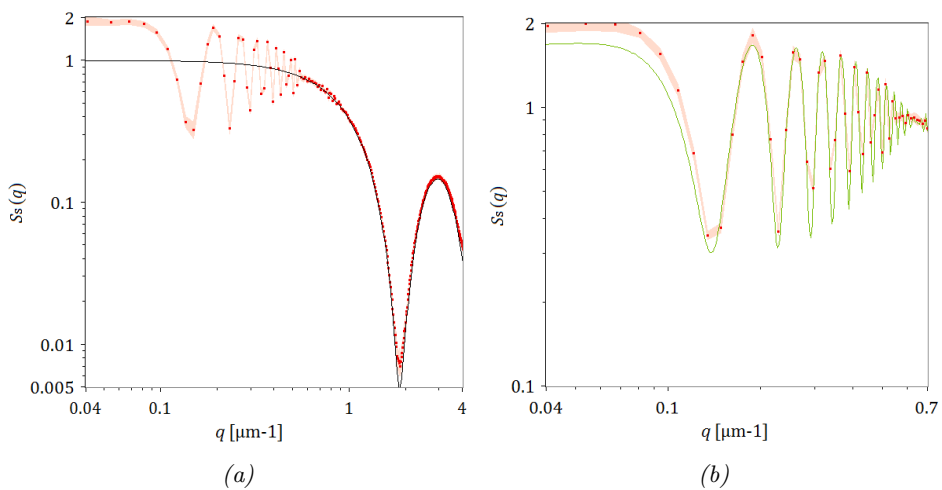


Figure B.5: Same as figure B.3 with $2.9 \mu\text{m}$ particles. The fit gives $\text{Arg } S(0) = 0.33 \text{ rad} \pm 0.05$.

Discrete Dipole Approximation

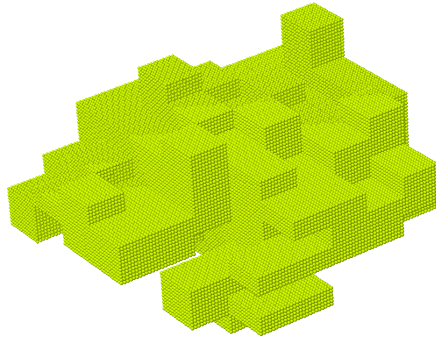


Figure C.1: Particle of arbitrary geometry (cluster of cuboid platelets) as discretized by DDA. Dipoles are represented as small spheres in the figure.

In the present thesis, we access the amplitude and phase of the scattered field from particles of diverse morphologies. To support the experimental findings, we used a numerical method to easily obtain the scattering parameters from non-spherical, user-defined particles. More broadly, first-principle modelling methods have recently considerable attention, and played an significant role in the advancement of many of domains of applied physics (Yurkin, 2013, Dubovik et al., 2006, Kahnert, 2016). The increasing computing power allows for fast, accurate and numerically stable calculations of local and scattered fields of structured, heterogeneous particles. Different approaches are available for solving macroscopic Maxwell equations numerically, such as the T-matrix method and the Discrete Dipole Approximation (DDA) (Penttilä et al., 2007, Redmond et al., 2010, Mishchenko et al., 2013, Somerville et al., 2015). The latter was chosen for its versatility and ease of use. The discrete dipole approximation (DDA) is a general method to simulate elastic light scattering by finite three-dimensional objects of arbitrary shape and composition (Purcell and Pennypacker, 1973). The basic idea of DDA is to divide the

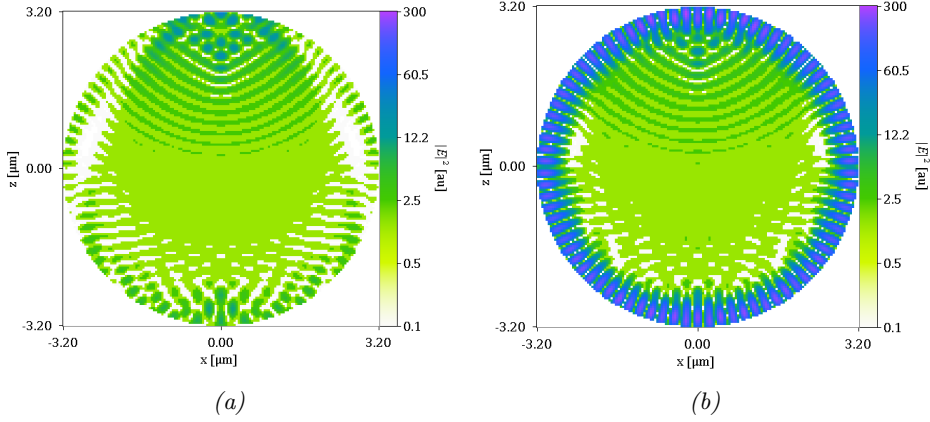


Figure C.2: Internal fields in a spherical water droplet $6.4\,\mu\text{m}$ in diameter (diametrical section) illuminated by linearly x -polarized light with (a) $\lambda = 0.577586\,\mu\text{m}$ (b) $\lambda = 0.577064\,\mu\text{m}$ displaying the intensity of the internal field with a false colour gradient. In the latter case, Mie theory predicts a resonance in scattering efficiency, which corresponds to a dramatic increase of the internal fields. The resonance is also reflected by the scattering cross section computed by the code (not displayed). Notice that the field is not homogeneous inside the sphere, since its size is larger than the wavelength, and it is not spherically symmetric due to the linear polarization of the incident wave.

scatterer in a set of small (cubical) sub-volumes each of which acts as a point-like dipole. Since the method includes the calculation of the interactions between all the dipoles in the volume as well as with the incident field, it has been referred to as *coupled dipole method* (Singham and Bohren, 1987). Without entering into too much detail, the calculation requires to iteratively solve a system of linear equations in order to obtain the polarization of each dipole in the scatterer, hence the radiated fields (see figure C.2).

We made extensive use of the open-source code ADDA, a highly portable C99 implementation of the DDA method by Yurkin and Hoekstra (2007) based on FFTW3 routines. It can run on a multiprocessor distributed-memory system in parallel mode. As a DDA algorithm, it is very flexible as regards the geometry of the scatterer, the applicability of this tool being, in principle, only limited by available computer resources. In this respect, the only constraint is that the size of the dipole must be small compared to both any structural length in the scatterer and the wavelength. An example of a particle with a user-defined geometry is shown in figure C.1: a cluster of cuboid platelets which approximates the features of a mineral dust particle, similar to the ones seen in section 3.4.

As a rule of thumb, the developers suggest that, for scatterers in free space with size comparable to the wavelength, the number of dipoles per wavelength should be ~ 10 , provided that the relative refractive index is such that $|m-1| < 2$. Otherwise, it should be increased with case-specific criteria; particles with a large refractive index need to be finely discretized. More generally, the accuracy requirements also vary upon particle shape and size. To be on the safe side, we chose to set $\sim 30 - 40$ dipoles per wavelength, while the refractive index of the particles was around 1.2 or lower, well within the suggested limit.

To our purposes, a very practical feature of ADDA is the wide variety of predefined shapes to be readily used. These include spheres, ellipsoids and prisms, whose parameters can be tuned according to specific requirements.

Simulations have been performed on a laboratory computer, and on a cluster for the larger particles which require more memory and computational speed. The field scattered at $\theta \in [0, 2\pi]$ is computed on both the scattering plane and the plane perpendicular to it. Many simulations are required to cover the whole range of the azimuth angle, ϕ .

The output displays the complex amplitude $S(\theta)$, and possibly the Mueller matrix, as a function of the scattering angle on the scattering plane and the plane perpendicular to it. The azimuth angle φ can be chosen by varying the orientation of the particle (by setting the Euler angles accordingly). The extinction and absorption cross sections, C_{ext} and C_{abs} , (and the efficiencies Q_{ext} and Q_{abs}) are also given as an output. The algorithm ensures that $C_{\text{ext}} = \frac{4\pi}{k^2} \Re S(0)$. For a thorough description of the code and its numerous options, we refer the reader to the dedicated user manual by Yurkin and Hoekstra (2014), which also includes a number of references covering many advanced aspects of scattering theory.

Bibliography

- Alaimo, M. D., Magatti, D., Ferri, F., and Potenza, M. A. C. (2006). Heterodyne speckle velocimetry. *Applied physics letters*, 88(19):191101.
- Albani, S., Balkanski, Y., Mahowald, N., Winckler, G., Maggi, V., and Delmonte, B. (2018). Aerosol-climate interactions during the last glacial maximum. *Current Climate Change Reports*, 4(2):99–114.
- Albani, S., Mahowald, N., Perry, A., Scanza, R., Zender, C., Heavens, N., Maggi, V., Kok, J., and Otto-Bliesner, B. (2014). Improved dust representation in the community atmosphere model. *Journal of Advances in Modeling Earth Systems*, 6(3):541–570.
- Albani, S., Mahowald, N. M., Delmonte, B., Maggi, V., and Winckler, G. (2012). Comparing modeled and observed changes in mineral dust transport and deposition to antarctica between the last glacial maximum and current climates. *Climate dynamics*, 38(9-10):1731–1755.
- Alloway, B. V., Lowe, D. J., Barrell, D. J., Newnham, R. M., Almond, P. C., Augustinus, P. C., Bertler, N. A., Carter, L., Litchfield, N. J., McGlone, M. S., et al. (2007). Towards a climate event stratigraphy for new zealand over the past 30 000 years (nz-intimate project). *Journal of Quaternary Science*, 22(1):9–35.
- Arons, B. (1992). A review of the cocktail party effect. *Journal of the American Voice I/O Society*, 12(7):35–50.
- Ashcroft, N. W. and Mermin, N. D. (2010). Solid state physics (saunders college, philadelphia, 1976). *Appendix N*.
- Babin, M. and Stramski, D. (2002). Light absorption by aquatic particles in the near-infrared spectral region. *Limnology and Oceanography*, 47(3):911–915.
- Balkanski, Y., Schulz, M., Claquin, T., and Guibert, S. (2007). Reevaluation of

- mineral aerosol radiative forcings suggests a better agreement with satellite and aeronet data. *Atmospheric Chemistry and Physics*, 7(1):81–95.
- Bergmann, M., Wirzberger, V., Krumpen, T., Lorenz, C., Primpke, S., Tekman, M. B., and Gerdt, G. (2017). High quantities of microplastic in arctic deep-sea sediments from the hausgarten observatory. *Environmental science & technology*, 51(19):11000–11010.
- Berne, B. J. and Pecora, R. (2000). *Dynamic light scattering: with applications to chemistry, biology, and physics*. Courier Corporation.
- Bertler, N. A., Conway, H., Dahl-Jensen, D., Emanuelsson, D. B., Winstrup, M., Vallelonga, P. T., Lee, J. E., Brook, E. J., Severinghaus, J. P., Fudge, T. J., et al. (2018). The ross sea dipole-temperature, snow accumulation and sea ice variability in the ross sea region, antarctica, over the past 2700 years. *Climate of the Past*, 14(2):193–214.
- Bigler, M., Svensson, A., Kettner, E., Vallelonga, P., Nielsen, M. E., and Steffensen, J. P. (2011). Optimization of high-resolution continuous flow analysis for transient climate signals in ice cores. *Environmental science & technology*, 45(10):4483–4489.
- Bohren, C. F. and Huffman, D. R. (2008). *Absorption and scattering of light by small particles*. John Wiley & Sons.
- Bond, T. C. and Bergstrom, R. W. (2006). Light absorption by carbonaceous particles: An investigative review. *Aerosol science and technology*, 40(1):27–67.
- Bond, T. C., Doherty, S. J., Fahey, D., Forster, P., Berntsen, T., DeAngelo, B., Flanner, M., Ghan, S., Kärcher, B., Koch, D., et al. (2013). Bounding the role of black carbon in the climate system: A scientific assessment. *Journal of Geophysical Research: Atmospheres*, 118(11):5380–5552.
- Borghese, F., Denti, P., and Saija, R. (2007). *Scattering from model nonspherical particles: theory and applications to environmental physics*. Springer Science & Business Media.
- Born, M. and Wolf, E. (2013). *Principles of optics: electromagnetic theory of propagation, interference and diffraction of light*. Elsevier.
- Brown, M., Errington, R., Rees, P., Williams, P., and Wilks, S. (2010). A highly efficient algorithm for the generation of random fractal aggregates. *Physica D: Nonlinear Phenomena*, 239(12):1061–1066.
- Burgay, F., Erhardt, T., Della Lunga, D., Jensen, C. M., Spolaor, A., Vallelonga, P., Fischer, H., and Barbante, C. (2019). Fe²⁺ in ice cores as a new potential proxy

- to detect past volcanic eruptions. *Science of the total environment*, 654:1110–1117.
- Bushell, G., Yan, Y., Woodfield, D., Raper, J., and Amal, R. (2002). On techniques for the measurement of the mass fractal dimension of aggregates. *Advances in Colloid and Interface Science*, 95(1):1–50.
- Carpineti, M., Ferri, F., Giglio, M., Paganini, E., and Perini, U. (1990). Salt-induced fast aggregation of polystyrene latex. *Physical Review A*, 42(12):7347.
- Ceratti, D. R., Rakita, Y., Cremonesi, L., Tenne, R., Kalchenko, V., Elbaum, M., Oron, D., Potenza, M. A. C., Hodes, G., and Cahen, D. (2018). Self-healing inside $apbbr_3$ halide perovskite crystals. *Advanced Materials*, 30(10):1706273.
- Charlson, R. J., Schwartz, S., Hales, J., Cess, R. D., Coakley, J. J., Hansen, J., and Hofmann, D. (1992). Climate forcing by anthropogenic aerosols. *Science*, 255(5043):423–430.
- Ch ylek, P. (1977). Extinction cross sections of arbitrarily shaped randomly oriented nonspherical particles. *JOSA*, 67(10):1348–1350.
- Ch ylek, P. and Klett, J. D. (1991). Extinction cross sections of nonspherical particles in the anomalous diffraction approximation. *JOSA A*, 8(2):274–281.
- Ch ylek, P. and Srivastava, V. (1983). Dielectric constant of a composite inhomogeneous medium. *Physical Review B*, 27(8):5098.
- Ch ylek, P. and Videen, G. (1998). Scattering by a composite sphere and effective medium approximations. *Optics communications*, 146(1-6):15–20.
- Claquin, T., Schulz, M., and Balkanski, Y. (1999). Modeling the mineralogy of atmospheric dust sources. *Journal of Geophysical Research: Atmospheres*, 104(D18):22243–22256.
- Coulter, W. H. (1953). Means for counting particles suspended in a fluid. US Patent 2,656,508.
- Cremonesi, L., Passerini, A., Tettamanti, A., Paroli, B., Delmonte, B., Albani, S., Cavaliere, F., Vigan , D., Bettiga, G., Sanvito, T., Pullia, A., and Potenza, M. A. C. (Dec 2019). Multiparametric optical characterization of airborne dust with single particle extinction and scattering. *Aerosol Science and Technology*, 0(ja):1–15.
- Cuccia, E., Bernardoni, V., Massab , D., Prati, P., Valli, G., and Vecchi, R. (2010). An alternative way to determine the size distribution of airborne particulate matter. *Atmospheric Environment*, 44(27):3304–3313.

- De Angelis, M., Tison, J.-L., Morel-Fourcade, M.-C., and Susini, J. (2013). Micro-investigation of epica dome c bottom ice: evidence of long term in situ processes involving acid-salt interactions, mineral dust, and organic matter. *Quaternary science reviews*, 78:248–265.
- Debye, P., Anderson Jr, H., and Brumberger, H. (1957). Scattering by an inhomogeneous solid. ii. the correlation function and its application. *Journal of applied Physics*, 28(6):679–683.
- Debye, P. and Bueche, A. (1949). Scattering by an inhomogeneous solid. *Journal of Applied Physics*, 20(6):518–525.
- Delmonte, B., Baroni, C., Andersson, P. S., Schoberg, H., Hansson, M., Aciego, S., Petit, J.-R., Albani, S., Mazzola, C., Maggi, V., et al. (2010). Aeolian dust in the talos dome ice core (east antarctica, pacific/ross sea sector): Victoria land versus remote sources over the last two climate cycles. *Journal of Quaternary Science*, 25(8):1327–1337.
- Delmonte, B., Paleari, C. I., Andò, S., Garzanti, E., Andersson, P. S., Petit, J. R., Crosta, X., Narcisi, B., Baroni, C., Salvatore, M. C., et al. (2017). Causes of dust size variability in central east antarctica (dome b): Atmospheric transport from expanded south american sources during marine isotope stage 2. *Quaternary Science Reviews*, 168:55–68.
- Delmonte, B., Petit, J., Andersen, K. K., Basile-Doelsch, I., Maggi, V., and Lipenkov, V. Y. (2004). Dust size evidence for opposite regional atmospheric circulation changes over east antarctica during the last climatic transition. *Climate Dynamics*, 23(3-4):427–438.
- Delmonte, B., Petit, J., and Maggi, V. (2002). Glacial to holocene implications of the new 27000-year dust record from the epica dome c (east antarctica) ice core. *Climate Dynamics*, 18(8):647–660.
- Delmonte, B., Petit, J. R., Krinner, G., Maggi, V., Jouzel, J., and Udisti, R. (2005). Ice core evidence for secular variability and 200-year dipolar oscillations in atmospheric circulation over east antarctica during the holocene. *Climate dynamics*, 24(6):641–654.
- Dubovik, O., Holben, B., Eck, T. F., Smirnov, A., Kaufman, Y. J., King, M. D., Tanré, D., and Slutsker, I. (2002). Variability of absorption and optical properties of key aerosol types observed in worldwide locations. *Journal of the atmospheric sciences*, 59(3):590–608.
- Dubovik, O., Sinyuk, A., Lapyonok, T., Holben, B. N., Mishchenko, M., Yang, P.,

- Eck, T. F., Volten, H., Munoz, O., Veihelmann, B., et al. (2006). Application of spheroid models to account for aerosol particle nonsphericity in remote sensing of desert dust. *Journal of Geophysical Research: Atmospheres*, 111(D11).
- Dusek, U., Frank, G., Hildebrandt, L., Curtius, J., Schneider, J., Walter, S., Chand, D., Drewnick, F., Hings, S., Jung, D., et al. (2006). Size matters more than chemistry for cloud-nucleating ability of aerosol particles. *Science*, 312(5778):1375–1378.
- Ebert, E. E. and Curry, J. A. (1992). A parameterization of ice cloud optical properties for climate models. *Journal of Geophysical Research: Atmospheres*, 97(D4):3831–3836.
- Ellis, A., Edwards, R., Saunders, M., Chakrabarty, R. K., Subramanian, R., Timms, N. E., Van Riessen, A., Smith, A. M., Lambrinidis, D., Nunes, L. J., et al. (2016). Individual particle morphology, coatings, and impurities of black carbon aerosols in antarctic ice and tropical rainfall. *Geophysical Research Letters*, 43(22):11–875.
- Emanuelsson, B., Baisden, W., Bertler, N., Keller, E., and Gkinis, V. (2015). High-resolution continuous-flow analysis setup for water isotopic measurement from ice cores using laser spectroscopy. *Atmospheric Measurement Techniques Discussions*, 7:12081–12124.
- Fairbanks, M., McCarthy, D., Scott, S., Brown, S., and Taylor, R. (2011). Fractal electronic devices: simulation and implementation. *Nanotechnology*, 22(36):365304.
- Farias, T. L., Köylü, Ü. Ö., and Carvalho, M. d. G. (1996). Range of validity of the rayleigh–debye–gans theory for optics of fractal aggregates. *Applied Optics*, 35(33):6560–6567.
- Fearn, H., James, D. F., and Milonni, P. W. (1996). Microscopic approach to reflection, transmission, and the ewald–oseen extinction theorem. *American Journal of Physics*, 64(8):986–995.
- Ferrero, L., Ritter, C., Cappelletti, D., Moroni, B., Mocnik, G., Mazzola, M., Lupi, A., Becagli, S., Traversi, R., Cataldi, M., et al. (2019). Aerosol optical properties in the arctic: The role of aerosol chemistry and dust composition in a closure experiment between lidar and tethered balloon vertical profiles. *Science of The Total Environment*.
- Ferri, F., Calegari, G. R., Molteni, M., Cardinali, B., Magatti, D., and Rocco, M. (2015). Size and density of fibers in fibrin and other filamentous networks from

- turbidimetry: Beyond a revisited carr–hermans method, accounting for fractality and porosity. *Macromolecules*, 48(15):5423–5432.
- Ferri, F., Giglio, M., Paganini, E., and Perini, U. (1988). Low-angle elastic light scattering study of diffusion-limited aggregation. *EPL (Europhysics Letters)*, 7(7):599.
- Ferri, F., Magatti, D., Pescini, D., Potenza, M. A. C., and Giglio, M. (2004). Heterodyne near-field scattering: A technique for complex fluids. *Physical Review E*, 70(4):041405.
- Field, J. P., Belnap, J., Breshears, D. D., Neff, J. C., Okin, G. S., Whicker, J. J., Painter, T. H., Ravi, S., Reheis, M. C., and Reynolds, R. L. (2010). The ecology of dust. *Frontiers in Ecology and the Environment*, 8(8):423–430.
- Fischer, H., Fundel, F., Ruth, U., Twarloh, B., Wegner, A., Udisti, R., Becagli, S., Castellano, E., Morganti, A., Severi, M., et al. (2007). Reconstruction of millennial changes in dust emission, transport and regional sea ice coverage using the deep epica ice cores from the atlantic and indian ocean sector of antarctica. *Earth and Planetary Science Letters*, 260(1-2):340–354.
- Flesch, J. C., Spicer, P. T., and Pratsinis, S. E. (1999). Laminar and turbulent shear-induced flocculation of fractal aggregates. *AIChE journal*, 45(5):1114–1124.
- Fletcher, N. H. et al. (2011). *The physics of rainclouds*. Cambridge University Press.
- Fu, Q., Thorsen, T., Su, J., Ge, J., and Huang, J. (2009). Test of mie-based single-scattering properties of non-spherical dust aerosols in radiative flux calculations. *Journal of Quantitative Spectroscopy and Radiative Transfer*, 110(14-16):1640–1653.
- Garzonio, R., Di Mauro, B., Cogliati, S., Rossini, M., Panigada, C., Delmonte, B., Maggi, V., and Colombo, R. (2018). A novel hyperspectral system for high resolution imaging of ice cores: Application to light-absorbing impurities and ice structure. *Cold Regions Science and Technology*, 155:47–57.
- Gaudichet, A., Petit, J., Lefevre, R., and Lorius, C. (1986). An investigation by analytical transmission electron microscopy of individual insoluble microparticles from antarctic (dome c) ice core samples. *Tellus B*, 38(3-4):250–261.
- Ghan, S. J. and Zaveri, R. A. (2007). Parameterization of optical properties for hydrated internally mixed aerosol. *Journal of Geophysical Research: Atmospheres*, 112(D10).

- Gmachowski, L. (2002). Calculation of the fractal dimension of aggregates. *Colloids and Surfaces A: Physicochemical and Engineering Aspects*, 211(2-3):197–203.
- Goldburg, W. (1999). Dynamic light scattering. *American Journal of Physics*, 67(12):1152–1160.
- Goodman, J. W. (2005). *Introduction to Fourier optics*. Roberts and Company Publishers.
- Goy, C., Potenza, M. A., Dederà, S., Tomut, M., Guillermin, E., Kalinin, A., Voss, K.-O., Schottelius, A., Petridis, N., Prosvetov, A., et al. (2018). Shrinking of rapidly evaporating water microdroplets reveals their extreme supercooling. *Physical review letters*, 120(1):015501.
- Halliday, D. and Curtis, A. (2009). Generalized optical theorem for surface waves and layered media. *Physical Review E*, 79(5):056603.
- Hansen, J. and Nazarenko, L. (2004). Soot climate forcing via snow and ice albedos. *Proceedings of the National Academy of Sciences*, 101(2):423–428.
- Haywood, J. and Boucher, O. (2000). Estimates of the direct and indirect radiative forcing due to tropospheric aerosols: A review. *Reviews of geophysics*, 38(4):513–543.
- Heim, M., Mullins, B. J., Umhauer, H., and Kasper, G. (2008). Performance evaluation of three optical particle counters with an efficient “multimodal” calibration method. *Journal of aerosol science*, 39(12):1019–1031.
- Heinson, W., Sorensen, C., and Chakrabarti, A. (2012). A three parameter description of the structure of diffusion limited cluster fractal aggregates. *Journal of colloid and interface science*, 375(1):65–69.
- Henning, T. and Stognienko, R. (1996). Dust opacities for protoplanetary accretion disks: influence of dust aggregates. *Astronomy and Astrophysics*, 311:291–303.
- Hinkley, T. K., Lamothe, P. J., Wilson, S. A., Finnegan, D. L., and Gerlach, T. M. (1999). Metal emissions from kilauea, and a suggested revision of the estimated worldwide metal output by quiescent degassing of volcanoes. *Earth and Planetary Science Letters*, 170(3):315–325.
- Holben, B. N., Eck, T., Slutsker, I., Tanre, D., Buis, J., Setzer, A., Vermote, E., Reagan, J. A., Kaufman, Y., Nakajima, T., et al. (1998). Aeronet—a federated instrument network and data archive for aerosol characterization. *Remote sensing of environment*, 66(1):1–16.
- Holve, D. and Self, S. A. (1979). Optical particle sizing for in situ measurements

- part 1. *Applied Optics*, 18(10):1632–1645.
- Horvath, H. (2009). Gustav mie and the scattering and absorption of light by particles: Historic developments and basics. *Journal of Quantitative Spectroscopy and Radiative Transfer*, 110(11):787–799.
- Jackson, J. D. (1999). Classical electrodynamics.
- Jacobson, M. Z. (2001). Strong radiative heating due to the mixing state of black carbon in atmospheric aerosols. *Nature*, 409(6821):695.
- Jones, A. (1988). Modelling interstellar extinction–i. porous grains. *Monthly Notices of the Royal Astronomical Society*, 234(2):209–218.
- Kahnert, M. (2016). Numerical solutions of the macroscopic maxwell equations for scattering by non-spherical particles: a tutorial review. *Journal of Quantitative Spectroscopy and Radiative Transfer*, 178:22–37.
- Kahnert, M., Nousiainen, T., Lindqvist, H., and Ebert, M. (2012). Optical properties of light absorbing carbon aggregates mixed with sulfate: assessment of different model geometries for climate forcing calculations. *Optics express*, 20(9):10042–10058.
- Kahnert, M., Nousiainen, T., and Räisänen, P. (2007). Mie simulations as an error source in mineral aerosol radiative forcing calculations. *Quarterly Journal of the Royal Meteorological Society: A journal of the atmospheric sciences, applied meteorology and physical oceanography*, 133(623):299–307.
- Kaufman, Y. J. and Koren, I. (2006). Smoke and pollution aerosol effect on cloud cover. *Science*, 313(5787):655–658.
- Kaufman, Y. J., Koren, I., Remer, L. A., Rosenfeld, D., and Rudich, Y. (2005). The effect of smoke, dust, and pollution aerosol on shallow cloud development over the atlantic ocean. *Proceedings of the National Academy of Sciences*, 102(32):11207–11212.
- Kaufmann, P. R., Federer, U., Hutterli, M. A., Bigler, M., Schupbach, S., Ruth, U., Schmitt, J., and Stocker, T. F. (2008). An improved continuous flow analysis system for high-resolution field measurements on ice cores. *Environmental science & technology*, 42(21):8044–8050.
- Kenyon, S. L. and Storey, J. W. (2006). A review of optical sky brightness and extinction at dome c, antarctica. *Publications of the Astronomical Society of the Pacific*, 118(841):489.
- Kinnan, M. K. and Chumanov, G. (2010). Plasmon coupling in two-dimensional

- arrays of silver nanoparticles: Ii. effect of the particle size and interparticle distance. *The Journal of Physical Chemistry C*, 114(16):7496–7501.
- Kjær, H. A., Dallmayr, R., Gabrieli, J., Goto-Azuma, K., Hirabayashi, M., Svensson, A., and Vallenga, P. (2015). Greenland ice cores constrain glacial atmospheric fluxes of phosphorus. *Journal of Geophysical Research: Atmospheres*, 120(20):10–810.
- Kjær, H. A., Vallenga, P., Vinther, B., Winstrup, M., Simonsen, M., Maffezzoli, N., and Jensen, C. M. (2017). Subannual layer variability in greenland firn cores. In *EGU General Assembly Conference Abstracts*, volume 19, page 11581.
- Klein, O. and Nishina, Y. (1929). Über die streuung von strahlung durch freie elektronen nach der neuen relativistischen quantendynamik von dirac. *Zeitschrift für Physik*, 52(11-12):853–868.
- Kok, J. F., Parteli, E. J., Michaels, T. I., and Karam, D. B. (2012). The physics of wind-blown sand and dust. *Reports on progress in Physics*, 75(10):106901.
- Kokhanovsky, A. (2016). *Light Scattering Reviews, Volume 11: Light Scattering and Radiative Transfer*. Springer.
- Kou, L., Labrie, D., and Chylek, P. (1993). Refractive indices of water and ice in the 0.65-to 2.5- μm spectral range. *Applied optics*, 32(19):3531–3540.
- Krasavin, A. V., Segovia, P., Dubrovka, R., Olivier, N., Wurtz, G. A., Ginzburg, P., and Zayats, A. V. (2018). Generalization of the optical theorem: experimental proof for radially polarized beams. *Light: Science & Applications*, 7(1):36.
- Kylling, A., Groot Zwaafink, C., and Stohl, A. (2018). Mineral dust instantaneous radiative forcing in the arctic. *Geophysical Research Letters*, 45(9):4290–4298.
- Lalor, É. and Wolf, E. (1972). Exact solution of the equations of molecular optics for refraction and reflection of an electromagnetic wave on a semi-infinite dielectric. *JOSA*, 62(10):1165–1174.
- Lambert, F., Delmonte, B., Petit, J.-R., Bigler, M., Kaufmann, P. R., Hutterli, M. A., Stocker, T. F., Ruth, U., Steffensen, J. P., and Maggi, V. (2008). Dust-climate couplings over the past 800,000 years from the epica dome c ice core. *Nature*, 452(7187):616.
- Lattuada, M., Wu, H., and Morbidelli, M. (2003). A simple model for the structure of fractal aggregates. *Journal of colloid and interface science*, 268(1):106–120.
- Lawrence, C. R. and Neff, J. C. (2009). The contemporary physical and chemical flux of aeolian dust: A synthesis of direct measurements of dust deposition.

- Chemical Geology*, 267(1-2):46–63.
- Le Ru, E. C., Somerville, W. R., and Augu  , B. (2013). Radiative correction in approximate treatments of electromagnetic scattering by point and body scatterers. *Physical Review A*, 87(1):012504.
- Lef  vre, M., Oumbe, A., Blanc, P., Espinar, B., Gschwind, B., Qu, Z., Wald, L., Homscheidt, M. S., Hoyer-Klick, C., Arola, A., et al. (2013). Mcclear: a new model estimating downwelling solar radiation at ground level in clear-sky conditions. *Atmospheric Measurement Techniques*, 6:2403–2418.
- Leinonen, J., Kneifel, S., Moiseev, D., Tyynel  , J., Tanelli, S., and Nousiainen, T. (2012). Evidence of non spheroidal behavior in millimeter-wavelength radar observations of snowfall. *Journal of Geophysical Research: Atmospheres*, 117(D18).
- Lennon, F. E., Cianci, G. C., Cipriani, N. A., Hensing, T. A., Zhang, H. J., Chen, C.-T., Murgu, S. D., Vokes, E. E., Vannier, M. W., and Salgia, R. (2015). Lung cancer—a fractal viewpoint. *Nature reviews Clinical oncology*, 12(11):664.
- Levasseur-Regourd, A., Cabane, M., Worms, J., and Haudebourg, V. (1997). Physical properties of dust in the solar system: relevance of a computational approach and of measurements under microgravity conditions. *Advances in Space Research*, 20(8):1585–1594.
- Li, A. and Draine, B. T. (2002). Are silicon nanoparticles an interstellar dust component? *The Astrophysical Journal*, 564(2):803.
- Lin, M., Lindsay, H., Weitz, D., Ball, R., Klein, R., and Meakin, P. (1989). Universality of fractal aggregates as probed by light scattering. *Proceedings of the Royal Society of London. A. Mathematical and Physical Sciences*, 423(1864):71–87.
- Luck, J. (1991). Conductivity of random resistor networks: an investigation of the accuracy of the effective-medium approximation. *Physical Review B*, 43(5):3933.
- Lunga, D. D., M  ller, W., Rasmussen, S. O., Svensson, A., and Vallenga, P. (2017). Calibrated cryo-cell uv-la-icpms elemental concentrations from the ngrip ice core reveal abrupt, sub-annual variability in dust across the gi-21.2 interstadial period. *The Cryosphere*, 11(3):1297–1309.
- Mackowski, D. W. (1995). Electrostatics analysis of radiative absorption by sphere clusters in the rayleigh limit: application to soot particles. *Applied optics*, 34(18):3535–3545.
- Maffezzoli, N., Vallenga, P., Spolaor, A., Barbante, C., Edwards, R., Saiz-Lopez, A., Kj  r, H. A., Simonsen, M., and Vinther, B. (2017). 125,000 year arctic sea ice variability from the renland ice core. In *EGU General Assembly Conference*

Abstracts, volume 19, page 10478.

- Magatti, D., Alaimo, M. D., Potenza, M. A. C., and Ferri, F. (2008). Dynamic heterodyne near field scattering. *Applied Physics Letters*, 92(24):241101.
- Maggi, V. (1997). Mineralogy of atmospheric microparticles deposited along the greenland ice core project ice core. *Journal of Geophysical Research: Oceans*, 102(C12):26725–26734.
- Maher, B., Prospero, J., Mackie, D., Gaiero, D., Hesse, P. P., and Balkanski, Y. (2010). Global connections between aeolian dust, climate and ocean biogeochemistry at the present day and at the last glacial maximum. *Earth-Science Reviews*, 99(1-2):61–97.
- Mahowald, N., Albani, S., Kok, J. F., Engelstaeder, S., Scanza, R., Ward, D. S., and Flanner, M. G. (2014). The size distribution of desert dust aerosols and its impact on the earth system. *Aeolian Research*, 15:53–71.
- Mahowald, N. M., Baker, A. R., Bergametti, G., Brooks, N., Duce, R. A., Jickells, T. D., Kubilay, N., Prospero, J. M., and Tegen, I. (2005). Atmospheric global dust cycle and iron inputs to the ocean. *Global biogeochemical cycles*, 19(4).
- Mahowald, N. M., Engelstaedter, S., Luo, C., Sealy, A., Artaxo, P., Benitez-Nelson, C., Bonnet, S., Chen, Y., Chuang, P. Y., Cohen, D. D., Dulac, F., Herut, B., Johansen, A. M., Kubilay, N., Losno, R., Maenhaut, W., Paytan, A., Prospero, J. M., Shank, L. M., and Siefert, R. L. (2009). Atmospheric iron deposition: global distribution, variability, and human perturbations. *Annual Review of Marine Science*, 1(1):245–278.
- Mann, I., Nakamura, A., and Mukai, T. (2009). *Small bodies in planetary systems*, volume 758. Springer.
- Mariani, F., Bernardoni, V., Riccobono, F., Vecchi, R., Valli, G., Sanvito, T., Paroli, B., Pullia, A., and Potenza, M. A. C. (2017). Single particle extinction and scattering allows novel optical characterization of aerosols. *Journal of Nanoparticle Research*, 19(8):291.
- Marín, I., Nunes, S., Sánchez-Pérez, E. D., Aparicio, F., Estrada, M., Marrasé, C., Moreno, T., Wagener, T., Querol, X., and Peters, F. (2017). Anthropogenic versus mineral aerosols in the stimulation of microbial planktonic communities in coastal waters of the northwestern mediterranean sea. *Science of the Total Environment*, 574:553–568.
- Marino, F., Maggi, V., Delmonte, B., Ghermandi, G., and Petit, J. R. (2004). Elemental composition (si, fe, ti) of atmospheric dust over the last 220 kyr from

- the epica ice core (dome c, antarctica). *Annals of glaciology*, 39:110–118.
- Markel, V. A. (2016). Introduction to the maxwell garnett approximation: tutorial. *JOSA A*, 33(7):1244–1256.
- Marks, F. (1987). Marine aerosols and whitecaps in the north atlantic and greenland sea regions. *Deutsche Hydrografische Zeitschrift*, 40(2):71–79.
- Massabò, D., Bernardoni, V., Bove, M., Brunengo, A., Cuccia, E., Piazzalunga, A., Prati, P., Valli, G., and Vecchi, R. (2013). A multi-wavelength optical set-up for the characterization of carbonaceous particulate matter. *Journal of Aerosol Science*, 60:34–46.
- Massabò, D., Caponi, L., Bernardoni, V., Bove, M., Brotto, P., Calzolari, G., Casola, F., Chiari, M., Fedi, M., Fermo, P., et al. (2015). Multi-wavelength optical determination of black and brown carbon in atmospheric aerosols. *Atmospheric Environment*, 108:1–12.
- Masson-Delmotte, V., Stenni, B., Pol, K., Braconnot, P., Cattani, O., Falourd, S., Kageyama, M., Jouzel, J., Landais, A., Minster, B., et al. (2010). Epica dome c record of glacial and interglacial intensities. *Quaternary Science Reviews*, 29(1-2):113–128.
- Mather, T., Pyle, D., and Oppenheimer, C. (2003). Tropospheric volcanic aerosol. *Geophysical Monograph-American Geophysical Union*, 139:189–212.
- Matsui, H. (2017). Development of a global aerosol model using a two-dimensional sectional method: 1. model design. *Journal of Advances in Modeling Earth Systems*, 9(4):1921–1947.
- Maxwell-Garnett, J. (1904). Philos. trans. r. soc. london. In *Ser. A*, volume 203, page 385.
- Mazzoni, S., Potenza, M. A. C., Alaimo, M. D., Veen, S., Dielissen, M., Leussink, E., Dewandel, J.-L., Minster, O., Kufner, E., Wegdam, G., et al. (2013). Sodicollloid: A combination of static and dynamic light scattering on board the international space station. *Review of Scientific Instruments*, 84(4):043704.
- Mie, G. (1908). Beiträge zur optik trüber medien, speziell kolloidaler metallösungen. *Annalen der physik*, 330(3):377–445.
- Miles, R. B., Lempert, W. R., and Forkey, J. N. (2001). Laser rayleigh scattering. *Measurement Science and Technology*, 12(5):R33.
- Miller, R., Cakmur, R., Perlwitz, J., Geogdzhayev, I., Ginoux, P., Koch, D., Kohfeld, K., Prigent, C., Ruedy, R., Schmidt, G., et al. (2006). Mineral dust aerosols

- in the nasa goddard institute for space sciences model atmospheric general circulation model. *Journal of Geophysical Research: Atmospheres*, 111(D6).
- Minnai, C. (2018). *Optical and Electrical properties of metal-polymer nanocomposites fabricated with Supersonic Cluster Beam Implantation*. PhD thesis, Università degli Studi di Milano.
- Minnai, C., Cremonesi, L., Milani, P., and Potenza, M. A. C. (2019). A very simple scheme for spectrally resolved imaging by means of curved polymeric gratings. *Materials Research Express*, 6(6):065044.
- Minnai, C., Di Vece, M., and Milani, P. (2017). Mechanical-optical-electro modulation by stretching a polymer-metal nanocomposite. *Nanotechnology*, 28(35):355702.
- Minnai, C. and Milani, P. (2015). Metal-polymer nanocomposite with stable plasmonic tuning under cyclic strain conditions. *Applied Physics Letters*, 107(7):073106.
- Mishchenko, M., Lacis, A., Carlson, B., and Travis, L. (1995). Nonsphericity of dust-like tropospheric aerosols: Implications for aerosol remote sensing and climate modeling. *Geophysical Research Letters*, 22(9):1077–1080.
- Mishchenko, M. I. (2018). “independent” and “dependent” scattering by particles in a multi-particle group. *OSA Continuum*, 1(1):243–260.
- Mishchenko, M. I., Dlugach, J. M., and Liu, L. (2016). Applicability of the effective-medium approximation to heterogeneous aerosol particles. *Journal of Quantitative Spectroscopy and Radiative Transfer*, 178:284–294.
- Mishchenko, M. I., Hovenier, J. W., and Travis, L. D. (2000). Light scattering by nonspherical particles: theory, measurements, and applications.
- Mishchenko, M. I., Liu, L., and Mackowski, D. W. (2013). T-matrix modeling of linear depolarization by morphologically complex soot and soot-containing aerosols. *Journal of Quantitative Spectroscopy and Radiative Transfer*, 123:135–144.
- Mishchenko, M. I. and Yurkin, M. A. (2017). On the concept of random orientation in far-field electromagnetic scattering by nonspherical particles. *Optics letters*, 42(3):494–497.
- Moosmüller, H., Chakrabarty, R., and Arnott, W. (2009). Aerosol light absorption and its measurement: A review. *Journal of Quantitative Spectroscopy and Radiative Transfer*, 110(11):844–878.

- Moosmüller, H., Engelbrecht, J. P., Skiba, M., Frey, G., Chakrabarty, R. K., and Arnott, W. P. (2012). Single scattering albedo of fine mineral dust aerosols controlled by iron concentration. *Journal of Geophysical Research: Atmospheres*, 117(D11).
- Moosmüller, H. and Sorensen, C. (2018). Small and large particle limits of single scattering albedo for homogeneous, spherical particles. *Journal of Quantitative Spectroscopy and Radiative Transfer*, 204:250–255.
- Müller, D., Weinzierl, B., Petzold, A., Kandler, K., Ansmann, A., Müller, T., Tesche, M., Freudenthaler, V., Esselborn, M., Heese, B., et al. (2010). Mineral dust observed with aeronet sun photometer, raman lidar, and in situ instruments during samum 2006: Shape-independent particle properties. *Journal of Geophysical Research: Atmospheres*, 115(D7).
- Munoz, O., Volten, H., De Haan, J., Vassen, W., and Hovenier, J. (2001). Experimental determination of scattering matrices of randomly oriented fly ash and clay particles at 442 and 633 nm. *Journal of Geophysical Research: Atmospheres*, 106(D19):22833–22844.
- Navarro, J. A., Varma, V., Riipinen, I., Seland, Ø., Kirkevåg, A., Struthers, H., Iversen, T., Hansson, H.-C., and Ekman, A. M. (2016). Amplification of arctic warming by past air pollution reductions in europe. *Nature Geoscience*, 9(4):277.
- Neff, P. D. and Bertler, N. A. (2015). Trajectory modeling of modern dust transport to the southern ocean and antarctica. *Journal of Geophysical Research: Atmospheres*, 120(18):9303–9322.
- Newton, R. G. (1976). Optical theorem and beyond. *American Journal of Physics*, 44(7):639–642.
- Nousiainen, T. (2009). Optical modeling of mineral dust particles: A review. *Journal of Quantitative Spectroscopy and Radiative Transfer*, 110(14-16):1261–1279.
- Nousiainen, T., Muinonen, K., and Räisänen, P. (2003). Scattering of light by large saharan dust particles in a modified ray optics approximation. *Journal of Geophysical Research: Atmospheres*, 108(D1):AAC–12.
- Nousiainen, T., Muñoz, O., Lindqvist, H., Mauno, P., and Videen, G. (2011). Light scattering by large saharan dust particles: comparison of modeling and experimental data for two samples. *Journal of Quantitative Spectroscopy and Radiative Transfer*, 112(3):420–433.
- Parola, A., Piazza, R., and Degiorgio, V. (2014). Optical extinction, refractive

- index, and multiple scattering for suspensions of interacting colloidal particles. *The Journal of chemical physics*, 141(12):124902.
- Penttilä, A., Zubko, E., Lumme, K., Muinonen, K., Yurkin, M. A., Draine, B., Rahola, J., Hoekstra, A. G., and Shkuratov, Y. (2007). Comparison between discrete dipole implementations and exact techniques. *Journal of Quantitative Spectroscopy and Radiative Transfer*, 106(1-3):417–436.
- Petit, J. R., Wegner, A., Narsici, B., Svensson, A., Bigler, M., and Steffensen, J. P. (2013). The neem record of aeolian dust: contributions from coulter counter measurements. In *EGU General Assembly Conference Abstracts*, volume 15.
- Piazzalunga, A., Bernardoni, V., Fermo, P., and Vecchi, R. (2013). Optimisation of analytical procedures for the quantification of ionic and carbonaceous fractions in the atmospheric aerosol and applications to ambient samples. *Analytical and bioanalytical chemistry*, 405(2-3):1123–1132.
- Pollack, J. B. and Cuzzi, J. N. (1980). Scattering by nonspherical particles of size comparable to a wavelength: A new semi-empirical theory and its application to tropospheric aerosols. *Journal of the Atmospheric Sciences*, 37(4):868–881.
- Pöschl, U. (2005). Atmospheric aerosols: composition, transformation, climate and health effects. *Angewandte Chemie International Edition*, 44(46):7520–7540.
- Potenza, M. A. C. (2015). The daylight sky and avogadro’s number. *European Journal of Physics*, 36(6):065040.
- Potenza, M. A. C., Albani, S., Delmonte, B., Villa, S., Sanvito, T., Paroli, B., Pullia, A., Baccolo, G., Mahowald, N., and Maggi, V. (2016a). Shape and size constraints on dust optical properties from the dome c ice core, antarctica. *Scientific reports*, 6:28162.
- Potenza, M. A. C., Cremonesi, L., Delmonte, B., Sanvito, T., Paroli, B., Pullia, A., Baccolo, G., and Maggi, V. (2017a). Single-particle extinction and scattering method allows for detection and characterization of aggregates of aeolian dust grains in ice cores. *ACS Earth and Space Chemistry*, 1(5):261–269.
- Potenza, M. A. C., Manca, A., Veen, S. J., Weber, B., Mazzoni, S., Schall, P., and Wegdam, G. H. (2014). Dynamics of colloidal aggregation in microgravity by critical casimir forces. *EPL (Europhysics Letters)*, 106(6):68005.
- Potenza, M. A. C. and Milani, P. (2014). Free nanoparticle characterization by optical scattered field analysis: opportunities and perspectives. *Journal of nanoparticle research*, 16(11):2680.
- Potenza, M. A. C., Minnai, C., and Milani, P. (2016b). Metal-polymer nanocom-

- posites for stretchable optics and plasmonics. In *International Symposium on Clusters and Nanomaterials*, volume 10174, page 101740G. International Society for Optics and Photonics.
- Potenza, M. A. C., Nazzari, D., Cremonesi, L., Denti, I., and Milani, P. (2017b). Hyperspectral imaging with deformable gratings fabricated with metal-elastomer nanocomposites. *Review of Scientific Instruments*, 88(11):113105.
- Potenza, M. A. C., Sabareesh, K., Carpineti, M., Alaimo, M. D., and Giglio, M. (2010a). How to measure the optical thickness of scattering particles from the phase delay of scattered waves: application to turbid samples. *Physical review letters*, 105(19):193901.
- Potenza, M. A. C., Sanvito, T., Alaimo, M. D., Degiorgio, V., and Giglio, M. (2010b). Confocal zero-angle dynamic depolarized light scattering. *The European Physical Journal E*, 31(1):69–72.
- Potenza, M. A. C., Sanvito, T., Argenti, S., Cella, C., Paroli, B., Lenardi, C., and Milani, P. (2015a). Single particle optical extinction and scattering allows real time quantitative characterization of drug payload and degradation of polymeric nanoparticles. *Scientific reports*, 5:18228.
- Potenza, M. A. C., Sanvito, T., and Pullia, A. (2015b). Accurate sizing of ceria oxide nanoparticles in slurries by the analysis of the optical forward-scattered field. *Journal of Nanoparticle Research*, 17(2):110.
- Potenza, M. A. C., Sanvito, T., and Pullia, A. (2015c). Measuring the complex field scattered by single submicron particles. *AIP Advances*, 5(11):117222.
- Prospero, J. M., Ginoux, P., Torres, O., Nicholson, S. E., and Gill, T. E. (2002). Environmental characterization of global sources of atmospheric soil dust identified with the nimbus 7 total ozone mapping spectrometer (toms) absorbing aerosol product. *Reviews of geophysics*, 40(1):2–1.
- Purcell, E. M. and Pennypacker, C. R. (1973). Scattering and absorption of light by nonspherical dielectric grains. *The Astrophysical Journal*, 186:705–714.
- Pyne, R. L., Keller, E. D., Canessa, S., Bertler, N. A., Pyne, A. R., Mandeno, D., Vallelonga, P., Semper, S., Kjær, H. A., Hutchinson, E., et al. (2018). A novel approach to process brittle ice for continuous flow analysis of stable water isotopes. *Journal of Glaciology*, 64(244):289–299.
- Rasmussen, S. O., Bigler, M., Blockley, S. P., Blunier, T., Buchardt, S. L., Clausen, H. B., Cvijanovic, I., Dahl-Jensen, D., Johnsen, S. J., Fischer, H., et al. (2014). A stratigraphic framework for abrupt climatic changes during the last glacial period

- based on three synchronized greenland ice-core records: refining and extending the intimate event stratigraphy. *Quaternary Science Reviews*, 106:14–28.
- Rauch, J. N. and Pacyna, J. M. (2009). Earth’s global ag, al, cr, cu, fe, ni, pb, and zn cycles. *Global Biogeochemical Cycles*, 23(2).
- Redmond, H. E., Dial, K. D., and Thompson, J. E. (2010). Light scattering and absorption by wind blown dust: Theory, measurement, and recent data. *Aeolian Research*, 2(1):5–26.
- Ridgwell, A. J. (2002). Dust in the earth system: the biogeochemical linking of land, air and sea. *Philosophical Transactions of the Royal Society of London. Series A: Mathematical, Physical and Engineering Sciences*, 360(1801):2905–2924.
- Ringl, C. and Urbassek, H. M. (2013). A simple algorithm for constructing fractal aggregates with pre-determined fractal dimension. *Computer Physics Communications*, 184(7):1683–1685.
- Rondanelli, R., Molina, A., and Falvey, M. (2015). The atacama surface solar maximum. *Bulletin of the American Meteorological Society*, 96(3):405–418.
- Ruth, U. (2002). *Concentration and size distribution of microparticles in the NGRIP ice core (Central Greenland) during the last glacial period*. PhD thesis, Bremen Universität.
- Ruth, U., Barbante, C., Bigler, M., Delmonte, B., Fischer, H., Gabrielli, P., Gaspari, V., Kaufmann, P., Lambert, F., Maggi, V., et al. (2008). Proxies and measurement techniques for mineral dust in antarctic ice cores. *Environmental science & technology*, 42(15):5675–5681.
- Ruth, U., Wagenbach, D., Steffensen, J. P., and Bigler, M. (2003). Continuous record of microparticle concentration and size distribution in the central greenland ngrip ice core during the last glacial period. *Journal of Geophysical Research: Atmospheres*, 108(D3).
- Seinfeld, J. H. and Pandis, S. N. (2016). *Atmospheric chemistry and physics: from air pollution to climate change*. John Wiley & Sons.
- Sihvola, A. (2001). Two main avenues leading to the maxwell garnett mixing rule. *Journal of electromagnetic waves and applications*, 15(6):715–725.
- Simonsen, M. F. (2018). *Interglacial ice core dust from Greenland*. PhD thesis, The Niels Bohr Institute, Faculty of Science, University of Copenhagen.
- Simonsen, M. F., Cremonesi, L., Baccolo, G., Bosch, S., Delmonte, B., Erhardt, T., Kjær, H. A., Potenza, M. A. C., Svensson, A., and Vallelonga, P. (2018). Particle

- shape accounts for instrumental discrepancy in ice core dust size distributions. *Climate of the Past*, 14(5):601–608.
- Singham, S. B. and Bohren, C. F. (1987). Light scattering by an arbitrary particle: a physical reformulation of the coupled dipole method. *Optics Letters*, 12(1):10–12.
- Slingo, A., Ackerman, T. P., Allan, R., Kassianov, E. I., McFarlane, S. A., Robinson, G., Barnard, J. C., Miller, M., Harries, J., Russell, J., et al. (2006). Observations of the impact of a major saharan dust storm on the atmospheric radiation balance. *Geophysical Research Letters*, 33(24).
- Sokolik, I., Winker, D., Bergametti, G., Gillette, D., Carmichael, G., Kaufman, Y., Gomes, L., Schuetz, L., and Penner, J. (2001). Introduction to special section: Outstanding problems in quantifying the radiative impacts of mineral dust. *Journal of Geophysical Research: Atmospheres*, 106(D16):18015–18027.
- Somerville, W., Auguié, B., and Le Ru, E. (2015). Accurate and convergent t-matrix calculations of light scattering by spheroids. *Journal of Quantitative Spectroscopy and Radiative Transfer*, 160:29–35.
- Sorensen, C., Cai, J., and Lu, N. (1992). Test of static structure factors for describing light scattering from fractal soot aggregates. *Langmuir*, 8(8):2064–2069.
- Sorensen, C., Oh, C., Schmidt, P., and Rieker, T. (1998). Scaling description of the structure factor of fractal soot composites. *Physical Review E*, 58(4):4666.
- Sorensen, C. and Wang, G. (1999). Size distribution effect on the power law regime of the structure factor of fractal aggregates. *Physical Review E*, 60(6):7143.
- Sorensen, C. M. (2001). Light scattering by fractal aggregates: a review. *Aerosol Science & Technology*, 35(2):648–687.
- Sorensen, C. M. and Roberts, G. C. (1997). The prefactor of fractal aggregates. *Journal of colloid and interface science*, 186(2):447–452.
- Sorensen, C. M., Yon, J., Liu, F., Maughan, J., Heinson, W. R., and Berg, M. J. (2018). Light scattering and absorption by fractal aggregates including soot. *Journal of Quantitative Spectroscopy and Radiative Transfer*, 217:459–473.
- Spicer, P. T. and Pratsinis, S. E. (1996). Coagulation and fragmentation: Universal steady-state particle-size distribution. *AIChE journal*, 42(6):1612–1620.
- Spiga, A. and Lewis, S. R. (2010). Martian mesoscale and microscale wind variability of relevance for dust lifting. *Mars*, 5:146–158.
- Spolaor, A., Vallelonga, P., Gabrieli, J., Cozzi, G., Boutron, C., and Barbante, C.

- (2012). Determination of Fe^{2+} and Fe^{3+} species by Fe^{2+} - Fe^{3+} -ICP-MS in antarctic ice samples. *Journal of Analytical Atomic Spectrometry*, 27(2):310–317.
- Stocker, T. e. (2014). *Climate change 2013: the physical science basis: Working Group I contribution to the Fifth assessment report of the Intergovernmental Panel on Climate Change*. Cambridge University Press.
- Stroud, D. (1975). Generalized effective-medium approach to the conductivity of an inhomogeneous material. *Physical Review B*, 12(8):3368.
- Stroud, D. (1998). The effective medium approximations: Some recent developments. *Superlattices and microstructures*, 23(3-4):567–573.
- Takemura, T., Nakajima, T., Dubovik, O., Holben, B. N., and Kinne, S. (2002). Single-scattering albedo and radiative forcing of various aerosol species with a global three-dimensional model. *Journal of Climate*, 15(4):333–352.
- Teixeira, J. (1988). Small-angle scattering by fractal systems. *Journal of Applied Crystallography*, 21(6):781–785.
- Tesson, S. V., Skj  th, C. A., Šantl-Temkiv, T., and L  ndahl, J. (2016). Airborne microalgae: Insights, opportunities, and challenges. *Appl. Environ. Microbiol.*, 82(7):1978–1991.
- Torres, B., Dubovik, O., Fuertes, D., Schuster, G., Cachorro, V. E., Lapyonok, T., Goloub, P., Blarel, L., Barreto, A., Mallet, M., et al. (2017). Advanced characterisation of aerosol size properties from measurements of spectral optical depth using the grasp algorithm. *Atmospheric Measurement Techniques*, 10(10).
- Vallelonga, P., Barbante, C., Cozzi, G., Gaspari, V., Candelone, J.-P., Van De Velde, K., Morgan, V. I., Rosman, K. J., Boutron, C. F., and Cescon, P. (2004). Elemental indicators of natural and anthropogenic aerosol inputs to law dome, antarctica. *Annals of Glaciology*, 39:169–174.
- Vallelonga, P., Gabrielli, P., Balliana, E., Wegner, A., Delmonte, B., Turetta, C., Burton, G., Vanhaecke, F., Rosman, K., Hong, S., et al. (2010). Lead isotopic compositions in the epica dome c ice core and southern hemisphere potential source areas. *Quaternary Science Reviews*, 29(1-2):247–255.
- Van de Hulst, H. C. (1981). *Light scattering by small particles*. Courier Corporation.
- Vecchi, R., Bernardoni, V., Paganelli, C., and Valli, G. (2014). A filter-based light-absorption measurement with polar photometer: Effects of sampling artefacts from organic carbon. *Journal of Aerosol Science*, 70:15–25.
- Villa, S., Sanvito, T., Paroli, B., Pullia, A., Delmonte, B., and Potenza, M. A. C.

- (2016). Measuring shape and size of micrometric particles from the analysis of the forward scattered field. *Journal of Applied Physics*, 119(22):224901.
- Vogt, R., Crutzen, P. J., and Sander, R. (1996). A mechanism for halogen release from sea-salt aerosol in the remote marine boundary layer. *Nature*, 383(6598):327.
- Wallace, J. M. and Hobbs, P. V. (2006). *Atmospheric science: an introductory survey*, volume 92. Elsevier.
- Wang, G. and Sorensen, C. M. (2002). Experimental test of the rayleigh-debye-gans theory for light scattering by fractal aggregates. *Applied optics*, 41(22):4645–4651.
- Weitz, D. and Lin, M. (1986). Dynamic scaling of cluster-mass distributions in kinetic colloid aggregation. *Physical review letters*, 57(16):2037.
- Weitz, D. and Oliveria, M. (1984). Fractal structures formed by kinetic aggregation of aqueous gold colloids. *Physical Review Letters*, 52(16):1433.
- Winton, V., Dunbar, G., Bertler, N., Millet, M.-A., Delmonte, B., Atkins, C., Chewings, J., and Andersson, P. (2014). The contribution of aeolian sand and dust to iron fertilization of phytoplankton blooms in southwestern ross sea, antarctica. *Global Biogeochemical Cycles*, 28(4):423–436.
- Witherow, R. A., Lyons, W. B., Bertler, N. A., Welch, K. A., Mayewski, P. A., Sneed, S. B., Nylen, T., Handley, M. J., and Fountain, A. (2006). The aeolian flux of calcium, chloride and nitrate to the mcmurdo dry valleys landscape: evidence from snow pit analysis. *Antarctic Science*, 18(4):497–505.
- Witten, T. A. and Sander, L. M. (1983). Diffusion-limited aggregation. *Physical Review B*, 27(9):5686.
- Wolff, E., Barbante, C., Becagli, S., Bigler, M., Boutron, C., Castellano, E., De Angelis, M., Federer, U., Fischer, H., Fundel, F., et al. (2010). Changes in environment over the last 800,000 years from chemical analysis of the epica dome c ice core. *Quaternary Science Reviews*, 29(1-2):285–295.
- Ysard, N., Jones, A., Demyk, K., Boutéraon, T., and Koehler, M. (2018). The optical properties of dust: the effects of composition, size, and structure. *Astronomy & Astrophysics*, 617:A124.
- Yurkin, M. A. (2013). Computational approaches for plasmonics. *Handbook of Molecular Plasmonics*, pages 83–135.
- Yurkin, M. A. and Hoekstra, A. G. (2007). The discrete dipole approximation:

- an overview and recent developments. *Journal of Quantitative Spectroscopy and Radiative Transfer*, 106(1-3):558–589.
- Yurkin, M. A. and Hoekstra, A. G. (2011). The discrete-dipole-approximation code adda: capabilities and known limitations. *Journal of Quantitative Spectroscopy and Radiative Transfer*, 112(13):2234–2247.
- Yurkin, M. A. and Hoekstra, A. G. (2014). User manual for the discrete dipole approximation code adda 1.3 b4.
- Zender, C. S., Miller, R., and Tegen, I. (2004). Quantifying mineral dust mass budgets: Terminology, constraints, and current estimates. *Eos, Transactions American Geophysical Union*, 85(48):509–512.
- Zennaro, P., Kehrwald, N., McConnell, J. R., Schüpbach, S., Maselli, O. J., Marlon, J., Vallelonga, P., Leuenberger, D., Zangrando, R., Spolaor, A., Borrotti, M., Barbaro, E., Gambaro, A., and Barbante, C. (2014). Fire in ice: two millennia of boreal forest fire history from the greenland neem ice core. *Climate of the Past*, 10(5):1905–1924.

Acknowledgements

I would like to acknowledge my advisor, Prof. Marco Potenza, Dr. Barbara Delmonte, Dr. Marius Simonsen, Prof. Alberto Parola and Prof. Fabio Ferri for their precious help and guidance throughout these years.

I would also like to thank the Referees: the accurate criticisms and suggestions by Prof. Paul Vallelonga and Dr. Dario Massabò contributed to ameliorate this text considerably.

Many other people contributed to this work in a more indirect, yet not less meaningful way. To them I extend my deepest gratitude.